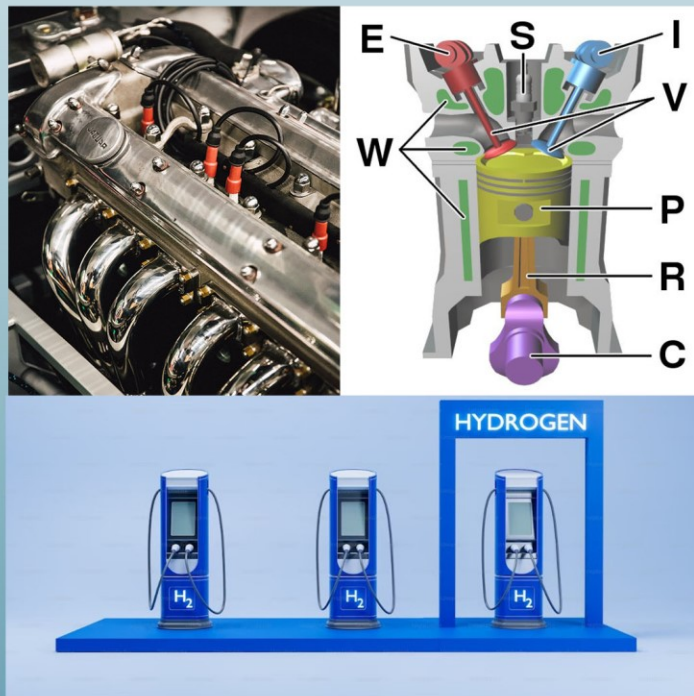


ISSN: 2376-2136 (Print)
ISSN: 2376-2144 (Online)

Trends in Renewable Energy

Volume 10, Issue 3, December 2024



Cover image: Series of Hydrogen Engine Articles by Liu, Ma and Xu



futureenergysp.com
thefutureenergy.org

Trends in Renewable Energy

ISSN: 2376-2136 (Print) ISSN: 2376-2144 (Online)

<http://futureenergysp.com/>

Trends in Renewable Energy is an open accessed, peer-reviewed semi-annual journal publishing reviews and research papers in the field of renewable energy technology and science.

The aim of this journal is to provide a communication platform that is run exclusively by scientists working in the renewable energy field. Scope of the journal covers: Bioenergy, Biofuel, Biomass, Bioprocessing, Biorefinery, Biological waste treatment, Catalysis for energy generation, Energy conservation, Energy delivery, Energy resources, Energy storage, Energy transformation, Environmental impact, Feedstock utilization, Future energy development, Green chemistry, Green energy, Microbial products, Physico-chemical process for Biomass, Policy, Pollution, Renewable energy, Smart grid, Thermo-chemical processes for biomass, etc.

The Trends in Renewable Energy publishes the following article types: peer-reviewed reviews, mini-reviews, technical notes, short-form research papers, and original research papers.

The article processing charge (APC), also known as a publication fee, is fully waived for the Trends in Renewable Energy.

Editorial Team of Trends in Renewable Energy

EDITOR-IN-CHIEF

Dr. Bo Zhang
Dr. Changyan Yang

Editor, Trends in Renewable Energy, USA
Prof., School of Chemical Engineering & Pharmacy, Wuhan Institute of Technology, China

HONORARY CHAIRMEN

Dr. Yong Wang
Dr. Mahendra Singh Sodha
Dr. Elio Santacesaria

Voiland Distinguished Professor, The Gene and Linda Voiland School of Chemical Engineering and Bioengineering, Washington State University, United States
Professor, Lucknow University; Former Vice Chancellor of Devi Ahilya University, Lucknow University, and Barkatulla University; Professor/Dean/HOD/Deputy Director at IIT Delhi; Padma Shri Award; India
Professor of Industrial Chemistry, CEO of Eurochem Engineering srl, Italy

VICE CHAIRMEN

Dr. Mo Xian

Prof., Assistant Director, Qingdao Institute of BioEnergy and Bioprocess Technology, Chinese Academy of Sciences, China

EDITORS

Dr. Yiu Fai Tsang,
Dr. Melanie Sattler
Dr. Attila Bai
Prof. Christophe Pierre Ménézo
Dr. Moinuddin Sarker
Dr. Suzana Yusup
Dr. Zewei Miao
Dr. Hui Wang
Dr. Shuangning Xiu
Dr. Junming XU
Dr. Hui Yang
Dr. Ying Zhang
Dr. Ming-Jun Zhu

Associate Prof., Department of Science and Environmental Studies, The Education University of Hong Kong
Dr. Syed Qasim Endowed Professor, Dept. of Civil Engineering, University of Texas at Arlington, United States
Associate Prof., University of Debrecen, Hungary
University of Savoy Mont-Blanc, France
MCIC, FICER, MInstP, MRSC, FARSS., VP of R & D, Head of Science/Technology Team, Natural State Research, Inc., United States
Associate Prof., Biomass Processing Laboratory, Centre for Biofuel and Biochemical Research, Green Technology Mission Oriented Research, Universiti Teknologi PETRONAS, Malaysia
Global Technology Development, Monsanto Company, United States
Pfizer Inc., United States
North Carolina Agricultural and Technical State University, United States
Associate Prof., Institute of Chemical Industry of Forest Products, China Academy of Forest, China
Prof., College of Materials Science and Engineering, Nanjing Tech University, China
Associate Prof., School of Chemistry and Materials Science, University of Science and Technology of China, China
Prof., Assistant Dean, School of Bioscience & Bioengineering, South China University of Technology, China

EDITORIAL BOARD

Dr. Risabh Dev Shukla
Dr. Neeraj Gupta
Dr. Elena Lucchi

Dean and Associate Prof., Department of Electrical Engineering, Budge Budge Institute of Technology Kolkata, India
Indian Institute of Technology Roorkee, India
Politecnico di Milano, Italy

Dr. Muhammad Mujtaba Asad	Faculty of Technical and Vocational Education, Universiti Tun Hussein Onn Malaysia, Malaysia
Dr. Afzal Sikander	Department of Instrumentation and Control Engineering, Dr. B. R. Ambedkar National Institute of Technology, India
Dr. Padmanabh Thakur	Professor and Head, Department of Electrical Engineering, Graphic Era University, India
Dr. K. DHAYALINI	Professor, Department of Electrical and Electronics Engineering, K. Ramakrishnan College of Engineering, Tamilnadu, India
Shangxian Xie	Texas A&M University, United States
Dr. Tanmoy Dutta	Sandia National Laboratories, United States
Dr. Efstathios Stefos	Pontifical Catholic University of Ecuador, Faculty of Exact and Natural Sciences, School of Physical Sciences and Mathematics, Ecuador
Dr. Xin Wang	Miami University, United States
Dr. Rami El-Emam	Assist. Prof., Faculty of Engineering, Mansoura University, Egypt
Dr. Rameshprabu Ramaraj	School of Renewable Energy, Maejo University, Thailand
Dr. ZAFER ÖMER ÖZDEMİR	Kirklareli University, Technology Faculty, Turkey
Dr. Vijay Yeul	Chandrapur Super Thermal Power Station, India
Dr. Mohanakrishna Gunda	VITO - Flemish Institute for Technological Research, Belgium
Dr. Shuai Tan	Georgia Institute of Technology, United States
Shahabaldin Rezanian	Universiti Teknologi Malaysia (UTM), Malaysia
Dr. Madhu Sabnis	Contek Solutions LLC, Texas, United States
Dr. Qiang Yan	Mississippi State University, United States
Dr. Mustafa Tolga BALTA	Associate Prof., Department of Mechanical Engineering, Faculty of Engineering, Aksaray University, Turkey
Dr. María González Alriols	Associate Prof., Chemical and Environmental Engineering Department, University of the Basque Country, Spain
Dr. Nattaporn Chaiyat	Assist. Prof., School of Renewable Energy, Maejo University, Thailand
Dr. Nguyen Duc Luong	Institute of Environmental Science and Engineering, National University of Civil Engineering, Vietnam
Mohd Lias Bin Kamal	Faculty of Applied Science, Universiti Teknologi MARA, Malaysia
Dr. N.L. Panwar	Assistant Prof., Department of Renewable Energy Engineering, College of Technology and Engineering, Maharana Pratap University of Agriculture and Technology, India
Dr. Caio Fortes	BASF, Brazil
Dr. Flavio Praticco	Department of Methods and Models for Economics, Territory and Finance, Sapienza University of Rome, Italy
Dr. Wennan ZHANG	Docent (Associate Prof.) and Senior Lecturer in Energy Engineering, Mid Sweden University, Sweden
Dr. Ing. Stamatis S. Kalligeros	Associate Prof., Hellenic Naval Academy, Greece
Carlos Rolz	Director of the Biochemical Engineering Center, Research Institute at Universidad del Valle, Guatemala
Ms. Liliash Makashini	Copperbelt University, Zambia
Dr. Ali Mostafaeipour	Associate Prof., Industrial Engineering Department, Yazd University, Iran
Dr. Camila da Silva	Prof., Maringá State University, Brazil
Dr. Anna Skorek-Osikowska	Silesian University of Technology, Poland
Dr. Shek Atiqure Rahman	Sustainable and Renewable Energy Engineering, College of Engineering, University of Sharjah, Bangladesh
Dr. Emad J Elnajjar	Associate Prof., Department of Mechanical Engineering, United Arab Emirates University, United Arab Emirates
Dr. Seyed Soheil Mousavi Ajarostaghi	Babol Noshirvani University of Technology, Babol, Iran
Dr. Dinesh K. Sharma	National Ecology and Environment Foundation, India
Dr. Lakshmana Kumar Ramasamy	Department of Corporate relations, Hindusthan College of Engineering and Technology, India
Dr. S. Venkata Ramana	SUSU/National Research University, Russian Federation
Dr. Priyanka Marathay	Department of Solar Energy, Pandit Deendayal Petroleum University, India
Osamah Siddiqui	University of Ontario Institute of Technology, Canada
Dr. Rupendra Kumar Pachauri	Assistant Prof., Electrical and Electronics Engineering Department, University

of Petroleum and Energy Studies, India

Dr. Jun Mei School of Chemistry and Physics, Science and Engineering Faculty,
Queensland University of Technology, Australia

Dr. Valeria Di Sarli Institute for Research on Combustion, National Research Council of Italy, Italy

Dr. Utkucan Şahin Assistant Prof., Department of Energy Systems Engineering, Faculty of
Technology, Muğla Sıtkı Koçman University, Turkey

Dr. ALIASHIM ALBANI School of Ocean Engineering, Universiti Malaysia Terengganu, Malaysia

Dr. Ashwini Kumar Assistant Prof., College of Engineering, HSBPVT's Parikrama Group of
Institutions, India

Dr. Hasan AYDOGAN Associate Prof., Mechanical Engineering Department, Selcuk University,
Turkey

Dr. Jiekang Wu Professor, School of Automation, Guangdong University of Technology, China

Dr. Ong Huei Ruey DRB-HICOM University of Automotive, Malaysia

Dr. Miguel Ángel Reyes Belmonte IMDEA Energy Institute, Spain

Dr. Chitra Venugopal Associate Professor in Electrical Engineering, University of Trinidad and
Tobago, Trinidad

Dr. Amit Kumar Singh Assistant Prof., Instrumentation & Control Engineering Department,
Dr. B.R.A. National Institute of Technology, India

Dr. Suvanjan Bhattacharyya University of Pretoria, South Africa

Dr. Karunesh Tiwari Babu Banarasi Das University, India

Dr. Sharadrao A. Vhanalkar Karmaveer Hire Arts, Science, Commerce and Education College, India

Dr. Prasenjit Chatterjee Assistant Prof. and Head, MCKV Institute of Engineering, India

Dr. S. Balamurugan Mindnotix Technologies, India

Dr. Mohammad Nurunnabi University of Oxford, United Kingdom

Dr. Kenneth Okedu Caledonian College of Engineering, Oman

Dr. Cheng Zhang Sr. Materials Engineer, Medtronic, Inc., United States

Dr. Chandani Sharma Assistant Prof., Department of Electrical Engineering, Graphic Era University,
India

Dr. Kashif Irshad Assistant Prof., Mechanical Engineering Department, King Khalid University,
Saudi Arabia

Dr. Abhijit Bhagavatula Principal Lead Engineer, Southern Company Services, United States

Dr. S. Sathish Associate Prof., Department of Mechanical Engineering, Hindustan University,
India

Dr. Bindeshwar Singh Assistant Prof., Kamla Nehru Institute of Technology, India

Dr. Yashar Hashemi Tehran Regional Electric Company, Iran

Dr. Navanietha Krishnaraj R South Dakota School of Mines and Technology, United States

Dr. SANDEEP GUPTA JECRC University, India

Dr. Shwetank Avikal Graphic Era Hill University, India

Dr. Xianglin Zhai Poochon Scientific LLC, United States

Dr. Rui Li Associate Prof., College of Engineering, China Agricultural University, China

Dr. Adam Elhag Ahmed National Nutrition Policy Chair, Department of Community Services, College of
Applied Medical Sciences, King Saud University, Saudi Arabia

Dr. Jingbo Li Massachusetts Institute of Technology, United States

Dr. Srikanth Mutnuri Associate Prof., Department of Biological Sciences, Associate Dean for
International Programmes and Collaboration, Birla Institute of Technology &
Science, India

Dr. Bashar Malkawi Global Professor of Practice in Law, James E. Rogers College of Law,
University of Arizona, United States

Dr. Simona Silvia Merola Istituto Motori - National Research Council of Naples, Italy

Dr. Hakan Caliskan Faculty of Engineering, Department of Mechanical Engineering, Usak
University, Turkey

Dr. Umashankar Subramaniam Associate Prof., College of Engineering, Prince Sultan University, Saudi
Arabia

Dr. Tayfun GÜNDOĞDU Faculty of Electrical and Electronic Engineering, Department of Electrical
Engineering, Istanbul Technical University, Turkey

Dr. Yukesh Kannah R Department of Civil Engineering, Anna University Regional Campus, India

Jean Bosco Mugiraneza University of Rwanda, Rwanda

Dr. R. Parameshwaran Assistant Prof., Dept. of Mechanical Engineering, Birla Institute of Technology

Dr. Endong Wang & Science (BITS-Pilani), India
Associate Prof., Department of Sustainable Resources Management, College of Environmental Science and Forestry, State University of New York (SUNY-ESF), USA

Dr. Jianxin Xu Prof., Faculty of metallurgy and energy engineering, Kunming University of Science and Technology, China

Dr. Qingtai Xiao Distinguished Associate Prof., Department of Energy and Power Engineering, Kunming University of Science and Technology, China

Abaubakry M' BAYE Facilities, Utilities and Energy manager, Glaxo Smith & Kline, France

Dr. Omar Behar Clean Combustion Research Center (CCRC), King Abdullah University of Science & Technology (KAUST), Saudi Arabia

Dr. Mohammad Mahdi Ahmadi Technical and Vocational University, Hekmat University, Iran

Dr. M. Karthikeyan Associate Professor, Chennai Institute of Technology, India

Dr. Karan Kumar RWTH Aachen University, Germany

Table of Contents

Volume 10, Issue 3, December 2024

Development Status and Outlook of Hydrogen Internal Combustion Engine

Mengfei Liu..... 257-265

Effect of Hydrogen Injection Flow Rate on the Performance of In-Cylinder Direct Injection Hydrogen Engines

Honglin Ma..... 266-282

Effect of Compression Ratio on the Performance of Direct-Injection Hydrogen Engines

Zhe Xu..... 283-300

Virtual Topologies for Populating Overhead Low-Voltage Broadband over Powerlines Topology

Classes by Exploiting Neural Network Topology Generator Methodology (NNTGM) - Part 1: Theory

Athanasios G. Lazaropoulos..... 301-314

Virtual Topologies for Populating Overhead Low-Voltage Broadband over Powerlines Topology

Classes by Exploiting Neural Network Topology Generator Methodology (NNTGM) - Part 2:

Numerical Results

Athanasios G. Lazaropoulos..... 315-334

Development Status and Outlook of Hydrogen Internal Combustion Engine

Mengfei Liu*

North China University of Water Resources and Electric Power, Zhengzhou City, No. 36, Beihuan Road, Henan, China

Received June 29, 2024; Accepted July 30, 2024; Published August 15, 2024

Hydrogen energy is one of the best energy carriers for achieving carbon peak and carbon neutrality, with the characteristics of high energy and no pollution. The hydrogen internal combustion engine is one of the important forms of hydrogen energy utilization, with the significant advantages of high efficiency, high reliability, low cost and low emissions. In this paper, the characteristics of hydrogen internal combustion engines and hydrogen fuel cells were compared, and the industrialization prospects of hydrogen energy utilization in the future were analyzed. Focusing on the hydrogen internal combustion engine technology system, a comprehensive analysis was conducted on the technical issues and technical progress in hydrogen storage, combustion, NO_x emissions, etc. of hydrogen internal combustion engines.

Keywords: Hydrogen internal combustion engine; Hydrogen storage; Combustion characteristics; Emission

Introduction

The current social energy system is dominated by disposable energy such as oil and natural gas. With the increase in energy demand, environmental pollution and greenhouse effect problems are becoming increasingly prominent. To achieve sustainable development, countries around the world are vigorously developing green energy such as solar energy, wind energy, and hydrogen energy. China has also put forward the strategic goals of reaching carbon peak by 2030 and carbon neutrality by 2060. Due to their inherent randomness and volatility, most renewable energy sources will produce serious losses of light energy, wind energy, etc. As a chemical energy storage energy source, hydrogen can effectively recover waste energy. Its high energy density (140 MJ/kg, 4.5 times that of coal, 3 times that of oil) and clean and pollution-free characteristics are regarded as the future energy technology direction [1, 2]. The use of hydrogen energy can reduce local pollution, lower global carbon dioxide emissions, and resolve the constraints of non-renewable energy such as oil and natural gas on human development.

The Structure, Material and Working Principle of Hydrogen Internal Combustion Engine

Hydrogen internal combustion engine, also known as hydrogen fuel engine, is an internal combustion engine using hydrogen as fuel. It basically follows the standard

*Corresponding author: a2593567927@163.com

working principle of internal combustion engines, including four-stroke and two-stroke engines. This article focuses on four-stroke hydrogen internal combustion engines because they are more common in practical applications.

Hydrogen Internal Combustion Engine Structure

The structure of the hydrogen internal combustion engine is mainly composed of hydrogen supply system, combustion chamber, hydrogen and air mixing system, and cooling system. The hydrogen supply system includes hydrogen storage tank, hydrogen pipeline and injection system. Hydrogen is usually stored at high pressure and introduced into the engine through an appropriate injection system. The combustion chamber design needs to adapt to the characteristics of hydrogen, and usually requires higher ignition capacity and suitable combustion chamber shape to ensure sufficient combustion efficiency. The hydrogen and air mixing system is used to adjust and optimize the mixing ratio of hydrogen and air in the combustion chamber to achieve the best combustion efficiency and power output. The cooling system of internal combustion engines needs to adapt to higher operating temperatures, especially due to the heat generated by hydrogen [3].

Materials for Hydrogen Internal Combustion Engines

The materials used in the hydrogen internal combustion engine mainly include burner materials, valve and piston materials, and sealing materials. Burner materials require high temperature resistance and corrosion resistance. Common choices include special alloys or ceramic materials. Valve and piston materials also need to choose materials that can withstand high temperature and high pressure to ensure the long-term reliability and performance of the internal combustion engine. Due to the small molecular size of hydrogen, special sealing materials are needed to prevent hydrogen leakage.

Working Cycle of Hydrogen Internal Combustion Engine

The working cycle of the hydrogen internal combustion engine is divided into intake, compression, ignition, work and exhaust. The intake is to mix hydrogen and air into the combustion chamber. The compressed gas is compressed by the piston to increase its temperature and pressure. The ignition system ignites the mixture and causes combustion. The work process is that the energy of the gas drives the piston to move and generate power. The exhaust gas after combustion in the exhaust process is discharged through the exhaust valve [4].

Characteristics of Hydrogen Internal Combustion Engines

There are many ways to use hydrogen energy, among which hydrogen fuel cells and hydrogen internal combustion engines are the most concerned. Hydrogen fuel cells convert the chemical energy in hydrogen fuel directly into electrical energy through electrochemical reactions. They have high energy utilization, stable operating conditions and zero emissions, and were once considered the most effective way to utilize hydrogen energy. However, the high purity of hydrogen (99.99%), the dependence on the rare metal platinum, and the imperfect industrial system have led to the high price of hydrogen fuel cells. In the foreseeable period of time, it will be difficult for hydrogen fuel cells to meet the needs of the whole society through large-scale and industrialized

production. On the contrary, although the hydrogen internal combustion engine is insufficient in terms of energy utilization and emissions, it is not much different from the traditional internal combustion engine in terms of structure, and the production of hydrogen internal combustion engine can rely on the existing industrial system to carry out mass production at low cost. On the whole, in terms of hydrogen energy utilization, hydrogen internal combustion is more promising for large-scale production and use in the automobile industry.

Hydrogen internal combustion engines have many advantages over hydrogen fuel cells. Most of the parts are the same as gasoline/diesel engines, and the material cost is about CNY 13,000. The existing production line can be used to save costs. The engine has high durability, about 300,000 km. It has low requirements for hydrogen purity and does not rely on rare metals. Overall, the biggest advantages of hydrogen-fueled engines lie in cost and industrialization prospects.

Development Status of Hydrogen Internal Combustion Engines

Up to now, hydrogen internal combustion engines have a history of development for several decades. As early as 2000, Ford officially began research on hydrogen internal combustion engines. Subsequently, foreign automobile companies such as BMW, Mazda and other automobile companies, and domestic companies such as Changan Automobile have all invested in the research and development of hydrogen internal combustion engines.

The development of hydrogen internal combustion engines has not been smooth sailing. During the in-depth research process, problems such as engine backfire, hydrogen embrittlement, and emissions have emerged one after another. BMW and other automobile companies have given up on exploring hydrogen internal combustion engines for cars due to reasons such as the inability to resolve the problem of on-board hydrogen storage, insufficient power caused by hydrogen injection in the airway, and imperfect hydrogen refueling stations. In the following years, the development of automotive hydrogen internal combustion engines stagnated. As time goes by, technology and materials continue to make breakthroughs, and problems such as storage, combustion, and emissions of on-board hydrogen have been effectively solved. Hydrogen internal combustion engines have regained attention in recent years. In 2019, SAIC Motor and Bosch Group respectively released 2.0-liter in-cylinder direct-injection turbocharged hydrogen internal combustion engines. Subsequently, in 2021, Toyota's hydrogen internal combustion engine vehicle Toyota-Corolla held a 24h rally at Fuji Circuit in Japan. In China, FAW, GAC, Great Wall and other automobile companies also launched different models of in-cylinder direct injection turbocharged hydrogen engine samples.

Overall, the research on hydrogen internal combustion engines can be divided into two phases: The first stage was from 2000 to 2007, the stage of gas-port hydrogen injection internal combustion engines developed by BMW. The second stage was from 2019 to the present, the stage of research and development of direct-injection hydrogen internal combustion engines represented by SAIC, Bosch and others.

Technical Problems and Development Status of Hydrogen Internal Combustion Engines

On-board Hydrogen Storage

The storage of hydrogen has always been a difficult problem in the research of hydrogen energy-related technologies. Hydrogen molecules are small in size and can easily penetrate into the interior of the storage tank material, hydrogenating the material and causing hydrogen embrittlement of the material. At the same time, the flammable and explosive nature of hydrogen restricts the application scenarios of hydrogen energy [5]. Especially in automotive engines, it is a huge challenge to store enough hydrogen fuel in a limited space to ensure mileage. At present, there are three main research directions of hydrogen storage methods: high-pressure gaseous hydrogen storage, low-temperature liquid hydrogen storage, and material-based hydrogen storage.

As early as the end of the nineteenth century, forged metal containers were used for hydrogen storage with a hydrogen storage pressure of 12 MPa. Because hydrogen molecules can easily penetrate into the cylinder to corrode the cylinder, resulting in hydrogen embrittlement. The cylinders are at risk of bursting under high pressure [6], and therefore are not used for on-board hydrogen storage. In 1963, Brunswick developed a high-pressure gas cylinder made of fully wound glass fiber composite material with a plastic liner. In 2001, Quantum successfully developed a high-pressure hydrogen storage cylinder with a carbon fiber fully wound structure with a polyethylene liner and a working pressure of 70 MPa.

In the automotive field, the most widely used hydrogen storage technology is high-pressure hydrogen storage cylinders. With the increasing demand for on-board hydrogen storage applications, light weight and high pressure are the final requirements for hydrogen storage cylinders. At present, high-pressure hydrogen storage containers have been developed from all-metal (type I bottles) to plastic liner fiber fully wound gas cylinders (type IV cylinders). The comparison of different types of high-pressure hydrogen storage cylinders is shown in Table 1.

Table 1. Comparison of different types of hydrogen storage bottles [5]

Type	Material quality	Working Pressure (MPa)	Cost	Vehicle available
Type I	Pure steel metal bottles	17.5~20	Low	No
Type II	Steel liner fiber winding bottle	26.5~30	Mid	No
Type III	Aluminum Liner filament winding bottle	30~70	High	Yes
Type IV	Plastic Liner filament winding bottle	>70	High	Yes

Type I hydrogen storage tank is not suitable for vehicle-mounted hydrogen storage because of its pure metal properties. Currently, Type III and Type IV are the mainstream composite hydrogen cylinders. It is mainly composed of inner liner and carbon fiber material. The fiber material is wound around the inner liner in a ring or spiral shape, which can effectively improve the structural strength of the inner liner. In the automotive field, Type IV hydrogen storage bottles have been successfully commercialized. However, China's research on high-pressure hydrogen storage started late. Limited by carbon fiber technology and filament winding technology, it is still committed to the development of Type III hydrogen storage bottles.

Deflagration, Pre-ignition and Tempering

The problems of hydrogen internal combustion engine are inseparable from its advantages. Firstly, the propagation speed of hydrogen combustion is extremely fast (about 9 times that of gasoline combustion), which will cause the combustion time to be too short and the combustion work time to be short. It cannot overcome the compression work and easily cause the engine to stall, that is, the deflagration problem. Secondly, because of the low ignition point of hydrogen, the overheating of the spark plug motor and the hot deposition in the internal combustion engine will lead to the natural occurrence of hydrogen and the problem of premature combustion. At the same time, due to the fast propagation speed of combustion, the intake valve has not yet closed at this time, and the flame will enter the intake pipe, causing backfire.

At present, enterprises are promoting direct injection technology, which injects hydrogen directly into the engine cylinder. This not only eliminates the problem of hydrogen occupying cylinder volume, but also greatly improves the power performance of hydrogen internal combustion engines. Compared with the intake port injection, the direct injection hydrogen internal combustion engine can inject hydrogen after the intake valve is closed to avoid the tempering problem caused by hydrogen backflow. The comparison of in-cylinder direct injection and inlet injection is shown in Table 2.

Table 2. Comparison of in-cylinder direct injection and inlet hydrogen injection [7]

Jetting method	Injection timing	Abnormal combustion	Mixture gas	Feature
Single poin injection of inlet	The initial stage of intake stroke	High risk tempering	Form uneven mixtu gas	Low sound power high combustion risk
Inlet multi-point injection	The end of the exhaust strol	Low risk backfir	Form a uniform mixture gas	Abnormal combustion risk
Direct injection	The initial stage of compression stroke	No tempering	Basically uniform	Low power

In a direct injection hydrogen internal combustion engine, uneven distribution of the mixer may cause premature ignition and detonation [8]. Verhelst *et al.* summarized the relationship between the knock intensity and the mass fraction of the unburned mixer. It can be concluded that the main methods of suppressing knock in hydrogen internal combustion engines are: optimizing the combustion chamber structure, optimizing the injection strategy, using EGR and water injection to reduce the temperature in the dry cylinder, and using the pressurization technology to improve the knock boundary [9].

Emission

In theory, hydrogen internal combustion engine has five emission products: H₂, HC, CO, CO₂ and NO_x. Among them, CO, CO₂ and HC are produced by oil combustion, and the emission concentration is small. As the main emission of hydrogen internal combustion engine, NO_x is formed by the reaction of nitrogen and oxygen at high temperature of the cylinder, and the emission can reach 0.02 g/kW·h [10]. Therefore, controlling NO_x emissions is the key to controlling emissions from hydrogen internal combustion engines. At present, there are mainly the following means to reduce NO_x emissions.

Lean Burn and Injection Parameter Optimization

The NO_x emission of hydrogen internal combustion engine is closely related to the excess air coefficient λ . When λ reaches 2.5, it reaches the zero boundary point (as shown in Figure 1).

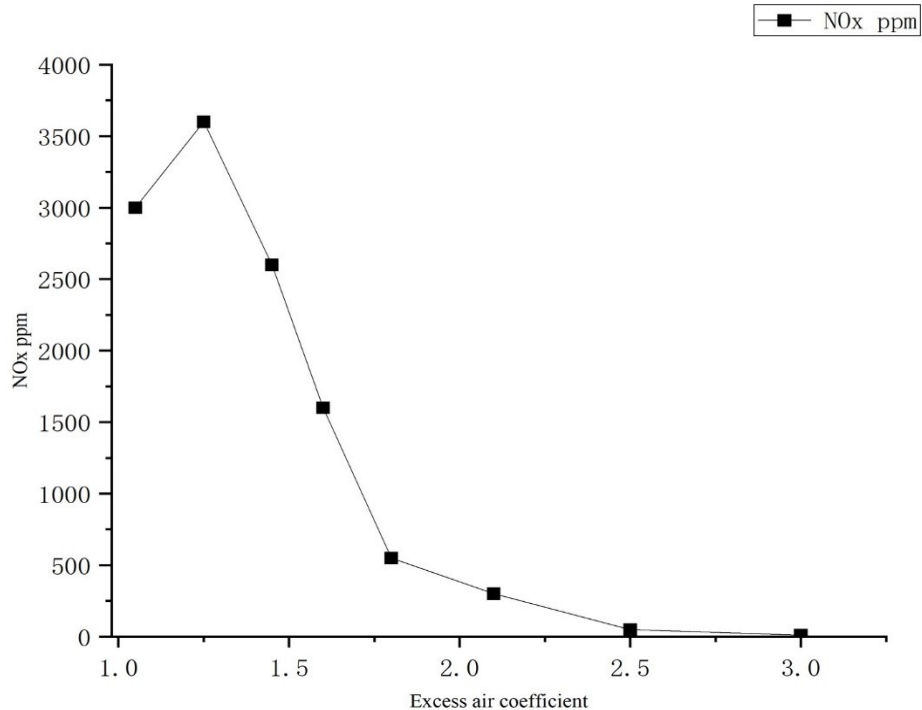


Fig. 1. Effect of excess air ratio on NO_x emissions

Therefore, controlling the excess air coefficient is the most effective way to reduce the emissions of hydrogen internal combustion engines. In order to ensure the combustion stability of the internal combustion engine, λ is generally less than 3.3. So, when λ is between 2.5 and 3.3, it can not only return the emission to zero, but also ensure the stability of hydrogen combustion. The intake pressure is increased by mechanical supercharging or turbocharging to ensure the power performance of the hydrogen internal combustion engine under lean combustion, so that the hydrogen internal combustion engine always works under the condition of $\lambda > 2.5$, and the emission is usually less than $0.1 \text{ g/kW}\cdot\text{h}$.

Wanner *et al.* [11] studied the effect of injection phase on emissions, and concluded that the injection was advanced and the emission was reduced under partial load. Under heavy load conditions, delayed injection will lead to reduced emissions. This is because under some conditions, the overall combustion is thin, and early injection can extend the mixing time of the mixture to form a low concentration uniform mixture, reducing emissions. Under heavy load conditions, delayed injection can make the mixture in the cylinder stratified, avoiding the high emission stage to reduce emissions [12].

EGR Technology and Water Injection Technology

EGR (Exhaust Gas Recirculation) technology can significantly reduce the combustion temperature and combustion rate, thereby effectively reducing emissions [13].

The principle of the water injection technology is similar to that of EGR technology. But compared with the EGR technology, the water injection technology can more accurately control the combustion medium and combustion temperature without significantly affecting the power performance of the internal combustion engine. According to the injection method, the water injection technology can be divided into two forms: inlet water injection and direct injection in cylinder [14].

Post-Processing Techniques

In addition to the above-mentioned means of reducing in-cylinder emissions, further treatment of out-cylinder emissions is required to enable hydrogen internal combustion engines to meet increasingly stringent emission standards.

Tokyo City University in Japan has proposed a new exhaust emission after-treatment technology - a two-stage nitrogen oxide storage reduction system (NSR) and oxidation catalyst (DOC) combined system. The system works by utilizing incompletely burned hydrogen or injecting low-pressure hydrogen into the after-treatment system for reduction in the NSR, where the DOC system is responsible for the unreacted oxygen and ammonia produced during the oxidation-reduction process. According to the literature [15], the NO_x purification rate can reach 98%, while the hydrogen consumption only increases NO_x by 0.2~0.5 %. This set of post-treatment technology has a significant effect on vehicle operation, reducing cycle emissions from 1.07 g/kW·h to 0.08 g/kW·h. LNT (lean trap) and SCR (selective catalytic reduction) post-treatment technologies were studied [16]. By utilizing the concentration changes in the engine mixer, periodic adsorption-catalytic reduction and chemical reactions are carried out to completely remove a small amount of NO_x emissions and achieve double zero emissions.

CONCLUSIONS

In recent years, great progress has been made in the practical application of hydrogen internal combustion engines. The industrialization prospect of hydrogen internal combustion engines is relatively bright. In the short term, hydrogen internal combustion engines are more suitable than hydrogen fuel cells for achieving carbon neutrality and carbon peak goals.

The hydrogen internal combustion engine has effectively solved the problems of hydrogen storage, combustion and emission, providing strong support for the future industrialization of hydrogen internal combustion engines. However, at the same time, under the current technical form, hydrogen storage technology and hydrogen injection technology need to be further improved. And because hydrogen fuel is different from diesel and gasoline fuel, we should get rid of the original internal combustion engine framework and establish a new hydrogen internal combustion system as soon as possible based on the characteristics of hydrogen fuel.

CONFLICTS OF INTEREST

The author declares that there is no conflict of interests regarding the publication of this paper.

REFERENCES

- [1] Hosseini, S. E., & Wahid, M. A. (2020). Hydrogen from solar energy, a clean energy carrier from a sustainable source of energy. *International Journal of Energy Research*, 44(6), 4110-4131. doi: <https://doi.org/10.1002/er.4930>
- [2] Liu, Y., Guo, H., & Ouyang, X. (2021). Development status and future prospects of hydrogen fuel cell technology. *Strategic Study of Chinese Academy of Engineering*, 23(4), 162-171. doi: <https://doi.org/10.15302/J-SSCAE-2021.04.019>
- [3] Sun, Z., Hong, J., Zhang, T., Sun, B., Yang, B., Lu, L., ... & Wu, K. (2023). Hydrogen engine operation strategies: recent progress, industrialization challenges, and perspectives. *International Journal of Hydrogen Energy*, 48(1), 366-392. doi: <https://doi.org/10.1016/j.ijhydene.2022.09.256>
- [4] Hosseini, S. E., & Butler, B. (2020). An overview of development and challenges in hydrogen powered vehicles. *International journal of green energy*, 17(1), 13-37. doi: <https://doi.org/10.1080/15435075.2019.1685999>
- [5] Li Jian, Zhang Lixin, Li Ruiyi, Yang Xiao, & Zhang Ting. (2021). Research progress on high-pressure hydrogen storage vessels. *Energy Storage Science and Technology*, 10(5), 1835.
- [6] Staykov, A., Yamabe, J., & Somerday, B. P. (2014). Effect of hydrogen gas impurities on the hydrogen dissociation on iron surface. *International Journal of Quantum Chemistry*, 114(10), 626-635.
- [7] Sun, B., Bao, L., & Luo, Q. (2021). Technology development and trend of in-cylinder direct injection hydrogen fuel internal combustion engine. *Journal of Automotive Safety and Energy Conservation*, 12(03):265-278.
- [8] Tsujimura, T., & Suzuki, Y. (2023). Development of a large-sized direct injection hydrogen engine for a stationary power generator. *International Journal of Hydrogen Energy*, 44(22), 11355-11369. doi: <https://doi.org/10.1016/j.ijhydene.2018.09.178>
- [9] Verhelst, S., Turner, J. W. G., Sileghem, L., & Vancoillie, J. (2019). Methanol as a fuel for internal combustion engines. *Progress in Energy and Combustion Science*, 70, 43-88. doi: <https://doi.org/10.1016/j.peccs.2018.10.001>
- [10] Pani, A., & Burla, V. S. S. U. T. (2020). Formation, Kinetics and Control Strategies of Nox Emission in Hydrogen Fueled IC Engine. *Int J Eng Res*, 9, IJERTV9IS010081.
- [11] Wallner, T., Nande, A. M., & Naber, J. D. (2009). Study of basic injection configurations using a direct-injection hydrogen research engine. *SAE International Journal of Engines*, 2(1), 1221-1230.
- [12] Yang, X., Wang, X., Dong, Q., Ni, Z., Song, J., & Zhou, T. (2022). Experimental study on the two-phase fuel transient injection characteristics of the high-pressure natural gas and diesel co-direct injection engine. *Energy*, 243, 123114. doi: <https://doi.org/10.1016/j.energy.2022.123114>
- [13] Nakagawa, K., Yamane, K., & Ohira, T. (2012). Potential of large output power,

- high thermal efficiency, near-zero NO_x emission, supercharged, lean-burn, hydrogen-fuelled, direct injection engines. *Energy Procedia*, 29, 455-462. doi: <https://doi.org/10.1016/j.egypro.2012.09.053>
- [14] Franken, T., Mauss, F., Seidel, L., Gern, M. S., Kauf, M., Matrisciano, A., & Kulzer, A. C. (2020). Gasoline engine performance simulation of water injection and low-pressure exhaust gas recirculation using tabulated chemistry. *International Journal of Engine Research*, 21(10), 1857-1877. doi: <https://doi.org/10.1177/1468087420933124>
- [15] Lázaro, M. J., Galvez, M. E., Ascaso, S., Suelves, I., Moliner, R., & Pieta, I. (2011). Catalytic technologies for diesel engines exhaust gas cleaning. *Catalysis: Principles, Types and Applications*: Nova Science Publishers.
- [16] Koch, D. T., Sousa, A., & Bertram, D. (2019). H₂-Engine operation with EGR achieving high power and high efficiency emission-free combustion (No. 2019-01-2178). SAE Technical Paper.

Article copyright: © 2024 Mengfei Liu. This is an open access article distributed under the terms of the [Creative Commons Attribution 4.0 International License](https://creativecommons.org/licenses/by/4.0/), which permits unrestricted use and distribution provided the original author and source are credited.



Effect of Hydrogen Injection Flow Rate on the Performance of In-Cylinder Direct Injection Hydrogen Engines

Honglin Ma*

North China University of Water Resources and Electric Power, Zhengzhou City, Henan

Received July 7, 2024; Accepted August 5, 2024; Published August 17, 2024

When a hydrogen internal combustion engine uses intake manifold injection to supply hydrogen, it must face the contradiction of abnormal combustion (premature combustion, backfire, etc.). The occurrence of abnormal combustion such as backfire can be avoided by using in-cylinder direct injection of hydrogen. In this paper, the In-Cylinder Direct Injection single-cylinder engine is modified, a three-dimensional simulation model is established, and simulation tests using AVL-Fire software on this basis is conducted. Through the analysis of the research results, the optimal hydrogen injection flow rate for the direct injection hydrogen engine to achieve the best power and economy under different working conditions was obtained. The results show that: under the same speed and load, the increase of hydrogen injection flow rate increases the hydrogen injection speed, which promotes the turbulent motion in the cylinder. At the same time, with the increase of hydrogen injection flow rate, the maximum pressure, temperature, indicated power and indicated thermal efficiency in the engine cylinder generally show a trend of first increasing and then decreasing, and there is an optimal hydrogen injection flow rate value.

Keywords: Hydrogen fuel; Hydrogen injection flow rate; In-cylinder direct injection

Introduction

Currently, due to the increasingly serious energy shortage and greenhouse gas problems, the transportation industry is actively exploring the use of clean renewable energy to replace fossil fuels to solve these problems [1, 2]. Hydrogen has zero carbon emissions and renewable energy characteristics, and can be used as an alternative fuel for traditional internal combustion engines [3, 4]. The future direction of engine technology is zero-carbon internal combustion engine, which is regarded as the future trend in the engine field [5]. In particular, hydrogen engines, as a zero-carbon energy solution, have great potential in addressing global energy challenges and mitigating climate change [6, 7].

Over the past few decades, as environmental issues and global warming have become increasingly serious, major automobile producing countries have been working hard to develop clean energy vehicles [8, 9]. Various factors are driving the shift from traditional engine fuels to low-carbon or zero-carbon [10]. Hydrogen is expected to become an ideal alternative fuel for internal combustion engines due to its low conversion cost, excellent combustion performance, zero carbon emissions and

*Corresponding author: mhl416@163.com

renewable potential [11, 12]. The in-cylinder direct injection hydrogen engine can completely avoid backfire by injecting hydrogen after the intake valve is closed [13-15]. In-cylinder direct injection hydrogen engine technology has become a hot topic in recent years, which can increase power output by more than 17% [16, 17].

In the field of hydrogen engines, there exist two dominant injection technologies, *i.e.*, direct in-cylinder injection (DI) and port-feed injection (PFI). Among them, PFI hydrogen engines often have problems such as backfire and detonation during use. These adverse factors can easily cause damage to the engine itself and the intake system, which has been confirmed in many studies [18-20]. As a result, DI hydrogen engines have regained the attention of scholars around the globe, because they can significantly avoid such problems. DI technology is able to completely eliminate the risk of backfiring and detonation by injecting hydrogen directly into the engine cylinders and also helps to increase the power output of the engine [21]. However, this technology also faces some challenges, such as how to effectively organize the airflow in the cylinder to optimize the mixing of hydrogen and air, while avoiding uneven combustion of the mixture and excessive combustion temperature, thereby reducing heat transfer losses and NO_x emissions. These requirements make the control strategy of DI hydrogen engines more complex and sophisticated [22].

Wallner *et al.* [23] provided an in-depth review of the effect of injection strategy on the performance of direct-injection hydrogen engines. The data from their study showed that the implementation of a dual injection technique was able to significantly reduce NO_x emissions compared to a single injection technique at an engine speed maintained at 1000 rpm and an Indicated Mean Effective Pressure (IMEP) of 6 bar. Further analysis revealed that when the direction of the hydrogen jet was aligned with the spark plug, either towards or away from the spark plug, the thermal efficiency of the engine was significantly improved. In particular, the indicated efficiency peaked at 31% in the case of hydrogen injection to the spark plug and the ratio of hydrogen between the two injections was optimized to be 7:3.

The study by Park *et al.* [24], on the other hand, revealed the effect of delayed start of injection (SOI) on engine performance. They found that the change in air-fuel ratio caused by delayed SOI had a greater impact on engine performance than the effect of reduced mixing time. Specifically, delayed SOI leads to an increase in fresh air intake and air-fuel ratio. As a result, although the mixing time of hydrogen and air is shortened, the engine's torque and thermal efficiency are improved.

Another study conducted by Yosri *et al.* [25] revealed another effect of SOI delay on engine performance. They found that the mixture layer around the spark plug became very thin when the SOI was delayed, which led to a decrease in the combustion rate and a reduction in thermal efficiency.

Hamada *et al.* [26], on the other hand, experimentally investigated the effect of equivalence ratio and SOI on the combustion characteristics of a direct injection hydrogen engine at an injection pressure of 18 bar. Their results showed that the mixture stratification achieved by delayed SOI can lead to earlier combustion initiation and shorter combustion duration compared to early partial direct injection.

A study by Naganuma *et al.* [27] categorized the injection and ignition strategies for DI hydrogen engines into three groups: early injection with premixed ignition (EI-PMI), late injection with pre-chamber ignition (LI-PHi), and late injection with post-chamber ignition (LI-PTi). The results of the study show that the EI-PMI mode performs well in reducing NO_x emissions, while the LI-PTi mode demonstrates a high thermal

efficiency in combination with EGR technology under high load conditions. The optimization resulted in a 1000 ppm reduction in NO_x emissions, while maintaining a stable thermal efficiency throughout the load range, with a maximum Maximum thermal efficiency of 45%.

On the other hand, Oikawa *et al.* [28] proposed the plume combustion concept (PCC) for hydrogen engines, which involves injecting hydrogen near the top dead center and igniting the hydrogen-rich plume at the end to achieve diffusion combustion of the hydrogen-rich mixture. This strategy significantly reduced NO_x emissions and cooling losses. Further studies have shown that delaying hydrogen injection time can improve thermal efficiency but will also lead to increased NO_x emissions.

A study by Wei *et al.* [29] showed that late injection has a positive effect on increasing the thermal efficiency of the engine. This effect was mainly attributed to stratified combustion due to late injection, which reduces heat transfer losses. However, they also observed a significant rise in NO_x emissions with late injection.

Using CFD simulations, the study by Rottenruber *et al.* [30] found that the mixture homogeneity was slightly improved as the direct hydrogen injection pressure was increased from 4 MPa to 15 MPa. This was attributed to the fact that the higher injection pressure increased the turbulent kinetic energy in the cylinder and enhanced the mixing process, thus improving the thermal efficiency.

In summary, compared with the hydrogen engine using inlet channel hydrogen injection, the in-cylinder direct-injection hydrogen engine eliminates the problem of hydrogen occupying the cylinder volume and the possibility of backfire. The direct-injection hydrogen combustion engine has a wider range of excess air coefficients, which allows it to adopt a thinner combustion mode. However, the control strategy of direct-injection hydrogen engine is more complicated, and the improvement of thermal efficiency has a stronger correlation with the increase of emissions. At present, research focuses on the operating parameters of direct-injection hydrogen engines, such as ignition timing, hydrogen injection timing, and equivalence ratio, etc. There is a relative lack of research on the structural parameters of the in-cylinder direct-injection hydrogen, economy and emission of the direct injection hydrogen engine can provide certain theoretical support and data support for the study of the structural parameters of the in-cylinder direct injection hydrogen engine, which plays an important role in the study of the in-cylinder direct injection hydrogen engine.

Based on the characteristics of hydrogen fuel, especially its high anti-knock performance in dilute mixtures, NO_x emissions increase. The combustion of a lean mixture of fuel and air has always been a traditional method to improve thermal efficiency and reduce NO_x. Currently, a mixture of hydrogen and air is formed by injecting hydrogen at the beginning of the compression stroke. However, even under lean mixture conditions, such mixing conditions do not always provide the expected thermal efficiency improvement because mixture inhomogeneity and incomplete flame propagation in the very lean portion can also lead to increased emissions of unburned hydrogen. Therefore, in this paper, the thermal efficiency of a hydrogen internal combustion engine is improved by adopting different hydrogen injection flow rates and controlling the hydrogen injection timing (generally injected in the later stage of the compression stroke) to optimize the distribution of the mixture in the cylinder and reduce exhaust emissions. At the same time, it also explores the impact of different hydrogen injection flow rates on the overall performance of the internal combustion engine. By analyzing the effects of different hydrogen injection flow rates on the in-cylinder mixture

and thus on the emissions and performance of the internal combustion engine, the optimal working conditions are derived on this basis. This provides a theoretical basis for the early realization of large-scale popularization of hydrogen engines.

Computational Model and Research Program

Research Object and Geometric Model

In this paper, the single-cylinder Gasoline Direct Injection (GDI) test engine is used as a prototype, and further modified and designed according to the original size data of the prototype, which is transformed into a variable compression ratio in-cylinder direct-injection hydrogen engine to meet the requirements of the experiment. The technical parameters as well as key points of the experimental engine after the modification is completed are shown in Tables 1 and 2, respectively:

Table 1. Engine technical parameters

Engine Parameter	Parameter Value
Displacement (ml)	1054
Cylinder Bore (mm)	108
Piston Stroke (mm)	115
Connecting Rod Length (mm)	137
Valve Number (pcs)	2
Maximum Power (w)	6000
Maximum Torque (N.m)	4500
Ignition System	Spark Ignition Systems

Table 2. Working cycle and key nodes

Key points of the experimental engine	Corresponding Crank Angle Range
Valve Overlap	351~394°CA
Intake	394~634°CA
Compression	634-866°CA
Exhaust	866-1071°CA
Upper Stop	360°CA/720°CA
Lower Stop	540°CA/900°CA
Intake Valve Open	351°CA
Intake Valve Closed	634°CA
Exhaust Valve Open	866°CA
Exhaust Valve Closed	394°CA

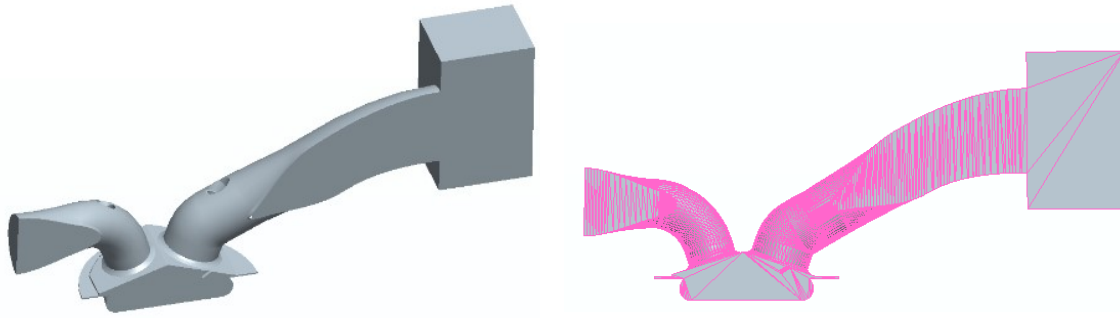


Fig. 1. Engine geometry and mesh model

Grid Division

In the actual operation of the engine, the various parts and the internal space are in the dynamic changes. In order to accurately calculate the entire computer numerical simulation process, initial grid division is required. According to the engine working process, it is divided into valve overlap part, intake part, compression part and exhaust part. The calculation grid can be adjusted according to the requirements of the experiment. To ensure the accuracy of the experiment and the overall efficiency of the experiment, this paper adopts AVL-FIRE software for grid division. The specific process is as follows:

(1) The division of the surface grid and the line grid, the definition and division of the selections of the surface grid will directly affect the subsequent experimental settings and the accuracy of the boundary conditions and initial conditions of the computational process. When drawing the line grid, we use the AVL-FIRE software line grid automatic generation tool, which requires us to set the minimum angle and length of the closed curve according to the specific requirements of the experiment.

(2) Dynamic mesh division, dynamic mesh division is a key link in the simulation of engine internal fluid dynamics. The Fame Engine Plus dynamic mesh module in AVL-FIRE software is used for the complex mesh division process. The steps include: Creating and configure the fep file, importing the geometric data containing the surface mesh and line mesh, sub-dividing the mesh according to the different operating cycles of the engine (manifested as the range of crankshaft angle changes), determining the trajectory of the piston surface and its direction, setting up a reasonable value of the valve lash, and importing a valve lift curve file to further define the mesh in a refined way. The quality of the mesh is evaluated by color coding, with green indicating high quality and suitable for computation, yellow indicating average quality and barely usable, and red indicating low quality and not usable for computation. After the above series of steps, high quality dynamic mesh data that meets the requirements is successfully generated and exported to fmo file for subsequent calculation and analysis.

Initial Conditions and Boundary Conditions

In this paper, the initial conditions mainly refer to the pressure and temperature in the intake and exhaust tracts and cylinders at the beginning of the calculation, which need to be met at 351°C. At this time, the engine state is that the intake valve has just opened. In the early stage of valve stacking period, in order to ensure the calculation speed, accuracy and convergence of the results, it is assumed that the gas satisfies the ideal gas state equation, and the external conditions and the initial state of the engine all meet the

ideal state. It also assumes that the initial intake tract is full of fresh air, and the cylinder and the exhaust tract are the combustion exhaust from the previous cycle. At the same time, it is necessary to set corresponding boundary conditions for each region of the engine. The boundary conditions mainly include import and export boundaries, wall boundaries, and symmetry surface boundaries. The wall boundaries are divided into fixed walls and moving walls. Various boundaries are mainly divided into pressure and temperature types, according to the actual process of the corresponding type of setting. As shown in Tables 3 and 4, the air inlet and exhaust port are inlet and outlet boundaries, and the type is set to pressure boundary; the inlet and exhaust channels are fixed wall boundaries, and the inlet and exhaust valves are moving wall boundaries, and the type is set to thermostatic boundary, and so on.

Table 3. Setting of initial conditions

Parameters	Intake Tract	Combustion Chamber	Exhaust Tract
Temperature (K)	293	950	900
Pressure (MPa)	0.1	0.108	0.106

Table 4. The setting of boundary conditions

Boundary area	Boundary types	Set Values
Air inlet	Inlet	0.1 MPa
Exhaust Air Outlet	Outlet	0.106 MPa
Air Inlet	Stationary wall	300 K
Exhaust tract	Stationary wall	600 K
Inlet valve seat	Stationary wall	450 K
Exhaust Valve Seat	Stationary wall	650 K
Intake Valve	Moving wall	500 K
Exhaust Valve	Moving wall	750 K
Cylinder Wall	Stationary wall	470 K
Piston	Moving wall	580 K
Cylinder head	Stationary wall	580K
Symmetrical surface	Symmetry	580 K

Model Validation

To verify the reliability of the model, the model was validated under normal combustion conditions when the JH600 engine was converted into a hydrogen internal combustion engine. The engine specifications include a cylinder bore of 94 mm, a stroke of 85 mm, and a compression ratio of 15:1. During the test, the engine was operated at a speed of 3000 r/min with an equivalent transmission ratio of 0.4. The injection timing was set at 394 °CA and the ignition advance angle was 715 °CA. The average in-cylinder pressure was chosen as the comparison parameter, and the results are shown in Figure 2.

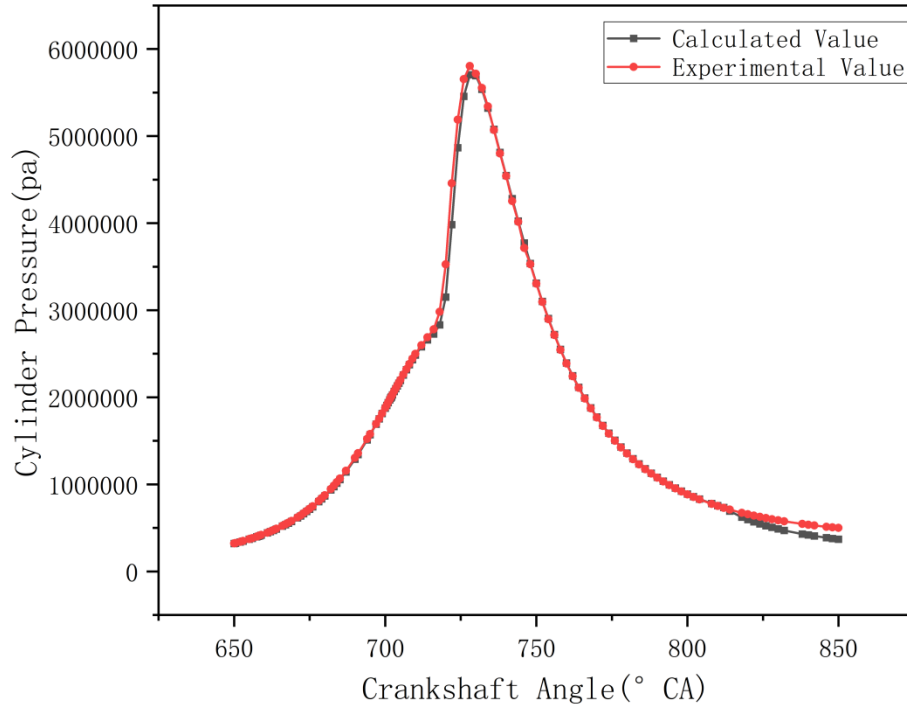


Fig. 2. Comparison of test and simulation in-cylinder pressure

Figure 2 shows that the relative error between test data and simulation data is within 5%, which is within the allowable error range. Therefore, the improved model method in this paper can effectively reflect the actual operation process of the direct injection hydrogen engine, and the simulation results are practical and reliable.

Results

The Effect of Hydrogen Injection Flow on the In-Cylinder Mixture Velocity Field under Different Working Conditions

Figure 3 shows the in-cylinder velocity field at different hydrogen injection flow rates and moments. The effect of hydrogen injection flow rate on the mixture of the in-cylinder direct injection hydrogen engine is mainly concentrated in the second half of the process of the piston upward after the intake is closed. It can be seen from the cloud diagram that in the pre-injection of hydrogen, a high-speed hydrogen jet begins to appear and concentrates in the axial direction of the hydrogen injection hole, impacting the cylinder wall and a part of the high speed of the hydrogen jet as the piston. After impacting the cylinder wall, part of the high-speed hydrogen jet moves with the bottom of the piston, and part of it moves upward along the cylinder wall. At the same time, with the crankshaft running the piston upward, part of the fuel forms a new vortex at the bottom of the cylinder under the influence of the piston movement after contacting the cylinder wall. When influenced by the structure of the piston combustion chamber, the hydrogen jet will expand its vortex after hitting the bottom of the piston, causing the flow

velocity of the mixture at the bottom of the piston to accelerate and gradually develop upwards. At the end of the piston stroke, the turbulent flow developing upward from the bottom of the piston contacts the top surface of the combustion chamber, forming a front that increases the flow velocity of the mixture at the bottom of the spark plug, which is beneficial for improving the flame propagation speed. At the same time, as the hydrogen injection flow rate increases, the flow rate of the mixture in the cylinder also increases, enhancing the turbulent movement in the cylinder. Compared with the low-flow situation, at the end of the compression stroke, the velocity of the mixture in the cylinder is more concentrated and evenly distributed, and the turbulent movement near the spark plug is stronger, which is more conducive to the formation of the flame front, thereby facilitating the propagation of the combustion flame and accelerating the combustion speed.

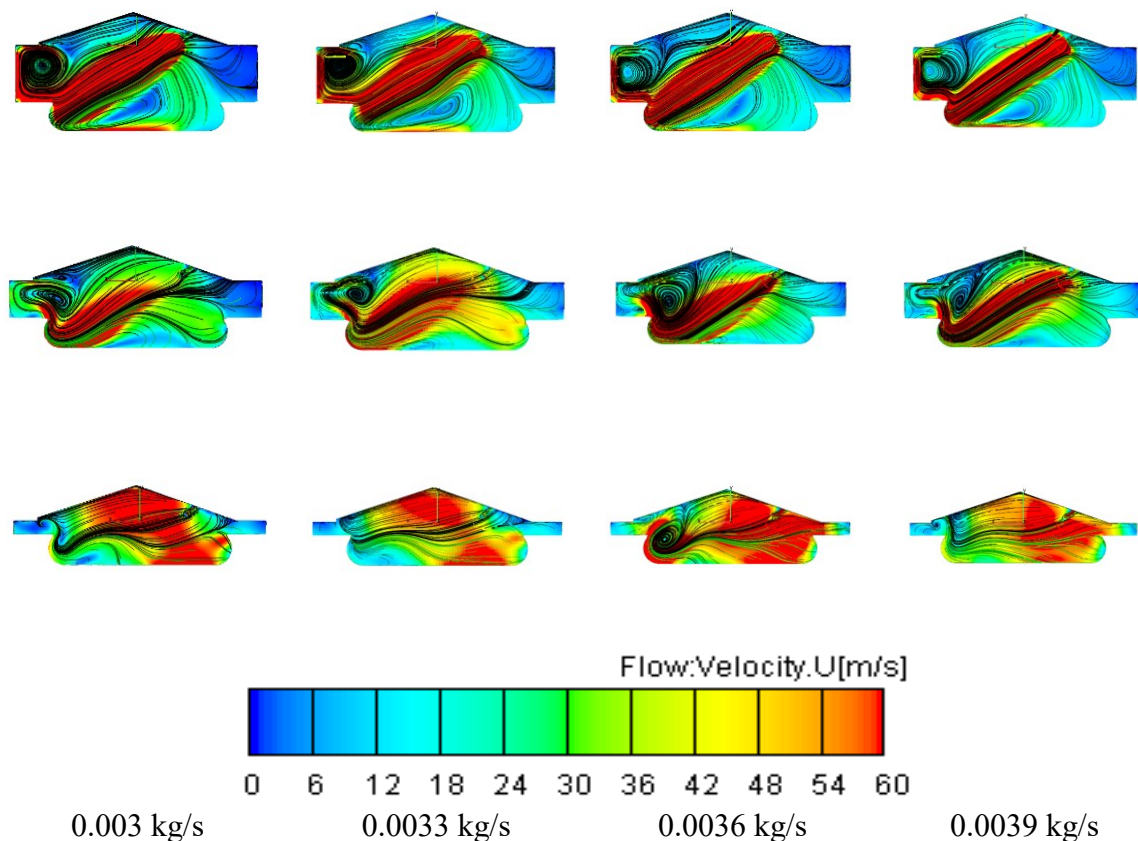


Fig. 3. Variation of velocity field of cylinder mixture with hydrogen injection flow rate

Influence of Hydrogen Injection Flow Rate on Cylinder Pressure and Temperature of Direct-Injection Hydrogen Engine under Different Working Conditions

During the operation of a direct injection hydrogen engine, the changing trends of the pressure and temperature in the cylinder are important indicators of the fuel combustion performance. This paper summarizes the changing trends of the maximum pressure and temperature in the cylinder under various operating conditions, analyzes the changing trends of the maximum pressure and temperature, and explores the influence of

the hydrogen injection flow rate on the changing trends of the maximum pressure and temperature in the cylinder of a direct injection hydrogen engine.

Figure 4 shows the trend of the maximum in-cylinder pressure with the hydrogen injection flow rate under different operating conditions. In Figure 4(a), it can be seen that the maximum in-cylinder pressure increases with the increase of load at 3000 r/min, which is due to the fact that when the load is increased to achieve the target equivalence ratio, the mass of the combustible mixture in the cylinder increases, and more combustible mixture is involved in combustion. As a result, the maximum pressure in the cylinder is further increased. In addition, under most working conditions, the maximum pressure in the cylinder increases first and then decreases with the increase of hydrogen injection flow rate. Under medium and high load conditions, the maximum pressure in the cylinder generally reaches its peak at 0.029kg/h. However, under low load conditions, the maximum pressure in the cylinder reaches its peak level at 0.026kg/h and gradually decreases with the increase of flow. This is because after the hydrogen reaches the target equivalence ratio, in order to increase the mass of the combustible mixture in the cylinder, more combustible mixture participates in the combustion. The highest pressure in the figure gradually decreases after reaching its peak, because hydrogen has a wide ignition limit, strong diffusion ability, and fast flame propagation speed after ignition. Under low-speed and low-load conditions, a larger hydrogen injection flow rate shortens the duration of hydrogen injection, and the diffusion ability of hydrogen is strong. Hydrogen rapidly diffuses in the cylinder to form a relatively dilute mixture. In addition, the higher hydrogen injection flow rate also accelerates the gas flow velocity inside the cylinder, and the turbulent motion of the mixture also accelerates the diffusion of hydrogen gas, forming a relatively lean mixture and ultimately leading to a decrease in the maximum pressure inside the cylinder during combustion. The increase in mixture turbulence also accelerates the diffusion of hydrogen, forming a leaner mixture and causing a decrease in the maximum pressure in the cylinder during combustion. Under medium and high load conditions, in order to achieve the target equivalence ratio, it is necessary to adjust the size of the hydrogen injection flow rate to achieve a good distribution of the mixture in the cylinder. The smaller the hydrogen injection flow rate, the longer the hydrogen injection duration is required, which is not conducive to the enrichment of hydrogen. When the hydrogen injection flow rate is large, the hydrogen injection duration is greatly shortened, which intensifies the fuel diffusion. Finally, the best mixture is obtained at 0.0029kg/h, and the combustion state is the best at this time.

Figures 4 (b) and (c) show the trend of the maximum in-cylinder pressure at 4500 r/min and 6000 r/min under each working condition with the increase of different hydrogen injection flow rates, respectively. From the overall point of view, with the increase of rotational speed, the maximum in-cylinder pressure under various working conditions increases to varying degrees compared with 3000 r/min. As the engine speed increases, the piston movement of the engine intensifies. The only way to achieve stratified combustion is to increase the hydrogen injection flow rate while keeping the hydrogen injection timing unchanged, so that the fuel near the spark plug becomes concentrated. At medium and high speeds, the maximum in-cylinder pressure first increases and then decreases with the increase of flow rate. The optimal hydrogen injection flow rate increases from 0.0026kg/h at 3000r/min to 0.0036kg/h and 0.0041kg/h. This is because the in-cylinder pressure increases to varying degrees with the increase of speed. This is because as the rotation speed increases, the flow rate of the mixed gas in the cylinder increases. The initial turbulence intensity in the cylinder increases, and it is

necessary to increase the hydrogen injection flow rate to improve the penetration of the hydrogen jet, reduce the duration of the hydrogen injection cycle, and achieve local hydrogen-rich stratified combustion. At the same time, under medium and low loads, with the increase in hydrogen injection flow rate, the increase in the maximum pressure in the cylinder is large and the change range is large, while under high loads, the increase in the maximum pressure in the cylinder is small, that is, the maximum pressure in the cylinder is low at low loads, and the increase in the maximum pressure in the cylinder is large at high loads. This shows that the maximum pressure in the cylinder is strongly influenced by the hydrogen injection flow rate when the load is small.

In general, under different working conditions, the maximum in-cylinder pressure increases and then decreases with the increase of hydrogen injection flow rate, and there exists an optimal hydrogen injection flow rate. In addition, with the increase of rotational speed, the optimal flow rate of hydrogen injection in the cylinder is also increased accordingly, and the change of cylinder pressure under high load is significantly less affected by the flow rate than that of the low and medium load conditions. Therefore, when the working state of the direct injection engine changes, the appropriate flow rate needs to be adjusted to achieve optimal performance.

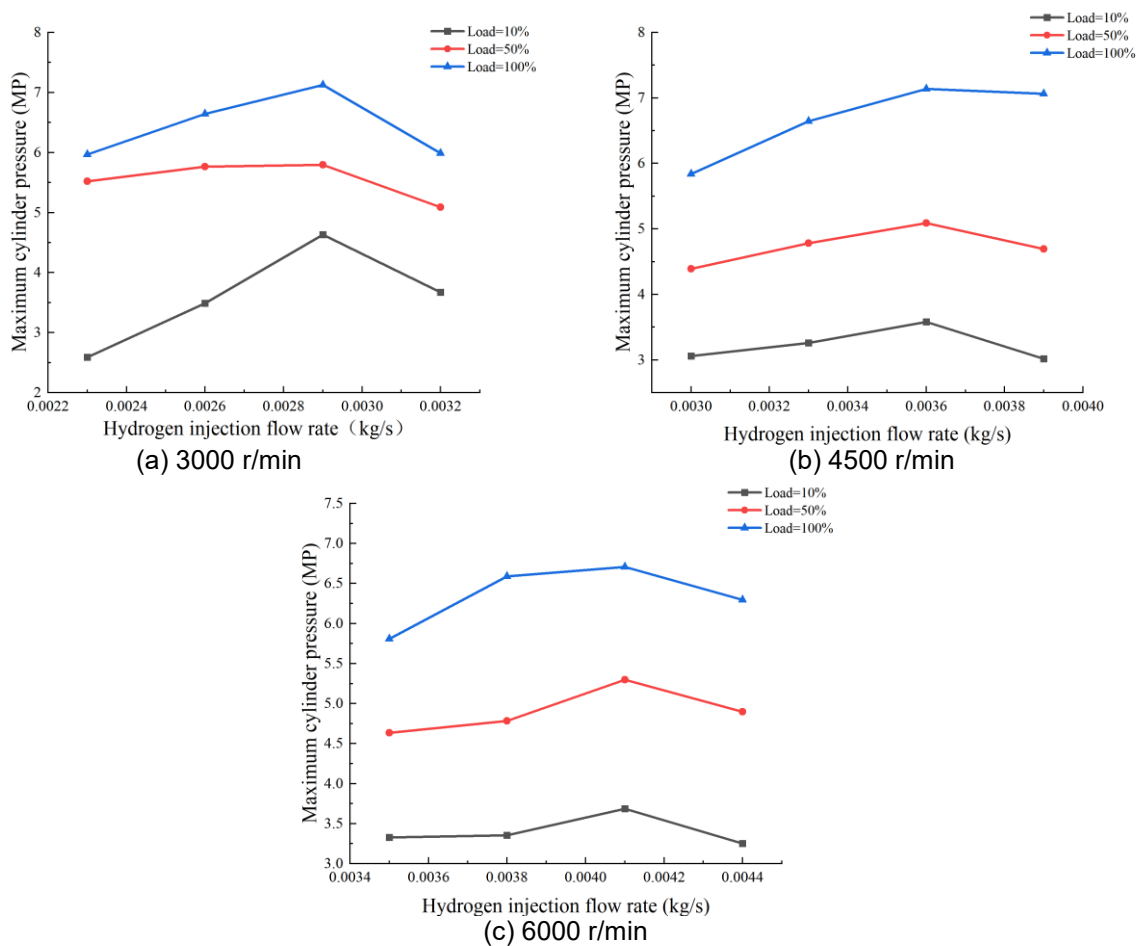


Fig. 4. The variation of the maximum in-cylinder pressure with the hydrogen injection flow rate under different working conditions

Figure 5 shows the trend of the maximum in-cylinder temperature with the hydrogen injection flow under different working conditions of the in-cylinder direct-injection hydrogen engine at engine speeds of 3000 r/min, 4500 r/min, and 6000 r/min. It can be seen from the figure that under different working conditions and different speeds, the maximum temperature in the cylinder shows a trend of first increasing and then decreasing with the increase of hydrogen injection flow rate. When the hydrogen injection flow rate is 3 000 r/min, the maximum temperature in the cylinder reaches a peak at 0.0029 kg/h. When the cylinder temperature reaches the peak value, the minimum hydrogen injection flow rate is 0.0029kg/h. As the speed increases further, the highest cylinder temperature is obtained when the hydrogen injection flow rate is 0.0036kg/h at 4500 r/min, and the cylinder temperature reaches the peak value when the hydrogen injection flow rate is 0.0041kg/h at 6000 r/min. This is because, compared with other hydrogen injection flow rates, the combustion conditions under this condition are significantly better than other conditions. Stratification occurs in the mixture in the cylinder, the hydrogen fuel is enriched near the spark plug, and the combustion speed is fast, resulting in an increase in the temperature in the cylinder.

At the same speed and different loads, as the load increases, the maximum temperature in the cylinder gradually increases. At 3000r/min, the maximum temperature is 2461K at the optimal hydrogen injection flow rate; at 4500r/min, the maximum temperature is 2661K at the optimal hydrogen injection flow rate; and at 6000r/min, the maximum temperature is 2789K at the optimal hydrogen injection flow rate. When the hydrogen injection flow rate is 0.032kg/s and the load is 100%, the maximum temperature inside the cylinder is 2789K. The greater the load, the more power the engine requires. Therefore, in order to achieve the target equivalence ratio, during the combustion process of the engine, as the amount of fuel in the cylinder increases, the total heat released by combustion also increases accordingly, which causes the maximum temperature that can be reached in the cylinder to also increase. By comparing the combustion characteristics under different operating conditions, it can be observed that there is a significant difference in the maximum temperature that can be achieved in the cylinder under low-speed and low-load conditions, compared to high-speed and high-load conditions. This is due to the longer duration of hydrogen injection at low speeds and the diffusivity of hydrogen, which tends to form a thinner mixture, leading to an increase in the duration of combustion. This reduces the stability of the combustion process and results in a lower maximum temperature in the cylinder.

From the effect of hydrogen injection flow on the maximum temperature in the cylinder, it can be seen that the overall trend of temperature change is roughly consistent with the change of the maximum pressure in the cylinder, both of which show a trend of first rising and then falling with the increase of flow. The pressure and temperature in the cylinder are relatively high during combustion under medium and high load conditions, which is conducive to improving the power of the engine. However, the high temperature and high pressure environment is the most favorable environment for the production of nitrogen oxides, the most important pollutant in the direct injection hydrogen engine. Therefore, choosing the appropriate hydrogen injection flow rate while ensuring power will minimize the generation of contamination.

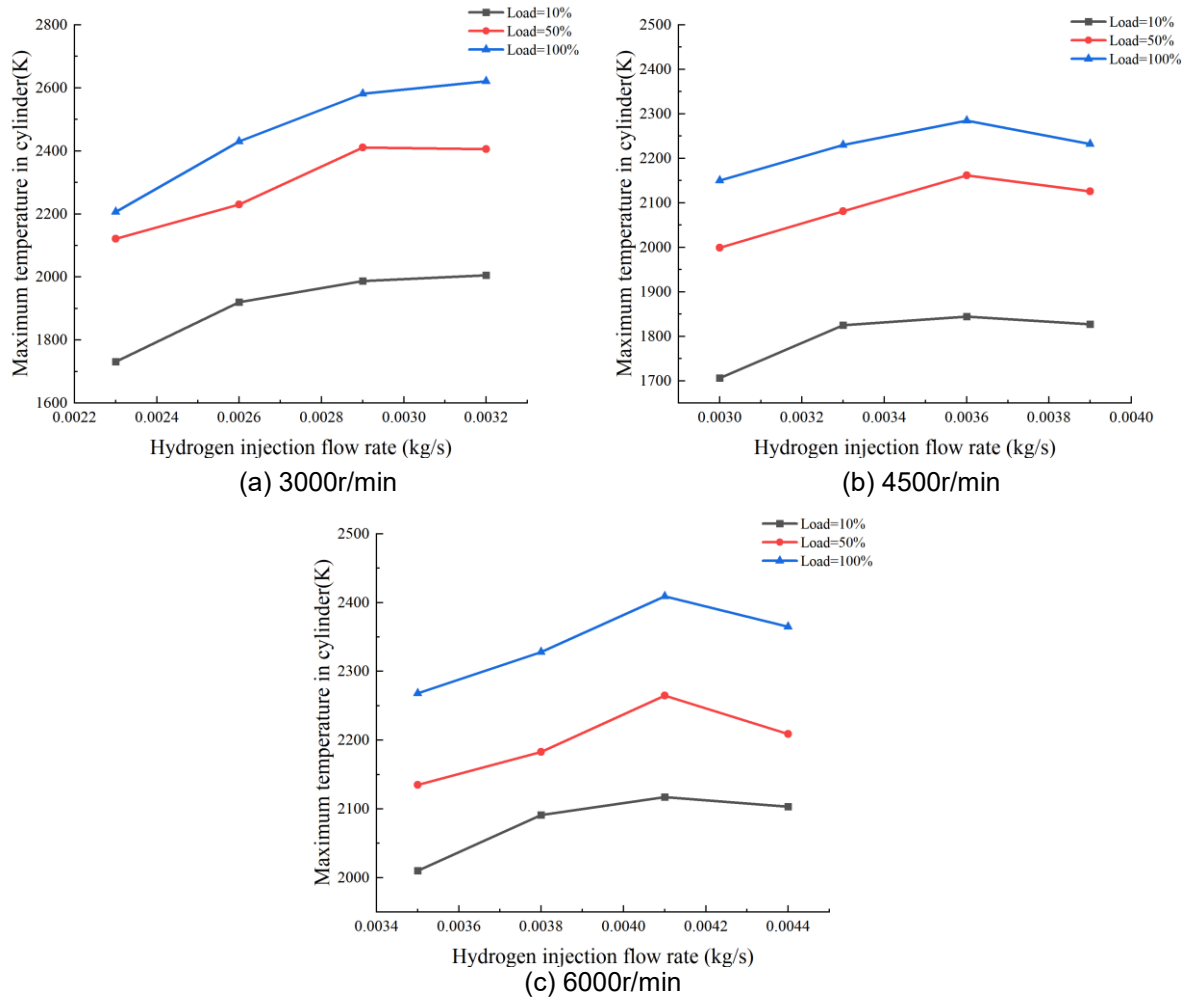


Fig. 5. The variation of the maximum temperature in the cylinder with the hydrogen injection flow

Influence of Hydrogen Injection Flow Rate on the Dynamics of In-Cylinder Direct Injection Hydrogen Engine under Different Operating Conditions

As an energy conversion device, the basic principle of an engine is to effectively convert the heat energy released by the chemical energy of the fuel into usable mechanical energy through a series of orderly working cycles. The indicated performance index of the engine is based on the work done on the piston after the combustion in the combustion chamber is completed. It can be directly reflected in a working cycle. The quality of the work done on the piston in the cylinder after the combustion is completed is an important parameter for evaluating the comprehensive performance of the engine. The indicated power refers to the indicated work done by the combustion engine per unit time, and the unit is KW. The indicated power is an important parameter for evaluating the power of the engine. Its calculation formula is as follows:

$$P_i = \frac{W_i n i}{30 \tau} \quad \text{Eq. 1}$$

$$W_i = \int p dV \quad \text{Eq. 2}$$

where n is the engine speed with a unit of r/min, i is the number of cylinders, τ is the number of engine strokes, and W_i is the engine indicated power.

The variation trend of indicated power under different operating conditions with hydrogen injection flow rate obtained in this section based on the simulation of the full experimental design scheme is shown in Figure 6. The indicated power of each working condition increases to varying degrees with the increase of rotational speed. This is because the higher the speed, the shorter the unit working cycle time of the engine, the more intense the turbulent motion in the cylinder, the more intense the piston motion, and the better the engine power. At the same time, under the same compression ratio, the indicated power of the engine increases as the load increases. At low load, as the hydrogen injection flow rate increases, the indicated power of the engine changes rapidly. Under high load conditions, the change of the indicated power is relatively gentle. Under low and medium load conditions, the indicated power of the engine is greatly affected by the hydrogen injection flow rate. And as the load increases, the influence of the hydrogen injection flow rate on the change of the indicated power of the engine is small.

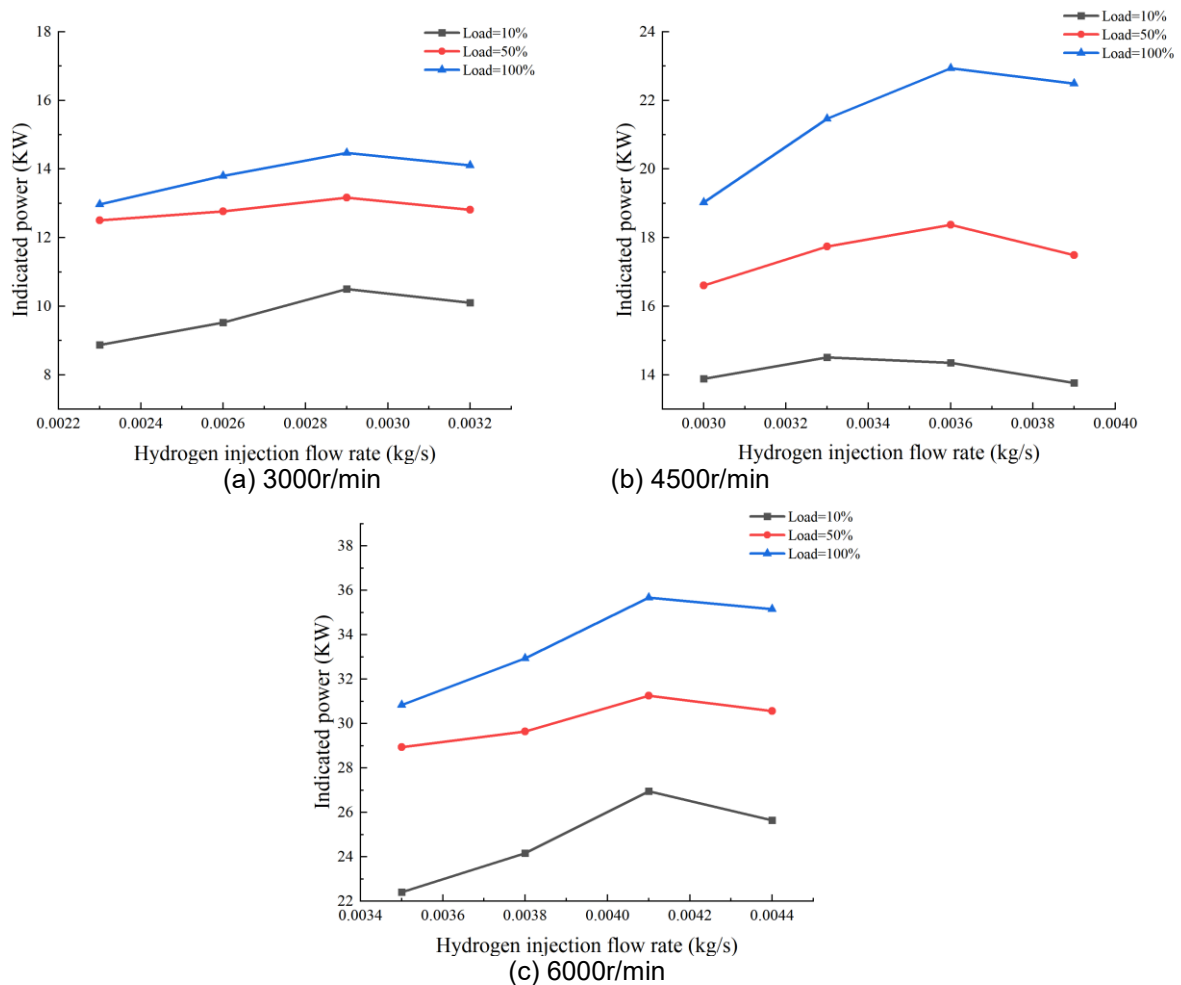


Fig. 6. The effect of hydrogen injection flow rate on the indicated power under different working conditions.

By analyzing the effect of hydrogen injection flow on the engine indicated power under different working conditions, it can be seen that the trend of the indicated power of the hydrogen engine under various working conditions is generally the same as the trend of the highest pressure in the cylinder. The change of combustion pressure in the cylinder

can reflect the ability of the fuel to convert chemical energy into thermal energy and then into mechanical energy for external output, while the corresponding relationship between pressure in the cylinder and power ensures the accuracy of factor analysis. In general, the indicated power under each working condition gradually increases with the increase of hydrogen injection flow rate. At the same time, due to the fixed hydrogen injection time, the flow rate for obtaining the best indicated power also gradually increases. When other conditions are the same, the flow rate for obtaining the highest indicated power under low load is significantly smaller than the flow rate for obtaining the highest indicated power under medium and high loads.

Conclusion

As the hydrogen injection flow rate increases, the initial velocity of the hydrogen jet increases, thereby accelerating the flow of the mixture in the cylinder, enhancing the intensity of the turbulence in the cylinder, and increasing the vortex in the cylinder. On the one hand, it increases the collision probability between the spark plug electrode and the combustible mixture molecules, shortens the reaction time of hydrogen and oxygen, and accelerates the formation and development of the flame center. On the other hand, the enhanced in-cylinder vortex enhances the intensity of hydrogen turbulent combustion and accelerates the in-cylinder combustion process.

The maximum pressure in the cylinder increases first and then decreases with the increase of hydrogen injection flow rate, and there is an optimal hydrogen injection flow rate. In addition, as the speed increases, the optimal hydrogen injection flow rate in the cylinder also increases accordingly. Under high load conditions of 3000, 4500, and 6000 r/min, the maximum pressure in the cylinder reached its peak value when the hydrogen injection flow rate was 0.0029, 0.0036, and 0.0041 kg/s. Moreover, the change of cylinder pressure under high load is significantly less affected by flow rate than that under medium and low load. Therefore, when the operating conditions of a direct injection engine change, the appropriate flow rate needs to be adjusted to achieve optimal performance. The overall trend of the maximum temperature change in the cylinder is basically consistent with that of the maximum pressure change in the cylinder, that is, it shows a trend of first rising and then falling with the increase of flow rate. In addition, the combustion pressure and temperature in the cylinder are relatively high under medium and high load conditions, which is conducive to improving the engine power. By analyzing the effect of hydrogen injection flow rate on engine power under different working conditions, it can be seen that the overall trend of the indicated power of the hydrogen engine under various working conditions is roughly the same as the trend of the maximum pressure in the cylinder.

CONFLICTS OF INTEREST

The author declares that there is no conflict of interests regarding the publication of this paper.

References

- [1] Abedin, M. J., Masjuki, H. H., Kalam, M. A., Sanjid, A., Rahman, S. M. A., & Masum, B. M. (2013). Energy balance of internal combustion engines using alternative fuels. *Renewable and Sustainable Energy Reviews*, 26, 20-33. doi:<https://doi.org/10.1016/j.rser.2013.05.049>
- [2] Al-Maamary, H. M., Kazem, H. A., & Chaichan, M. T. (2016). Changing the energy profile of the GCC States: A review. *International Journal of Applied Engineering Research (IJAER)*, 11(3), 1980-1988.
- [3] Yang, Z., Wu, J., Yun, H., Zhang, H., & Xu, J. (2022). Diagnosis and control of abnormal combustion of hydrogen internal combustion engine based on the hydrogen injection parameters. *International Journal of Hydrogen Energy*, 47(35), 15887-15895. doi:<https://doi.org/10.1016/j.ijhydene.2022.03.031>
- [4] Eichlseder, H., Wallner, T., Freymann, R., & Ringler, J. (2003). *The potential of hydrogen internal combustion engines in a future mobility scenario* (No. 2003-01-2267). SAE Technical Paper.
- [5] Shih, C. F., Zhang, T., Li, J., & Bai, C. (2018). Powering the Future with Liquid Sunshine. *Joule*, 2(10), 1925-1949. doi:<https://doi.org/10.1016/j.joule.2018.08.016>
- [6] Hosseini, S. E., & Butler, B. (2020). An overview of development and challenges in hydrogen powered vehicles. *International Journal of Green Energy*, 17(1), 13-37. doi:<https://doi.org/10.1080/15435075.2019.1685999>
- [7] Sun, Z., Hong, J., Zhang, T., Sun, B., Yang, B., Lu, L., Li, L., & Wu, K. (2023). Hydrogen engine operation strategies: Recent progress, industrialization challenges, and perspectives. *International Journal of Hydrogen Energy*, 48(1), 366-392. doi:<https://doi.org/10.1016/j.ijhydene.2022.09.256>
- [8] Saeidi, S., Fazlollahi, F., Najari, S., Iranshahi, D., Klemeš, J. J., & Baxter, L. L. (2017). Hydrogen production: Perspectives, separation with special emphasis on kinetics of WGS reaction: A state-of-the-art review. *Journal of Industrial and Engineering Chemistry*, 49, 1-25. doi:<https://doi.org/10.1016/j.jiec.2016.12.003>
- [9] Shahbek, S. A. (2017). *The Policy Trade-off Between Energy Security and Climate Change in the GCC States* (Master's thesis, Hamad Bin Khalifa University (Qatar)).
- [10] Wu, Z.-S., Li, X., Wang, F., & Bao, X. (2019). DICP's 70th Anniversary Special Issue on Advanced Materials for Clean Energy. *Advanced Materials*, 31(50), 1905710. doi:<https://doi.org/10.1002/adma.201905710>
- [11] Arsie, I., Battistoni, M., Brancaleoni, P. P., Cipollone, R., Corti, E., Di Battista, D., ... & Zembi, J. (2023). A new generation of hydrogen-fueled hybrid propulsion systems for the urban mobility of the future. *Energies*, 17(1), 34. doi:<https://doi.org/10.3390/en17010034>
- [12] Verhelst, S. (2014). Recent progress in the use of hydrogen as a fuel for internal combustion engines. *International Journal of Hydrogen Energy*, 39(2), 1071-1085. doi:<https://doi.org/10.1016/j.ijhydene.2013.10.102>
- [13] Gao, J., Wang, X., Song, P., Tian, G., & Ma, C. (2022). Review of the backfire occurrences and control strategies for port hydrogen injection internal combustion engines. *Fuel*, 307, 121553. doi:<https://doi.org/10.1016/j.fuel.2021.121553>
- [14] Babayev, R., Andersson, A., Dalmau, A. S., Im, H. G., & Johansson, B. (2021). Computational characterization of hydrogen direct injection and nonpremixed combustion in a compression-ignition engine. *International Journal of Hydrogen Energy*, 46(35), 18678-18696. doi:<https://doi.org/10.1016/j.ijhydene.2021.02.223>

- [15] Chen, B., Li, L., & Zhao, X. (2007, 26-31 July 2007). *Fault Diagnosis Method to Internal-combustion Engine Based on Integration of Scale-wavelet Power Spectrum, Rough Set and Neural Network*. Paper presented at the 2007 Chinese Control Conference. doi:<https://doi.org/10.1109/CHICC.2006.4346846>
- [16] Yip, H. L., Srna, A., Yuen, A. C. Y., Kook, S., Taylor, R. A., Yeoh, G. H., ... & Chan, Q. N. (2019). A review of hydrogen direct injection for internal combustion engines: towards carbon-free combustion. *applied sciences*, 9(22), 4842. <https://doi.org/10.3390/app9224842>
- [17] Wimmer, A., Wallner, T., Ringler, J., & Gerbig, F. (2005). *H₂-direct injection—a highly promising combustion concept* (No. 2005-01-0108). SAE technical paper.
- [18] Yu, X., Li, Y., Liu, D., Guo, Z., Zhang, J., & Zhu, Q. (2022). Effects of second hydrogen direct injection proportion and injection timing on combustion and emission characteristics of hydrogen/n-butanol combined injection engine. *International Journal of Hydrogen Energy*, 47(75), 32330-32344. doi:<https://doi.org/10.1016/j.ijhydene.2022.07.122>
- [19] Dhyani, V., & Subramanian, K. A. (2018). Experimental investigation on effects of knocking on backfire and its control in a hydrogen fueled spark ignition engine. *International Journal of Hydrogen Energy*, 43(14), 7169-7178. doi:<https://doi.org/10.1016/j.ijhydene.2018.02.125>
- [20] Dhyani, V., & Subramanian, K. A. (2019). Control of backfire and NO_x emission reduction in a hydrogen fueled multi-cylinder spark ignition engine using cooled EGR and water injection strategies. *International Journal of Hydrogen Energy*, 44(12), 6287-6298. doi:<https://doi.org/10.1016/j.ijhydene.2019.01.129>
- [21] Sekine, K., Oikawa, M., Takagi, Y., & Sato, Y. (2013). Effect of fuel jet location and ignition point in the combustion chamber on thermal efficiency and NO_x formation in rich mixture plume ignition combustion of high pressure direct injection hydrogen engines. *Transactions of the Japan Society of Mechanical Engineers, Series B*, 79(808), 274-281.
- [22] Roy, M. K., Kawahara, N., Tomita, E., & Fujitani, T. (2012). High-pressure hydrogen jet and combustion characteristics in a direct-injection hydrogen engine. *SAE International Journal of Fuels and Lubricants*, 5(3), 1414-1425.
- [23] Wallner, T., Scarcelli, R., Nande, A. M., & Naber, J. D. (2009). Assessment of multiple injection strategies in a direct-injection hydrogen research engine. *SAE International Journal of Engines*, 2(1), 1701-1709.
- [24] Park, C., Kim, Y., Oh, S., Oh, J., Choi, Y., Baek, H., Lee, S. W., & Lee, K. (2022). Effect of fuel injection timing and injection pressure on performance in a hydrogen direct injection engine. *International Journal of Hydrogen Energy*, 47(50), 21552-21564. doi:<https://doi.org/10.1016/j.ijhydene.2022.04.274>
- [25] Yosri, M., Palulli, R., Talei, M., Mortimer, J., Poursadegh, F., Yang, Y., & Brear, M. (2023). Numerical investigation of a large bore, direct injection, spark ignition, hydrogen-fuelled engine. *International Journal of Hydrogen Energy*, 48(46), 17689-17702. doi:<https://doi.org/10.1016/j.ijhydene.2023.01.228>
- [26] Hamada, K. I., Rahman, M. M., Abdullah, M. A., Bakar, R. A., & A. Aziz, A. R. (2013). Effect of mixture strength and injection timing on combustion characteristics of a direct injection hydrogen-fueled engine. *International Journal of Hydrogen Energy*, 38(9), 3793-3801. doi:<https://doi.org/10.1016/j.ijhydene.2013.01.092>

- [27] Naganuma, K., Honda, T., Yamane, K., Takagi, Y., Kawamura, A., Yanai, T., & Sato, Y. (2010). Efficiency and emissions-optimized operating strategy of a high-pressure direct injection hydrogen engine for heavy-duty trucks. *SAE International Journal of Engines*, 2(2), 132-140.
- [28] Oikawa, M., Kojiya, Y., Sato, R., Goma, K., Takagi, Y., & Mihara, Y. (2022). Effect of supercharging on improving thermal efficiency and modifying combustion characteristics in lean-burn direct-injection near-zero-emission hydrogen engines. *International Journal of Hydrogen Energy*, 47(2), 1319-1327.
doi:<https://doi.org/10.1016/j.ijhydene.2021.10.061>
- [29] Wei, H., Hu, Z., Ma, J., Ma, W., Yuan, S., Hu, Y., Hu, K., Zhou, L., & Wei, H. (2023). Experimental study of thermal efficiency and NO_x emission of turbocharged direct injection hydrogen engine based on a high injection pressure. *International Journal of Hydrogen Energy*, 48(34), 12905-12916.
doi:<https://doi.org/10.1016/j.ijhydene.2022.12.031>
- [30] Rottengruber, H., Berckmüller, M., Elsässer, G., Brehm, N., & Schwarz, C. (2004). Direct-injection hydrogen SI-engine-operation strategy and power density potentials. *SAE transactions*, 1749-1761.

Article copyright: © 2024 Honglin Ma. This is an open access article distributed under the terms of the [Creative Commons Attribution 4.0 International License](https://creativecommons.org/licenses/by/4.0/), which permits unrestricted use and distribution provided the original author and source are credited.



Effect of Compression Ratio on the Performance of Direct-Injection Hydrogen Engines

Xu Zhe*

North China University of Water Resources and Electric Power, Zhengzhou City, No. 36, Beihuan Road, Henan, China

Received July 9, 2024; Accepted August 16, 2024; Published August 26, 2024

Direct injection of hydrogen into the cylinder can avoid abnormal combustion such as backfire, and the hydrogen engine can operate in a wider range of excess air coefficient. However, direct injection hydrogen engines still have problems such as high NO_x emissions under high load conditions, reduced power output due to lean combustion, and low thermal efficiency. This paper adopts a variable compression ratio structural design to study the impact of compression ratio changes on the comprehensive performance of direct injection hydrogen engines. The results show that under the same working conditions, as the engine compression ratio increases, the turbulence in the engine cylinder becomes more intense, increasing the back pressure in the cylinder, inhibiting the diffusion of hydrogen, making the hydrogen distribution more concentrated and the combustion conditions in the cylinder better. The overall performance of the engine is significantly improved.

Keywords: Direct injection; Compression ratio; Hydrogen; Indicated power; Indicated thermal efficiency; Turbulent kinetic energy

Introduction

With the development of automobile engines, the demand for new alternative fuels continues to increase. This trend has promoted the continuous innovation and development of energy technology. The emergence of new alternative fuels not only brings new development opportunities to the automotive industry, but also puts forward higher requirements for the energy industry, environmental protection and sustainable development. The promotion and application of alternative fuels has a positive contribution to the realization of environmental protection and emission reduction goals. The combustion of traditional fuels produces a large amount of greenhouse gases and harmful emissions, which have serious impacts on the atmospheric environment and human health. The application of new alternative fuels often has lower emission levels, which can reduce the emission of air pollutants, improve air quality and protect the ecological environment. In particular, some zero-emission alternative fuels, such as hydrogen fuel and electric vehicles, provide important support for achieving carbon neutrality and responding to climate change [1-3]. Hydrogen is considered a zero-carbon emission fuel with a very low production cost. It can be synthesized through a variety of chemical reactions such as ammonia decomposition, water gas, and water electrolysis. Hydrogen is known as the most promising alternative engine fuel at present, with the characteristics of clean combustion and no pollution. However, when used as a fuel in

*Corresponding author: xz15690863667@163.com

automobile engines, if hydrogen is not properly controlled, abnormal combustion is likely to occur. Common abnormal combustion in hydrogen engines [4-7] includes pre-ignition, backfire, detonation, etc.

As a renewable energy source, hydrogen energy can effectively reduce the emission of harmful substances from automobiles by utilizing its characteristics, providing a better solution to the contradiction between current environmental pollution and automobile emissions [8-9]. Currently, the application of hydrogen in the engine field mainly includes two modes [10-17]: One is to use it as a single fuel to directly drive the engine; the other is to mix it with traditional fuels such as gasoline and natural gas. However, due to the physical properties of hydrogen itself, the density of hydrogen is relatively small. When injecting hydrogen into the intake inlet method is adopted, the hydrogen expands immediately after being sprayed into the intake port, and quickly fills the entire intake port, which has a certain hindering effect on the entry of air. In severe cases, it will cause air to be unable to enter, the filling coefficient is low, and the incomplete combustion of fuel also brings about the negative effects of increased emissions and reduced engine power. In-cylinder direct injection technology solves the problem of hydrogen taking up cylinder volume and enhances the power performance of hydrogen internal combustion engines. Compared with intake inlet injection, direct-injection hydrogen combustion engines are able to inject after the intake valve is closed, effectively preventing backfire caused by hydrogen flowing back into the intake port. Under similar operating conditions, direct-injection hydrogen internal combustion engines can use a leaner combustion method to reduce pumping losses, thereby improving engine thermal efficiency.

Park *et al.* [18-19] investigated the engine performance and emission characteristics of hydrogen-natural gas blended fuels. The results show that when the excess air coefficient is constant, the thermal efficiency decreases with the increase of CO content; the increase of the heat capacity of the mixture reduces the combustion temperature, thereby inhibiting the formation of NO_x. Shivaprasad *et al.* [20] conducted tests on the performance and emission characteristics of a high-speed single-cylinder engine by selecting hydrogen-gasoline mixtures with different hydrogen enrichment levels, and studied the effects of hydrogen addition on the engine's brake mean effective pressure (Bmep), brake thermal efficiency, volumetric efficiency and emission characteristics. The results showed that hydrogen enrichment improved combustion performance, fuel consumption and Bmep. The experimental results also showed that the brake thermal efficiency was higher than that of pure gasoline conditions.. Both HC and CO emissions were reduced after hydrogen enrichment. Sukumaran & Kong [21] numerically simulated the direct in-cylinder hydrogen injection and the formation of the in-cylinder mixture. Early injection can produce a more uniform mixture during ignition. It is more advantageous to place the injector near the intake valve to take advantage of the interaction between the hydrogen jet and the intake flow to produce a more homogeneous mixture

This study adopts a higher compression ratio to improve thermal efficiency. However, as higher compression ratios are applied, NO_x emissions also increase. The traditional method to improve thermal efficiency and reduce NO_x is to burn a lean mixture of fuel and air. Currently, this is done by injecting hydrogen at the beginning of the compression stroke to form a mixture of hydrogen and air. In this paper, the thermal efficiency of a hydrogen internal combustion engine is improved by using at different compression ratios. It also further explores the effect of compression ratio on the thermal

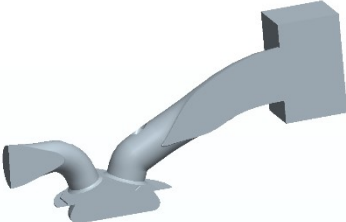
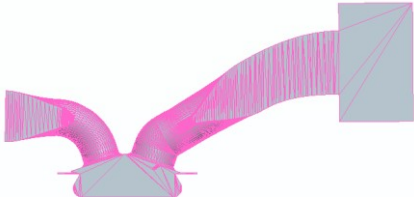

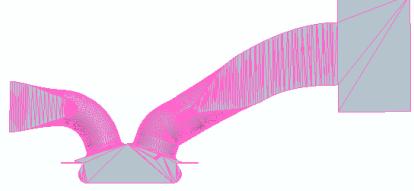
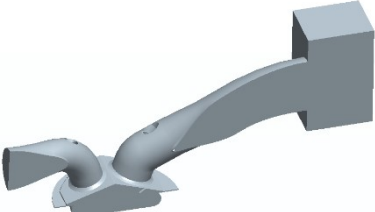
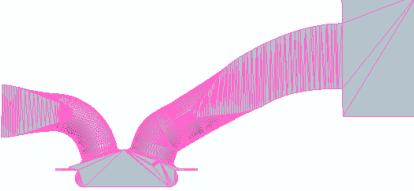
efficiency of the hydrogen engine at the same rotational speed, and analyzes the effects of different compression ratios on the in-cylinder mixture, emissions and performance of internal combustion engines.

Computational Models and Research Programs

This study uses a single-cylinder gasoline direct injection (GDI) test engine as a prototype, and further modifies the design based on the original size data of the prototype, converting it into a variable compression ratio in-cylinder direct injection hydrogen engine to meet the experimental requirements. The technical parameters of the experimental engine have been described in pervious publication [22].

Geometric and Mesh Models

In this experiment, based on the designed variable compression ratio engine combustion structure and the actual engine specifications, four groups of experimental engine models with different compression ratios were established using the 3D modeling software Creo. The four groups of models with different compression ratios were exported in stl format to obtain a preliminary mesh model. The specific model is shown in Figure 1.

Compression ratio	Engine Geometry Model	Initial mesh model of the engine
10:1		
12:1		
15:1		

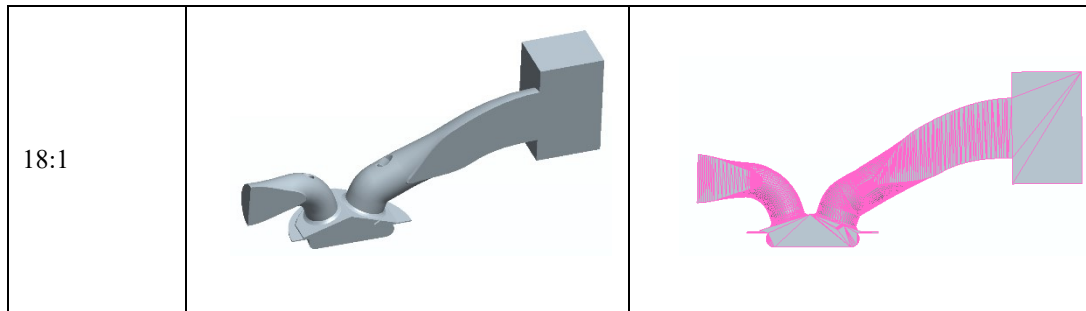


Fig. 1. Engine geometric model and mesh under different compression ratios

Initial and Boundary Conditions

The boundary conditions mainly include inlet and outlet boundaries, wall boundaries, symmetry surface boundaries, etc., among which wall boundaries are divided into fixed walls and moving walls. Various boundaries are mainly divided into pressure type and temperature type, and the corresponding type can be set according to the actual process. For example, the air inlet and exhaust port are inlet and outlet boundaries, and the type is set to pressure boundary; the inlet and exhaust channels are fixed wall boundaries, and the inlet and exhaust valves are moving wall boundaries, and the type is set to constant temperature boundary, etc. Both initial and boundary conditions have been described in pervious publication [22].

Model Validation

When the JH600 engine was converted to a hydrogen internal combustion engine, the model was validated under normal combustion conditions. The engine specifications include a cylinder diameter of 94 millimeters, a stroke of 85 millimeters, and a compression ratio of 15:1. The validation data has been described in pervious publication [22].

Results

Effect of Compression Ratio on In-Cylinder Mixture Velocity Field under Different Operating Conditions

Figure 2 shows the in-cylinder velocity field at 667° CA, 680° CA, 698° CA, respectively, when the compression ratio is 10:1. The effect of compression ratio on the mixture of in-cylinder direct hydrogen injection engine is mainly concentrated in the rear part of the upward movement of the piston after the intake closes. After the high-speed hydrogen is sprayed onto the cylinder wall, part of it moves with the bottom of the piston, and part of it moves upward along the cylinder wall. At the same time, as the crankshaft rotates and the piston moves upward, part of the fuel in contact with the cylinder wall is impacted by the piston movement and forms a new vortex at the bottom of the cylinder. With the injection of hydrogen, the speed of the mixture in the cylinder is further increased, and the mixture flowing outward from the top of the combustion chamber is affected by the crowding effect. The turbulent motion of the mixture at the top of the combustion chamber is restricted, and the mixture flowing outward from the top of the piston and the mixture flowing outward from the top of the combustion chamber are more turbulent. The turbulent motion in the combustion chamber is generated by the piston combustion chamber structure. The vortex formed by the hydrogen jet after touching the

bottom of the piston further expands, which accelerates the velocity of the mixed gas at the bottom of the piston and gradually develops upward. At the end of the piston stroke, the turbulent flow from the bottom of the piston develops upward to the top surface of the combustion chamber, and then forms a head-on downward after contacting the top surface of the combustion chamber. In this way, the velocity of the mixed gas at the bottom of the spark plug is at a larger position, which is beneficial to the flame propagation speed.

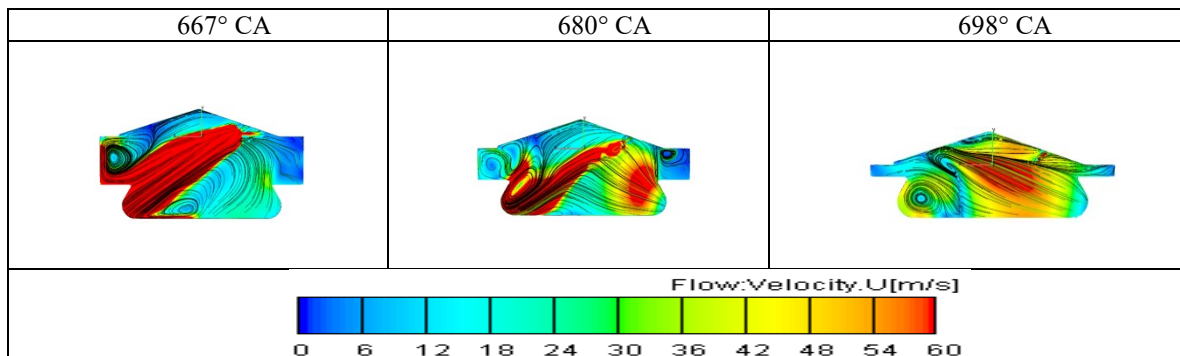


Fig. 2. In-cylinder mixture velocity field distribution at the compression ratio of 10:1

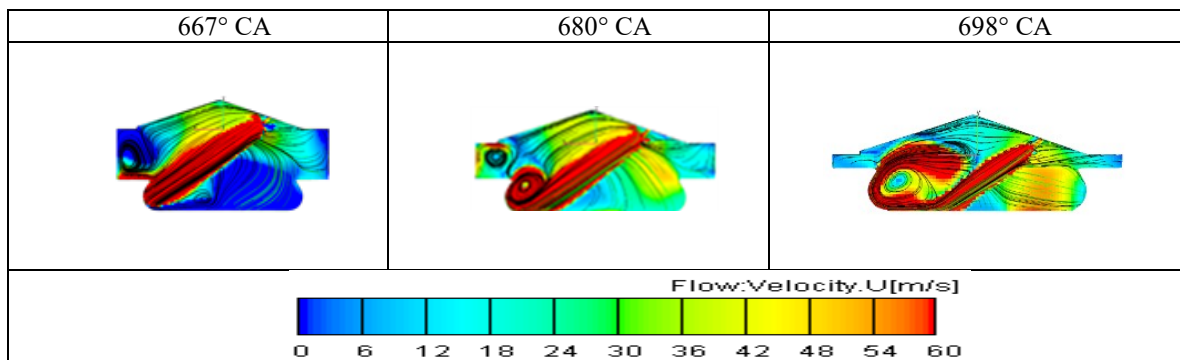


Fig. 3. In-cylinder mixture velocity field distribution at the compression ratio of 12:1

Figure 3 shows the velocity field distribution of the mixture in the cylinder at three moments when the compression ratio is 12:1, 667° CA, 680° CA, and 698° CA, respectively. From the velocity cloud diagram of the mixture in the cylinder at each moment, it can be seen that the movement law of the mixture in the cylinder when the compression ratio is 12 is basically the same as the development trend when the compression ratio is 10. However, as the compression ratio is further increased, the depth of the combustion chamber on the top surface of the piston continues to decrease, and the corresponding combustion chamber volume also decreases accordingly. At the same time, the squeezing effect of the piston bottom and the combustion chamber wall is also strengthened, which also promotes the turbulent movement of the mixture in the cylinder. As it can be seen in the figure, the depth of the combustion chamber is reduced due to the increase in compression ratio before hydrogen injection. Hydrogen injection promotes the movement of air flow in the cylinder, forming a vortex on the left side of the cylinder. At the same time, with the movement of the piston and the squeezing effect of the cylinder head, the center of the vortex located on the outside gradually moves toward the center of the cylinder. After the hydrogen injection is completed, the center of the vortex gradually moves toward the center, and then moves closer to the center. Simultaneously, with the

movement of the piston and the squeezing effect of the cylinder head, the center of the side vortex gradually moves toward the center of the cylinder. After the hydrogen injection is completed, the velocity distribution of the mixed gas in the cylinder is uneven due to the influence of the side vortex.

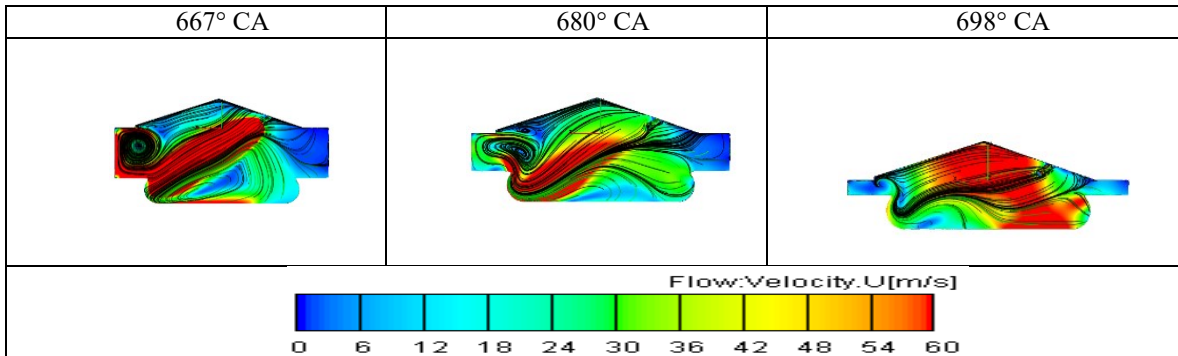


Fig. 4. In-cylinder mixture velocity field distribution at the compression ratio of 15:1

Figure 4 shows the velocity field and turbulence development trend of the mixture in the cylinder, when the compression ratio is 15:1. The increase in compression ratio further reduces the depth of the concave cavity on the top surface of the piston, and the volume of the combustion chamber also decreases accordingly. When the volume of the combustion chamber decreases, the movement of the mixture in the cylinder is enhanced under the impetus of the hydrogen jet, and the scope of influence is also expanded. After being squeezed by the cylinder wall, a new vortex is formed along the cylinder wall at the bottom of the cylinder. After encountering the hydrogen jet, the upper vortex moves along the center of the cylinder and promotes the movement of the hydrogen jet. On both sides of the hydrogen jet, after being squeezed by the cylinder wall, new vortices are formed along the cylinder wall. The vortex at the bottom of the cylinder moves along the center of the cylinder and drives the hydrogen jet to move. The upper vortex moves toward the middle of the cylinder under the enhancement of the circulation and finally forms a front, which enhances the flow rate of the mixture in the middle of the cylinder.

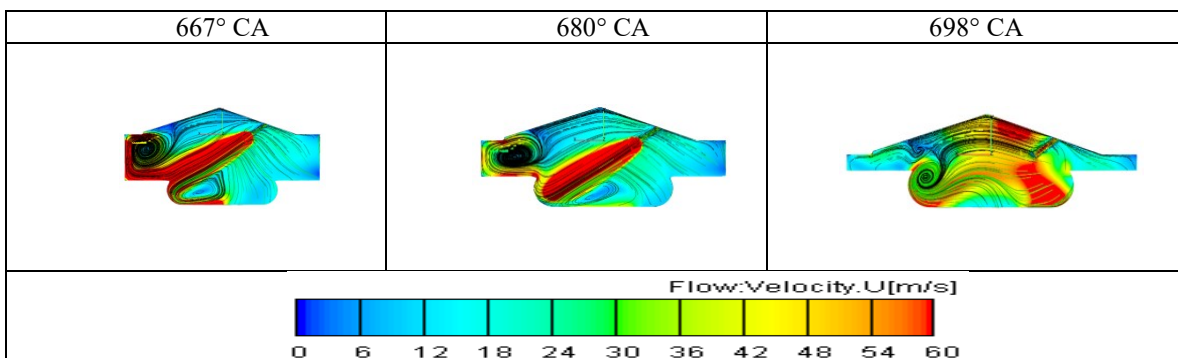


Fig. 5. In-cylinder mixture velocity field distribution at the compression ratio of 18:1

Figure 5 shows the velocity field distribution of the in-cylinder mixture at compression ratio of 18:1. The volume of the combustion chamber reaches its minimum with the increase of compression ratio. With the increase of compression ratio, the turbulence intensity of the mixture in the cylinder also increases continuously. At the same time, the range of influence of the hydrogen jet on the mixture in the cylinder also

expands with the increase of compression ratio. As shown in Figure 5, with the increase of compression ratio, the squeezing effect of the bottom of the piston takes effect later than the effect on the mixture in the cylinder at low compression ratio. The vortex effect at the bottom of the cylinder is weaker than the vortex at the top of the cylinder, and the large vortex at the top of the cylinder moves toward the center of the cylinder under the action of the cylinder wall, resulting in an overall increase in the velocity of the mixture in the cylinder. In addition, the increase in the flow rate of the hydrogen jet significantly enhances the turbulent motion inside the cylinder and accelerates the flow velocity of the mixture in the cylinder.

Effect of Compression Ratio on Turbulent Kinetic Energy of In-Cylinder Mixture and Mixture Distribution under Different Operating Conditions

According to the above analysis, it can be seen that the turbulent movement of the mixture in the cylinder will affect the combustion process of the engine. As the compression ratio increases, the turbulent movement in the cylinder becomes more active. From the change process of the velocity field in the cylinder with the crankshaft angle, it can be found that the part of the cylinder with higher gas flow velocity is mainly concentrated in the middle of the cylinder, which is beneficial to the propagation of the flame during the combustion process. In addition, the distribution of the mixture concentration field in the cylinder before combustion starts also has an important influence on the combustion and emission process of the engine. Reasonable mixture distribution is conducive to accelerating the combustion process and reducing emissions.

Turbulent kinetic energy refers to the flow kinetic energy generated by the mixing of fuel and air in the cylinder of a direct injection hydrogen engine due to different mixing degrees and the combustion of fuel during the combustion process [23-24]. The turbulent kinetic energy in the cylinder is an important indicator for evaluating the fuel energy conversion efficiency in the combustion chamber of a direct injection hydrogen engine and the fluidity of the fuel in the engine. Turbulence occurs throughout the entire process of the engine, especially in the mixing stage of the mixture in the cylinder. During the mixing stage of the mixture in the cylinder, the turbulent energy of the turbulent motion in the cylinder directly affects the quality of engine combustion and emissions, and also has an important impact on the engine's output power and the comprehensive utilization rate of fuel. Therefore, studying the turbulent energy of the mixture in the cylinder is of great significance to the comprehensive performance of the direct injection hydrogen engine. In hydrogen engines, due to the extremely high combustibility and diffusion rate of hydrogen fuel, the degree of mixture homogeneity and turbulence intensity play a decisive role in the combustion speed, combustion stability, combustion efficiency, and generation of harmful emissions.

Under different loads, the required amount of fuel is different, and the total amount of fuel required increases with the increase of load. Generally, the hydrogen injection mixing time at medium speed is longer than that at high speed. Therefore, this paper studies the changes in the state of the mixture in the cylinder when the compression ratio changes under different load conditions at 3000 r/min, hydrogen injection flow rate of 0.003 kg/h.

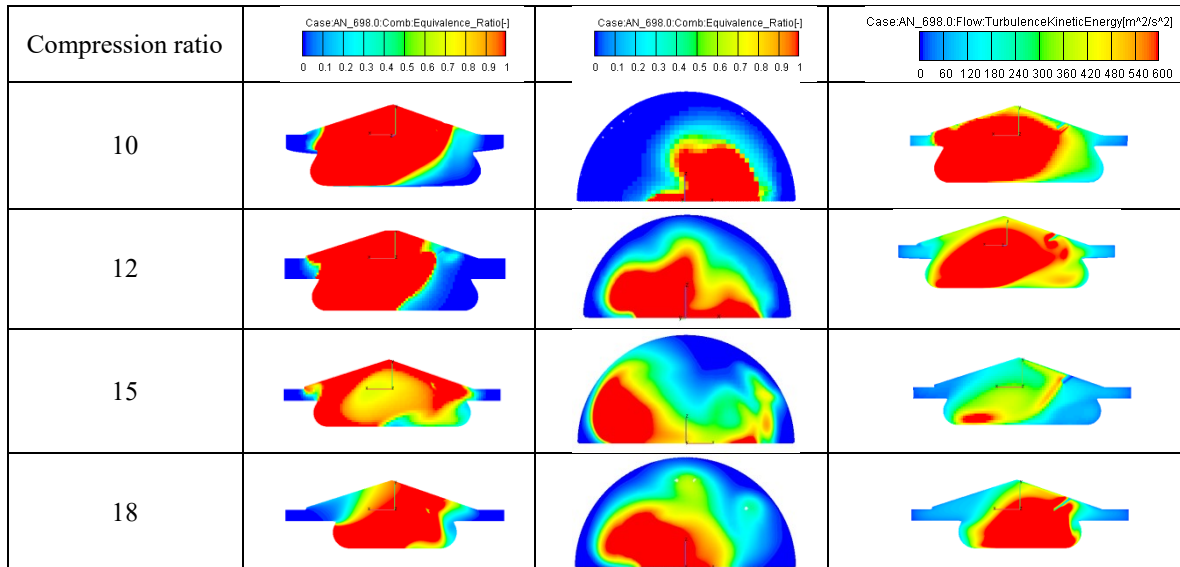


Fig. 6. Mixed gas concentration field and turbulent kinetic energy after hydrogen injection at 3000 rpm and 10% load

Figure 6 shows the concentration field of the mixture and the distribution of the mixture in the cylinder under different compression ratios at the end of the hydrogen injection period at 10% load and 3000 r/min. It can be seen from the figure that after the hydrogen injection stage, the hydrogen in the cylinder is mainly distributed in the left part of the cylinder. And the distribution of hydrogen in the cylinder is more concentrated, forming a fuel plume. The slice in the Y direction of the figure shows the distribution of hydrogen in the cylinder more three-dimensionally. The distribution of hydrogen is mainly concentrated in the center of the cylinder and moves to the right when the compression ratio is 10:1. However, as the compression ratio increases, the distribution of hydrogen in the cylinder gradually moves to the left. This is because when the piston rises during the hydrogen injection process, the hydrogen jet contacts the bowl-shaped structure at the bottom of the cylinder, and is squeezed by the piston and turbulently moves along the cylinder wall. The hydrogen moves to the right along the combustion chamber wall, then to the right, and then to the right. The combustion chamber wall moves to the right. At the end of hydrogen injection, the thicker part of the mixture in the cylinder is mainly distributed in the right part of the combustion chamber. However, with the increase of compression ratio, the depth of the combustion chamber gradually decreases. During the hydrogen injection process, the time when the hydrogen jet contacts the piston is delayed. Finally, at the end of continuous hydrogen injection, the main distribution of hydrogen in the cylinder moves to the left, and the hydrogen concentration in this area increases. According to the turbulent kinetic energy distribution diagram in the cylinder, it can be seen that the flow velocity and turbulent motion of the cylinder mixture in the hydrogen injection area are relatively concentrated after the hydrogen injection is completed. Therefore, the turbulent kinetic energy in the cylinder is relatively high at this time. However, as the compression ratio increases, the turbulent kinetic energy in the cylinder mixture concentration area is weakened by the turbulence in the cylinder.

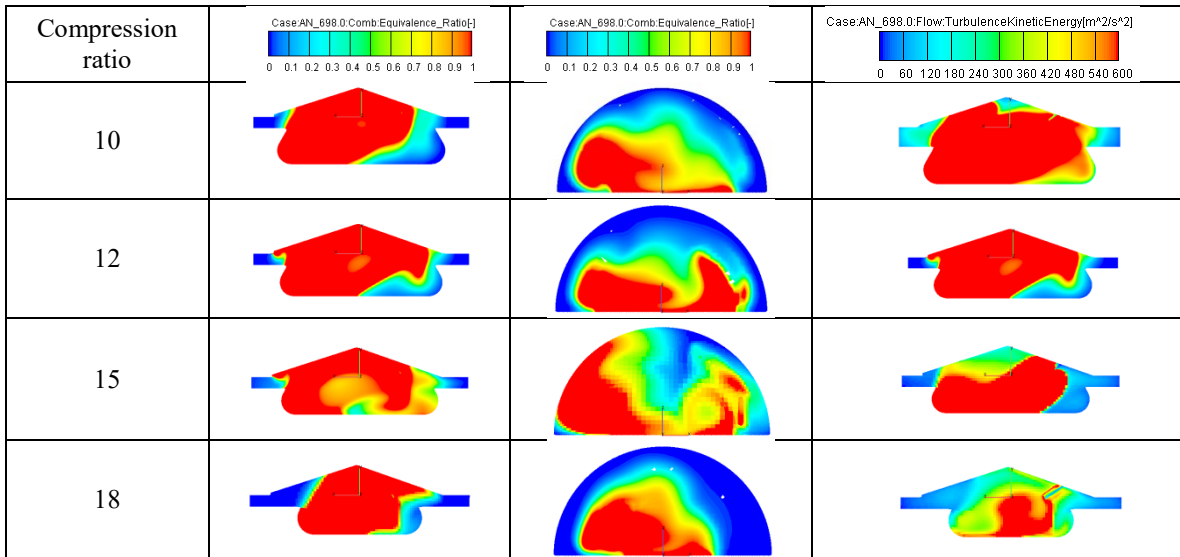


Fig. 7. Mixed gas concentration field and turbulent kinetic energy after hydrogen injection at 3000 rpm and 50% load

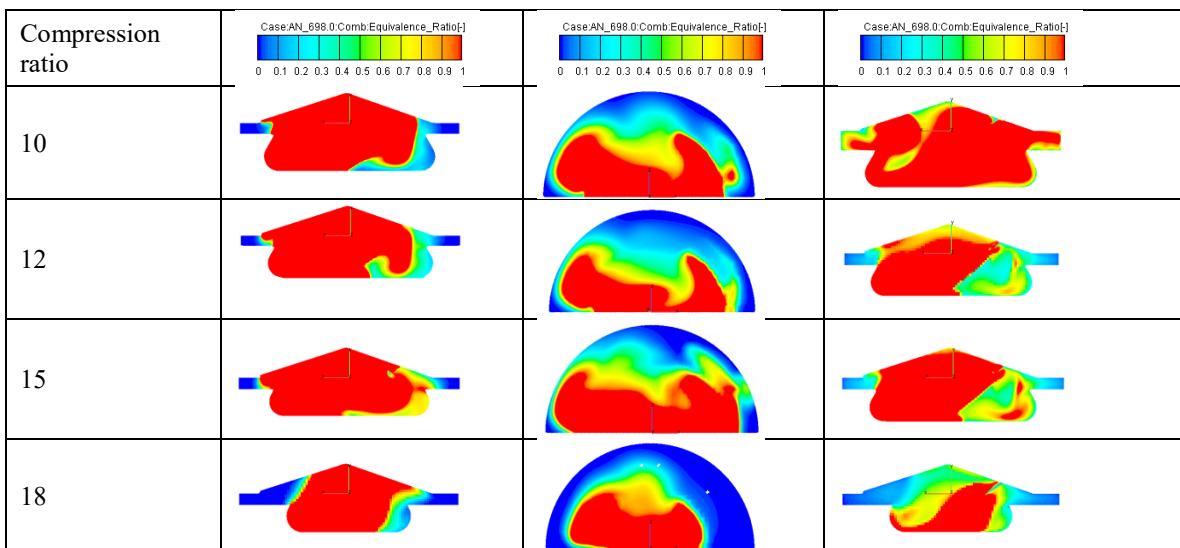


Fig. 8. Mixed gas concentration field and turbulent kinetic energy after hydrogen injection at 3000 rpm and 100% load

Figure 7 shows the distribution of the concentration field and turbulent kinetic energy of the mixture in the cylinder at 3000 r/min and 50% load. It can be seen from the in-cylinder concentration field and the Y-direction slice cloud diagram that when the load increases to 50%, the fuel required by the engine increases. In order to achieve the target equivalence ratio, more hydrogen needs to be injected. Therefore, compared with the area of the combustion chamber occupied by the fuel at low load, the distribution of the in-cylinder concentration field increases. As the area of the combustion chamber increases, the diffusion rate and diffusion range of hydrogen further increase, and an obvious concentration gradient appears. However, with the increase of the compression ratio, the diffusion rate of hydrogen is limited, causing the mixture to gather in the middle of the cylinder. The reason for this phenomenon is that with the increase of the compression ratio, when the piston runs near the top dead center, the back pressure in the combustion chamber at a high compression ratio is higher than the back pressure in the cylinder at a

low compression ratio, thereby further limiting the diffusion of fuel in the cylinder. At the same time, as the load increases, the turbulent kinetic energy intensity of the turbulent flow in the cylinder is also increasing. It can be seen that the turbulent intensity in the cylinder at a low compression ratio is significantly higher than that at a high compression ratio.

Figure 8 shows the distribution of concentration field and turbulent kinetic energy of the mixture in the cylinder at 3000 r/min and 100% load. It can be seen from the cloud diagram that with the further increase of load, the change patterns of the in-cylinder concentration field and turbulent kinetic energy are the same at 100% load and 50% load. However, compared with low load, the area occupied by the in-cylinder concentration field at high load further increases, but the concentration gradient distribution of hydrogen is smaller than at low load, and the diffusion range of hydrogen is further reduced.

Effect of Compression Ratio on Cylinder Pressure and Temperature of Direct-Injection Hydrogen Engine under Different Operating Conditions

This section takes 50% load as an example to show the variation trend of maximum cylinder pressure and temperature with compression ratio at different speeds. Figure 9 shows that under the same load and different speeds, the maximum pressure in the cylinder under each working condition increases with the increase of compression ratio. For example, at 4500 r/min and 0.0036 kg/h, the compression ratio increases from 10 to 18, and the maximum pressure in the cylinder increases from 4.835MPa to 7.453MPa. This is because, under the same other conditions, with the increase of compression ratio, the volume of the combustion chamber gradually decreases before the piston reaches the top dead center of the cylinder. The increase of compression ratio under the same load leads to the increase of pressure and temperature in the cylinder, thereby accelerating the propagation speed of the combustion flame. In addition, with the increase of compression ratio, the vortex inside the cylinder becomes more intense, and the space for vortex in the cylinder continues to increase. At the same time, the squeezing effect between the bottom of the piston and the cylinder head becomes more obvious, and the enhancement of the vortex in the cylinder greatly enhances the combustible mixture. The enhancement of the cylinder eddy current greatly improves the probability of ignition of the combustible mixture molecules, thereby accelerating the reaction process and causing an increase in the maximum cylinder pressure in the cylinder.

Figure 9 also shows that as the engine speed increases, when the speed increases from 3000 r/min to 6000 r/min, the maximum in-cylinder pressure under different working conditions at each compression ratio increases to varying degrees. At low speeds, as the compression ratio increases, the rate of increase in the highest cylinder pressure also increases. The highest cylinder pressure is affected by the compression ratio at low speeds, and as the speed increases, the highest external pressure decreases while the highest internal pressure increases. As the rotational speed increases, the rate of increase in maximum pressure decreases, and the maximum pressure inside the cylinder is less affected by the compression ratio.

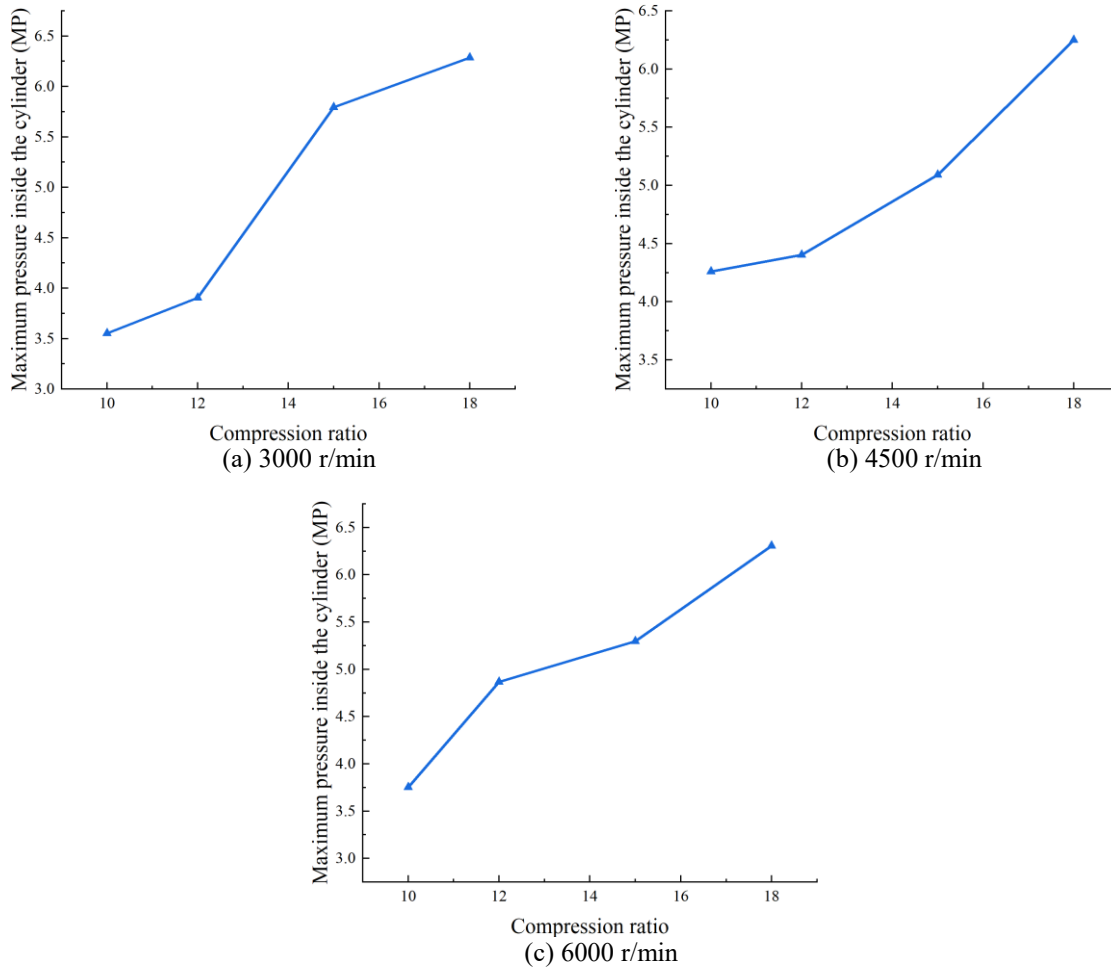


Fig. 9. The influence of the change of compression ratio at different speeds on the maximum pressure in the cylinder

As can be seen from Figure 10, under different working conditions of 50% load and different speeds, the maximum combustion temperature in the cylinder shows a positive correlation with the compression ratio, that is, as the compression ratio increases, the peak temperature that can be achieved in the cylinder rises synchronously. This shows that the increase in compression ratio improves the combustion quality of the mixture in the cylinder, speeds up the reaction speed of the mixture, and can increase the combustion heat in the cylinder, thereby increasing the maximum temperature in the cylinder. Figure 10a shows that at low speed and the same load, the maximum temperature in the cylinder is slightly higher than the peak temperature at high speed. This is because at low speed and the same load, the combustion duration of the mixture in the cylinder is longer and the heat release combustion is more complete. In addition, at low speed, the cylinder temperature of the mixture combustion is smaller than the combustion chamber structure, and the heat transfer loss is reduced, which increases the peak temperature in the cylinder. When the speed increases to 4500 r/min and 6000 r/min (Figures 10b,c), the peak temperature in the cylinder decreases. On the one hand, as the speed increases, the time of each cycle becomes shorter, and the heat transfer loss of the engine increases. On the other hand, as the speed increases, the combustion duration shortens, the combustion time of the mixture in the cylinder is relatively reduced, and the

mixture cannot release the heat in the cylinder in a timely and complete manner. But overall, the increase in compression ratio is beneficial to speeding up the combustion speed of the mixture in the cylinder, promoting combustion stability, and accelerating the heat release rate of the fuel.

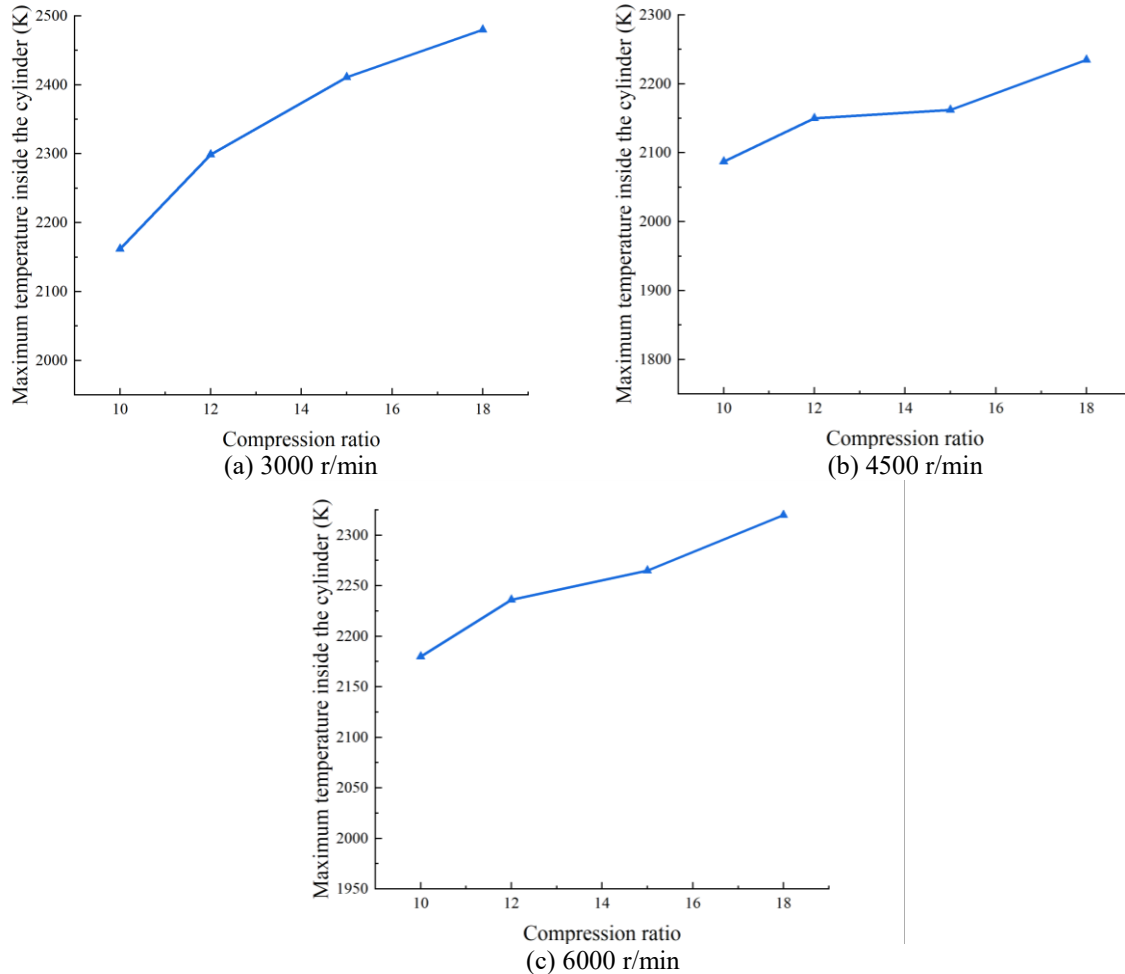


Fig. 10. The influence of the change of compression ratio on the maximum temperature in the cylinder at different speeds.

Effect of Compression Ratio on the Dynamics of Direct Injection Hydrogen Engines under Different Operating Conditions

As can be seen from Figure 11, taking 6000 r/min and 0.0041 kg/s as an example, when the compression ratio increases from 10:1 to 18:1, the indicated power of the engine increases from 26.4kW to 33.2kW. And at 50% load, the maximum indicated power at different speeds increases with the increase of rotational speed. This is because under the same conditions, as the compression ratio increases, the higher the compression ratio, the smaller the combustion chamber volume. Before the piston moves to the upper end point, the turbulent motion of the working material in the combustion chamber in the cylinder becomes more intense, which can be improved, effectively shortening the flame development period and accelerating the spread of the flame. At the same time, the increase in compression ratio reduces the combustion chamber volume, increases the

back pressure in the cylinder, and can inhibit the diffusion of the mixture, thereby increasing the indicated power of the engine.

By analyzing the effect of compression ratio on engine indicated power under different working conditions, it can be seen that the trend of indicated power of hydrogen engine under various working conditions is roughly the same as that of the highest pressure in the cylinder. The change of combustion pressure in the cylinder can indicate the ability of the fuel to convert chemical energy into heat energy and then into mechanical energy for external output, while the corresponding relationship between pressure in the cylinder and power ensures the accuracy of factor analysis. Under the same conditions, increasing the compression ratio can significantly improve the power loss of hydrogen engines caused by lean combustion. Therefore, by increasing the compression ratio, the overall indicated power of the engine can be significantly improved.

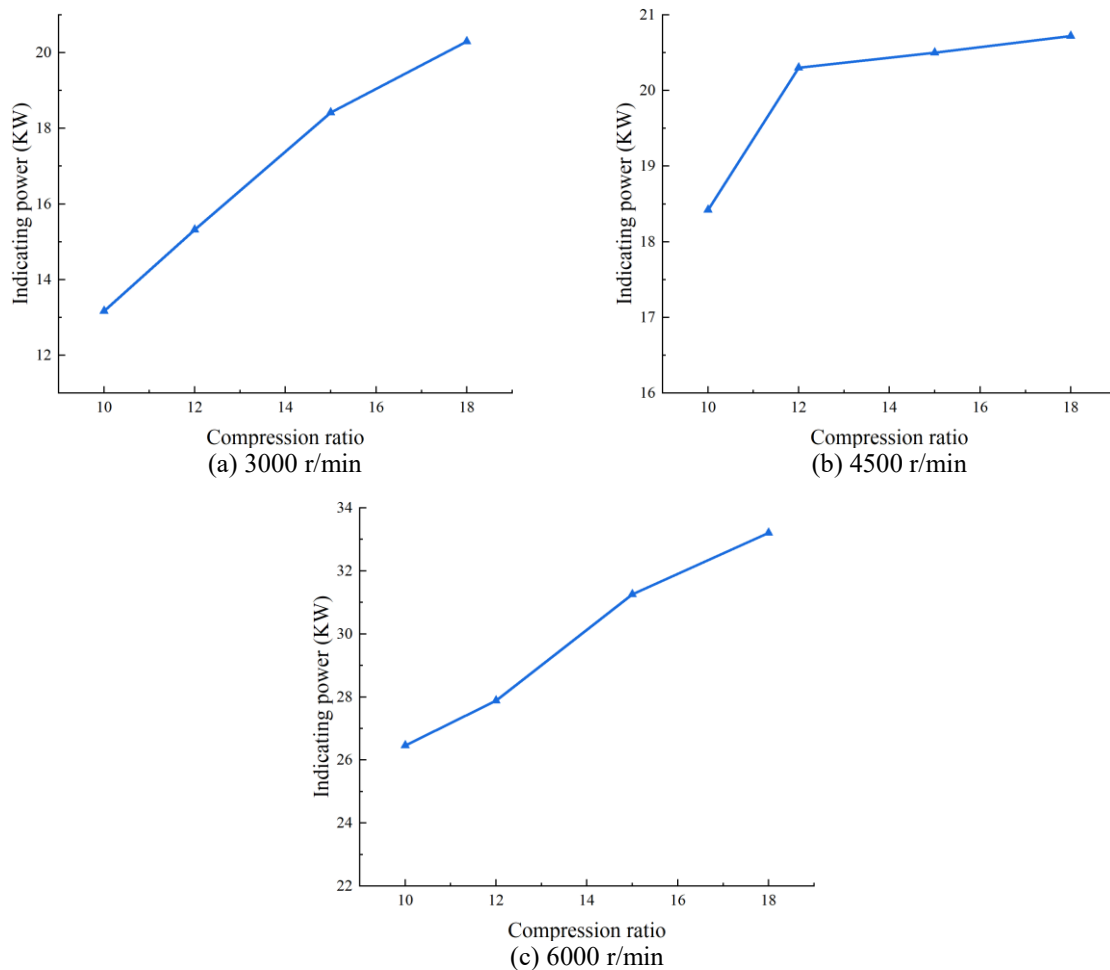


Fig. 11. The influence of compression ratio on the indicated power under different working conditions.

Effect of Compression Ratio on the Economy of Direct Injection Hydrogen Engines under Different Operating Conditions

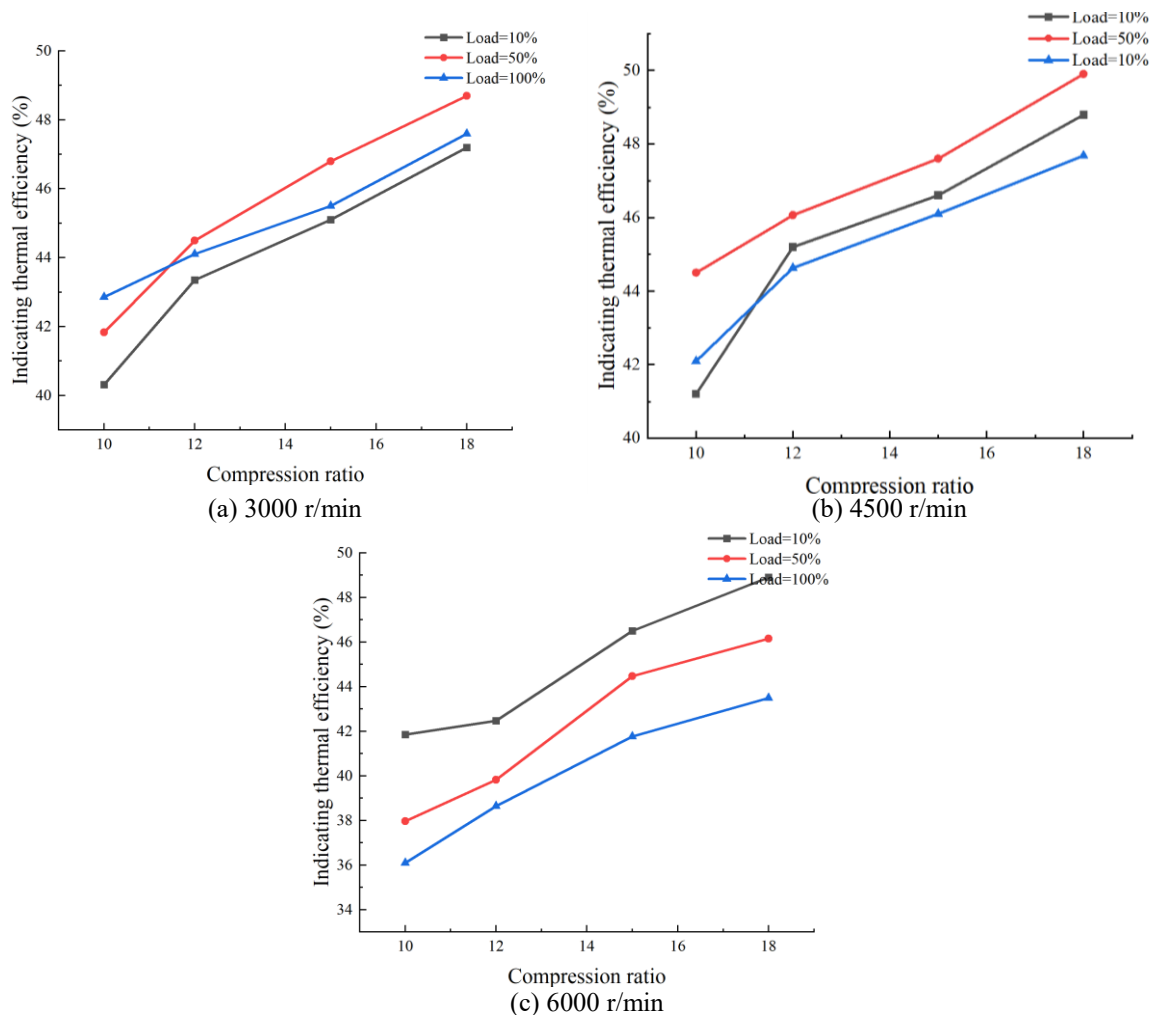


Fig. 12. The effect of compression ratio on indicated thermal efficiency of hydrogen engine under different working loads

Figure 12 shows the changing trend of indicated thermal efficiency with the increase of compression ratio at 3000 r/min, 4500 r/min, and 6000 r/min under some working conditions. This section mainly examines the influence of the single compression ratio factor on the indicated thermal efficiency of the hydrogen engine. Therefore, the compression ratios at 3000 r/min, 4500 r/min, and 6000 r/min are selected to study the influence of compression ratio on the indicated thermal efficiency at different speeds and loads. It can be seen that with the increase of compression ratio, the indicated thermal efficiency of hydrogen engine under different loads also gradually increases, and the economy of the engine gradually improves. This is because under the same conditions, the compression ratio increases, the combustion chamber volume decreases, and the pressure in the cylinder increases during the upward movement of the piston. The increase in cylinder pressure reduces the diffusion degree of the hydrogen jet, forming a high-quality mixture with local enrichment of hydrogen. At the same time, the increase in compression ratio also increases the temperature of the combustion chamber, accelerates the combustion reaction, shortens the combustion duration, and makes the hydrogen

combustion more sufficient and complete. Taking 3000 r/min and 50% load as an example, as the compression ratio increases, the best indicated thermal efficiency of the hydrogen engine increases from 41.8% to 48.7%. This shows that increasing the compression ratio is one of the important ways to improve the indicated thermal efficiency of the engine.

From Figure 12, the best indicated thermal efficiency obtained at 50% load, a compression ratio of 18, and 3000 r/min, 4500 r/min and 6000 r/min are 48.7%, 49.5% and 48.7%, respectively. The indicated thermal efficiency at 3000 r/min and 4500 r/min 50% load conditions is significantly higher than that at other conditions. In addition, as the speed increases, the indicated thermal efficiency at 6000 r/min 10% load condition is the best. This is because increasing the target equivalence ratio of load-corresponding combustion increases the pressure and temperature of the combustion process, thereby improving the overall indicated thermal efficiency. However, with the increase in speed and load, the maximum temperature of the in-cylinder reaction in the high load conditions greatly increased, increasing the heat transfer loss of the cylinder wall and other walls. In addition, a fixed ignition timing was used during the experimental simulation, and the turbulent motion in the cylinder was more intense under high-speed and high-load conditions, which accelerated the flame propagation speed and increased the actual compression negative work of the engine. This reduces the indicated thermal efficiency of the hydrogen engine under high load conditions.

Conclusions

(1) With the increase of compression ratio, during the upward movement of the piston, the in-cylinder mixture is enhanced by the squeezing effect of the bottom surface of the piston and the cylinder wall, which promotes the turbulence movement of the in-cylinder mixture and the expansion of the in-cylinder vortex distribution range. In addition, with the continuous increase of the hydrogen injection flow rate, it increases the initial velocity of the hydrogen jet, which accelerates the in-cylinder mixture flow rate and enhances the enhancement of the in-cylinder vortex.

(2) As the compression ratio increases, the main distribution center of hydrogen in the cylinder gradually moves toward the center. When the compression ratio is 18:1, the hydrogen concentration in the middle of the cylinder is higher, and obvious stratification occurs at low load. This is because the increase in compression ratio is affected by the crowded flow on the cylinder wall and the vortex in the cylinder, causing the main distribution of hydrogen in the cylinder to move toward the center of the cylinder. Due to the increase in compression ratio, the background pressure in the cylinder increases, which inhibits the diffusion of hydrogen and causes more hydrogen to diffuse toward the center of the cylinder. As the load increases, the cylinder area occupied by hydrogen fuel gradually increases, and obvious stratification occurs at low loads. The hydrogen concentration gradient decreases under medium and high load conditions.

(3) The increase of compression ratio under different working conditions has a significant effect on the maximum pressure and temperature in the cylinder. On the one hand, the increase of compression ratio enhances the turbulence movement in the cylinder, optimizes the distribution of hydrogen in the cylinder and increases the chance of ignition of the combustible mixture. On the other hand, it helps accelerate the

combustion speed of the mixture in the cylinder, promotes the stability of the combustion, and accelerates the heat release rate of the fuel.

CONFLICTS OF INTEREST

The author declares that there is no conflict of interests regarding the publication of this paper.

REFERENCES

- [1] Luo, Y., Wu, B., Li, Q., Tang, X., Yang, Z., Wu, C., & Wu, T. (2024). Experimental and simulation research on the lean combustion characteristics of direct-injection hydrogen engine. *International Journal of Hydrogen Energy*, 68, 398-409. doi:<https://doi.org/10.1016/j.ijhydene.2024.04.184>
- [2] Huang, Z., Yuan, S., Wei, H., Zhong, L., Hu, Z., Liu, Z., . . . Zhou, L. (2024). Effects of hydrogen injection timing and injection pressure on mixture formation and combustion characteristics of a hydrogen direct injection engine. *Fuel*, 363, 130966. doi:<https://doi.org/10.1016/j.fuel.2024.130966>
- [3] Duan, Y.-h., Sun, B.-g., Li, Q., Wu, X.-s., Hu, T.-g., & Luo, Q.-h. (2023). Combustion characteristics of a turbocharged direct-injection hydrogen engine. *Energy Conversion and Management*, 291, 117267. doi:<https://doi.org/10.1016/j.enconman.2023.117267>
- [4] Fu, Z., Li, Y., Wu, W., Li, Y., & Gao, W. (2024). Experimental study on the combustion and emission performance of the hydrogen direct injection engine. *International Journal of Hydrogen Energy*, 61, 1047-1059. doi:<https://doi.org/10.1016/j.ijhydene.2024.02.276>
- [5] Azeem, N., Beatrice, C., Vassallo, A., Pesce, F., Gessaroli, D., Biet, C., & Guido, C. (2024). Experimental study of cycle-by-cycle variations in a spark ignition internal combustion engine fueled with hydrogen. *International Journal of Hydrogen Energy*, 60, 1224-1238. doi:<https://doi.org/10.1016/j.ijhydene.2024.02.182>
- [6] Shahpouri, S., Gordon, D., Hayduk, C., Rezaei, R., Koch, C. R., & Shahbakhti, M. (2023). Hybrid emission and combustion modeling of hydrogen fueled engines. *International Journal of Hydrogen Energy*, 48(62), 24037-24053. doi:<https://doi.org/10.1016/j.ijhydene.2023.03.153>
- [7] Zhang, K., Jin, Z., Liu, Q., & Liu, L. (2024). Novel Green Hydrogen – Fossil Fuel Dehydrogenation. *Fundamental Research*. doi:<https://doi.org/10.1016/j.fmre.2024.06.007>
- [8] Rosendal, M. B., Münster, M., & Bramstoft, R. (2024). Renewable fuel production and the impact of hydrogen infrastructure — A case study of the Nordics. *Energy*, 297, 131234. doi:<https://doi.org/10.1016/j.energy.2024.131234>
- [9] Singh, M., Singla, M. K., Beryozkina, S., Gupta, J., & Safaraliev, M. (2024). Hydrogen vehicles and hydrogen as a fuel for vehicles: A-State-of-the-Art review. *International Journal of Hydrogen Energy*, 64, 1001-1010. doi:<https://doi.org/10.1016/j.ijhydene.2024.03.325>

- [10] Abubakar, S., Muhamad Said, M. F., Abas, M. A., Ismail, N. A., Khalid, A. H., Roslan, M. F., & Kaisan, M. U. (2024). Hydrogen-fuelled internal combustion engines - Bibliometric analysis on research trends, hotspots, and challenges. *International Journal of Hydrogen Energy*, 61, 623-638. doi:<https://doi.org/10.1016/j.ijhydene.2024.02.280>
- [11] Yang, Z., Guo, P., Wang, L., & Hao, Q. (2024). Multi-objective optimization analysis of hydrogen internal combustion engine performance based on game theory. *Applied Energy*, 374, 123946. doi:<https://doi.org/10.1016/j.apenergy.2024.123946>
- [12] Sebastian, S., Wijewardane, S., & Srinivasan, S. (2023). Recent advances in hydrogen production, storage, and fuel cell Technologies with an emphasis on inventions, innovations, and commercialization. *Solar Compass*, 8, 100065. doi:<https://doi.org/10.1016/j.solcom.2023.100065>
- [13] Jafari, H., Safarzadeh, S., & Azad-Farsani, E. (2022). Effects of governmental policies on energy-efficiency improvement of hydrogen fuel cell cars: A game-theoretic approach. *Energy*, 254, 124394. doi:<https://doi.org/10.1016/j.energy.2022.124394>
- [14] Stockford, C., Brandon, N., Irvine, J., Mays, T., Metcalfe, I., Book, D., . . . Thompson, C. (2015). H2FC SUPERGEN: An overview of the Hydrogen and Fuel Cell research across the UK. *International Journal of Hydrogen Energy*, 40(15), 5534-5543. doi:<https://doi.org/10.1016/j.ijhydene.2015.01.180>
- [15] Richardson, I. A., Fisher, J. T., Frome, P. E., Smith, B. O., Guo, S., Chanda, S., . . . Leachman, J. W. (2015). Low-cost, transportable hydrogen fueling station for early market adoption of fuel cell electric vehicles. *International Journal of Hydrogen Energy*, 40(25), 8122-8127. doi:<https://doi.org/10.1016/j.ijhydene.2015.04.066>
- [16] Alazemi, J., & Andrews, J. (2015). Automotive hydrogen fuelling stations: An international review. *Renewable and Sustainable Energy Reviews*, 48, 483-499. doi:<https://doi.org/10.1016/j.rser.2015.03.085>
- [17] Sun, Z.-y., Liu, F.-S., Liu, X.-h., Sun, B.-g., & Sun, D.-W. (2012). Research and development of hydrogen fuelled engines in China. *International Journal of Hydrogen Energy*, 37(1), 664-681. doi:<https://doi.org/10.1016/j.ijhydene.2011.09.114>
- [18] Park, C., Kim, C., & Choi, Y. (2012). Power output characteristics of hydrogen-natural gas blend fuel engine at different compression ratios. *International Journal of Hydrogen Energy*, 37(10), 8681-8687. doi:<https://doi.org/10.1016/j.ijhydene.2012.02.052>
- [19] Park, C., Kim, C., Choi, Y., Won, S., & Moriyoshi, Y. (2011). The influences of hydrogen on the performance and emission characteristics of a heavy duty natural gas engine. *International Journal of Hydrogen Energy*, 36(5), 3739-3745. doi:<https://doi.org/10.1016/j.ijhydene.2010.12.021>
- [20] Shivaprasad, K. V., Raviteja, S., Chitragar, P., & Kumar, G. N. (2014). Experimental Investigation of the Effect of Hydrogen Addition on Combustion Performance and Emissions Characteristics of a Spark Ignition High Speed Gasoline Engine. *Procedia Technology*, 14, 141-148. doi:<https://doi.org/10.1016/j.protcy.2014.08.019>
- [21] Sukumaran, S., & Kong, S.-C. (2010). Numerical study on mixture formation characteristics in a direct-injection hydrogen engine. *International Journal of*

- Hydrogen Energy*, 35(15), 7991-8007.
doi:<https://doi.org/10.1016/j.ijhydene.2010.05.090>
- [22] Ma, H. (2024). Effect of hydrogen injection flow rate on the performance of in-cylinder direct injection hydrogen engines. *Trends in Renewable Energy*, 10(3), 266-282. doi:<http://dx.doi.org/10.17737/tre.2024.10.3.00177>
- [23] Wang, T., Wang, Y., Zhang, L., Zheng, Y., Liu, R., Wang, C., & Gong, W. (2024). Influence of In-Cylinder Turbulence Kinetic Energy on the Mixing Uniformity within Gaseous-Fuel Engines under Various Intake Pressure Conditions. *Energies*, 17(13), 3321. doi:<https://doi.org/10.3390/en17133321>
- [24] Fu, X. (2022). *Research on the interaction mechanism between turbulence and combustion in natural gas engine*. Jilin University, Thesis

Article copyright: © 2024 Zhe Xu. This is an open access article distributed under the terms of the [Creative Commons Attribution 4.0 International License](https://creativecommons.org/licenses/by/4.0/), which permits unrestricted use and distribution provided the original author and source are credited.



Virtual Topologies for Populating Overhead Low-Voltage Broadband over Powerlines Topology Classes by Exploiting Neural Network Topology Generator Methodology (NNTGM) - Part 1: Theory

Athanasios G. Lazaropoulos*

*School of Electrical and Computer Engineering / National Technical University of Athens /
9 Iroon Polytechniou Street / Zografou, GR 15780*

Received July 23, 2024; Accepted September 1, 2024; Published September 8, 2024

Based on a set of indicative overhead low voltage broadband over power lines (OV LV BPL) topologies of respective OV LV BPL topology classes, Neural Network Topology Generator Methodology (NNTGM) is theoretically proposed in this paper, so that its generated OV LV BPL topologies (NNTGM OV LV BPL topologies) can populate the OV LV BPL topology classes. Given the indicative topology of the OV LV BPL topology class, the NNTGM OV LV BPL topologies can be statistically familiar with the corresponding indicative OV LV BPL topology in terms of the theoretical channel attenuation behavior. Actually, NNTGM is based on the reverse procedure of the Neural Network Identification Methodology for the distribution line and branch Line Length Approximation (NNIM-LLA); say, NNTGM generates theoretical channel attenuation behaviors given the number of branches, the distribution line lengths and the branch line lengths, when appropriate NNTGM default operation settings are assumed. The statistical familiarity between the examined indicative OV LV BPL topology and an NNTGM OV LV BPL topology is examined after the application of appropriate channel attenuation metrics. On the basis of the channel attenuation metrics, class maps are theoretically defined so that the relative positions of indicative OV LV BPL topologies and their respective NNTGM OV LV BPL topologies (NNTGM virtual topologies) can be further studied.

Keywords: Smart Grid; Broadband over Power Lines (BPL) Networks; Power Line Communications (PLC); Distribution and Transmission Power Grids; Neural Networks; Simulation; Modeling

Introduction

Among the communications solutions that can be integrated across the smart grid in order to support its intelligent IP-based communications network of two-way information flows, Broadband over Power Lines (BPL) networks may exploit the available wired power grid infrastructure without investing additional costs in networking cables [1-7].

Deterministic Hybrid Model (DHM), which describes the BPL signal propagation and transmission across the topologies of the overhead low voltage (OV LV) BPL networks while feeding the Topology Identification Methodology (TIM) BPL topology database with the big data of the operation of OV LV BPL topologies, is considered to be

*Corresponding author: AGLazaropoulos@gmail.com

the channel model basis where all the artificial intelligence (AI), machine learning (ML) and neural network (NN) features have been built on [3, 4, 8-16]. As the added AI - ML - NN functionalities are concerned, the neural network identification methodology for the branch number identification (NNIM-BNI) of OV LV BPL topologies has been proposed in [17]. Then, the neural network identification methodology for the distribution line and branch line length approximation (NNIM-LLA) has been proposed for the OV LV BPL topologies in [2] while its performance has been assessed for various usage scenarios in [6, 7]. Actually, NNIM-LLA approximates the distribution line and branch line lengths for a given OV LV BPL topology theoretical channel attenuation behavior thus performing the tomography of the OV LV BPL topology.

In this paper, the Neural Network Topology Generator Methodology (NNTGM) is theoretically proposed and aims at reversing the operation of NNIM-LLA so that virtual topologies can populate existing OV LV BPL topology classes [18-21]. For the NNTGM operation, the available big data of the TIM BPL topology database for the OV LV BPL topologies of [15, 16], the NN architectures / training / methodology of [2, 17] and the conclusions for better approximation performances for the family products of TIM and NNIM of [2, 6, 7, 17] are exploited. The NNTGM output is a collection of NNTGM virtual topologies that present only theoretical channel attenuation behaviors when their topological characteristics are set to be derived from the topological characteristics of the indicative OV LV BPL topology of the examined class that anyway acts as the basis for the topological characteristics of the NNTGM virtual topologies. In accordance with [2, 6, 7, 17], since default operation settings play a critical role in the operation of the family products of TIM and NNIM, they are also going to determine the operation of NNTGM. However, the NNTGM default operation settings, which are going to be analytically reported in this paper, are different from the NNIM-based ones in terms of the preparation parameters of the TIM OV LV BPL topology database since the vicinity to the examined indicative OV LV BPL topology is of interest for NNTGM rather than the representativeness of all the OV LV BPL topologies.

To examine the statistical familiarity of the NNTGM virtual topologies with the respective indicative OV LV BPL topologies, channel attenuation metrics, such as the average theoretical channel attenuation (ACA) and the root mean square delay-spread (RMS-DS), are going to be exploited. With reference to [18-22], new OV LV BPL topology class maps are here defined by the graphical ACA / RMS-DS combination of their respective indicative OV LV BPL topologies. NNTGM virtual topologies that come from an indicative OV LV BPL topology graphically define the NNTGM virtual topology footprint of the indicative OV LV BPL topology. The graphical vicinity of the NNTGM virtual topology footprints to their respective indicative OV LV BPL topologies is examined on the OV LV BPL topology class maps. Then, the impact of the parameters of the NNTGM default operation settings on the relative position and the size of the NNTGM virtual topology footprints are further graphically and numerically assessed in the companion paper [23].

The rest of this paper is organized as follows: Section 2 briefly presents the indicative OV LV BPL topologies of the classes that are going to be used during the benchmark process of these two papers. Also, this Section summarizes the basics of DHM, TIM OV LV BPL topology database and NNIM-LLA as well as NNIM-LLA default operation settings. Section 3 analyzes the operation of the proposed NNTGM. Also, the NNTGM default operation settings and the channel attenuation metrics of ACA and RMS-DS are here reported. Section 4 concludes this paper.

Indicative OV LV BPL Topologies of Topology Classes, DHM, TIM OV LV BPL Topology Database and NNIM-LLA

In this Section, four indicative OV LV BPL topologies that are the representative ones of the four main OV LV BPL topology classes of [18-21, 24] are reported. Then, DHM, which creates the big data pool, and TIM OV LV BPL topology database are briefly discussed. Finally, NNIM-LLA, which is going to be procedurally reversed for the sake of the NNTGM definition, is presented as well as NNIM-LLA default operation settings.

OV LV BPL Topologies and Respective Topology Classes

As already mentioned in [8, 10, 25, 26], OV LV BPL networks are divided into cascaded OV LV BPL topologies of typical lengths of 1000m while a typical OV LV BPL topology is shown in Figure 1. With reference to Figure 1, the typical OV LV BPL topology is bounded by its transmitting and receiving ends. Across the transmission path of the OV LV BPL topology, N branches of open-circuit terminations may occur. The arbitrary $k, k=1, \dots, N$ branch has length equal to L_{bk} while it is located at distance $\sum_{i=1}^k L_i$ from the transmitting end. In accordance with [2, 10, 17, 25], the topological characteristics and the number of branches for four indicative OV LV BPL topologies – *i.e.*, Line-Of-Sight (LOS), rural, suburban and urban– are listed in Table 1. The aforementioned four indicative OV LV BPL topologies are the representative ones of the respective main OV LV BPL topology classes, which are detailed in [18, 20, 21].

DHM

DHM is a synthetic BPL channel model of three cascaded modules; say, the bottom-up, the top-down and the coupling scheme modules [2, 8-10, 17, 19, 25, 29, 30]. In detail, the bottom-up and top-down modules of DHM address the propagation and transmission issues of the BPL signal across the OV LV BPL topologies, respectively, while the coupling scheme module is responsible for studying the injection / extraction of the BPL signal across the OV LV Multi-conductor Transmission Line (MTL) configurations and the OV LV BPL topologies. The theoretical coupling scheme channel transfer function, which is the output of DHM for given OV LV MTL configuration, OV LV BPL topology and coupling scheme, is stored in the TIM OV LV BPL topology database. Trying different variations on the applied OV LV MTL configurations, OV LV BPL topologies and coupling schemes, TIM OV LV BPL topology database compiles a wealth of case studies thus creating the necessary big data for AI, ML and NNIM-based methodologies to operate.

TIM OV LV BPL Topology Database

In accordance with [2, 17], TIM OV LV BPL topology database has already acted as the big data pool for NNIM-BNI and NNIM-LLA. Depending on the operation scenario, the records of the TIM OV LV BPL topology database for NNIM-BNI and NNIM-LLA may contain the following fields: (i) the ID number p of the OV LV BPL topology when the number of all OV LV BPL topologies in the TIM OV LV BPL topology database is equal to P ; (ii) the actual number of branches N of the OV LV BPL topology; (iii) the actual lengths of the distribution lines $\mathbf{L} = [L_1 \ L_2 \ \dots \ L_{N+1}]$ of each

OV LV BPL topology;

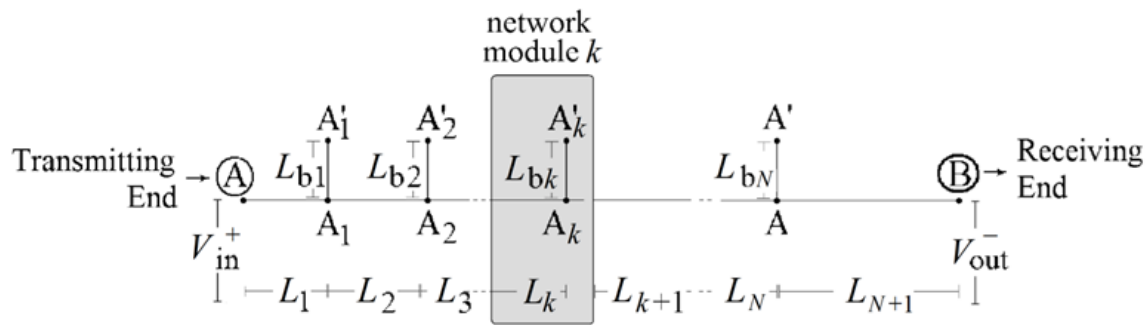


Fig. 1. Typical OV LV BPL topology with N branches [17, 27]

Table 1. Indicative OV LV BPL Topologies [10, 17, 18, 20, 21, 25, 28]

OV LV BPL Topology Name	OV LV BPL Topology Class Name	Branch Number (N)	Length of Main Lines	Length of Branches
Urban case A (Typical urban case)	Urban	3	$L_1=500\text{m}, L_2=200\text{m}, L_3=100\text{m}, L_4=200\text{m}$	$L_{b1}=8\text{m}, L_{b2}=13\text{m}, L_{b3}=10\text{m}$
Suburban case	Suburban	2	$L_1=500\text{m}, L_2=400\text{m}, L_3=100\text{m}$	$L_{b1}=50\text{m}, L_{b2}=10\text{m}$
Rural case	Rural	1	$L_1=600\text{m}, L_2=400\text{m}$	$L_{b1}=300\text{m}$
LOS case	LOS	0	$L_1=1000\text{m}$	-

(iv) the actual lengths of the branch lines $\mathbf{L}_b = [L_{b1} \ L_{b2} \ \dots \ L_{bN}]$ of each OV LV BPL topology; and (v) the theoretical coupling scheme channel transfer function values with respect to the frequency. Here, it should be noted that the size of the TIM OV LV BPL topology database, which further affects the performance and the execution times of the family products of NNIM-based methodologies, depends on the default operation settings that are applied and are presented in the following subsection.

NNIM-LLA and NNIM-LLA Default Operation Settings

NNIM-LLA has first been presented in [2] while its performance has been assessed during various operation scenarios in [6, 7]. NNIM-LLA is based on an NN architecture where its fully connected NN of HL hidden layers of neurons receives as input the amplitude of the coupling scheme channel transfer functions of the OV LV BPL topologies of the TIM OV LV BPL topology database in dB and gives as output the NNIM-LLA approximation for the lengths of the examined indicative OV LV BPL topology (*i.e.*, the NNIM-LLA approximation lengths of the distribution and branch lines are

$\mathbf{L}_{\text{NNIM-LLA}} = [L_{1,\text{NNIM-LLA}} \ L_{2,\text{NNIM-LLA}} \ \dots \ L_{N+1,\text{NNIM-LLA}}]$ and $\mathbf{L}_{b,\text{NNIM-LLA}} = [L_{b1,\text{NNIM-LLA}} \ L_{b2,\text{NNIM-LLA}} \ \dots \ L_{bN,\text{NNIM-LLA}}]$, respectively). Actually, NNIM-LLA approximates the distribution line and branch line lengths of the examined OV LV BPL topology when its OV LV BPL topology theoretical channel attenuation behavior is separately fed to NNIM-LLA. The core of NNIM-LLA is its MATLAB NN training program, which is detailed in [31, 32], that jointly processes the big data of the TIM OV LV BPL topology database with the OV LV BPL topology theoretical channel attenuation. The MATLAB NN training program is divided into three phases; say,

training, validation and testing phases, while these three phases segment the big data of the TIM OV LV BPL topology database in accordance with the respective participation percentages. In accordance with [2, 6, 7], the critical factor for the high performance and accuracy of NNIM-LLA is the selection of appropriate NNIM-LLA default operation settings.

According to [2, 6, 7, 17], the adoption of elaborate NNIM-LLA default operation settings, which may support higher accuracies for the TIM OV LV BPL topology database, can significantly improve the performance of NNIM-LLA. The NNIM-LLA operation settings that can be configured for the included OV LV BPL topologies in the TIM OV LV BPL topology database and for the operation of the MATLAB NN training program are: (i) the number of branches; (ii) the length spacings for the branch distance and the branch length; (iii) the branch line length range; (iv) the total distribution line length; (v) the coupling scheme; (vi) the frequency range; (vii) the flat-fading subchannel frequency spacing; and (viii) the default participation percentages of the three phases. However, a trade-off between the accuracy of the applied default operation settings and the total execution time of NNIM-LLA has been revealed in [6].

NNTGM is going to be the procedural reversal of NNIM-LLA while NNTGM default operation settings are going to exploit the NNIM-LLA ones and the good practices learned from their study. NNTGM is first presented in the coming Section.

NNTGM: Definition, Default Operation Settings, Channel Attenuation Metrics and Class Maps

In this Section, NNTGM is proposed based on the NNIM-based family products; say, NNIM-BNI and NNIM-LLA. Apart from its definition, NNTGM default operation settings are reported while their parameters that are going to be configured for the included OV LV BPL topologies in the TIM OV LV BPL topology database are discussed. Finally, the channel attenuation metrics of ACA and RMS-DS are mathematically defined so that they can be applied to the indicative OV LV BPL topologies and their respective NNTGM virtual OV LV BPL topologies for the preparation of the OV LV BPL topology class maps.

NNTGM Definition

With reference to Figure 2 of [2] and [17], NNTGM is going to implement the inverted NN architecture that has been applied in NNIM-BNI and NNIM-LLA. The structure of the NNTGM fully connected NN is assumed to have HL hidden layers of neurons. The input of the NN is P column vectors where P is the total number of the used OV LV BPL topologies that come from the records of the TIM OV LV BPL topology database while the p , $p=1, \dots, P$ column vector consists of the actual lengths of the distribution and branch lines of the arbitrary p OV LV BPL topology of the TIM OV LV BPL topology database, namely:

$$\mathbf{L}_{\text{TIM},p,hl=0}^{\text{OVLV,C}} \{ \cdot \} = [\mathbf{L}_p \quad \mathbf{L}_{b,p}]^T = [L_{1,p} \quad L_{2,p} \quad \dots \quad L_{N+1,p} \quad L_{b1,p} \quad L_{b2,p} \quad \dots \quad L_{bN,p}]^T \quad (1)$$

where $[\cdot]^T$ denotes the transpose of the matrix and each column vector consists of

$\underbrace{N+1}_{\text{number of main lines}} + \underbrace{N}_{\text{number of branches}} = 2N+1$ lines. After the input layer, HL hidden layers occur. The

output of the fully connected NN is a $Q \times 1$ channel attenuation difference column vector that is given by

$$\Delta \mathbf{H}^{\text{OVLV,C}\{\cdot\}} = [|H_{\text{NNTGM}}^{\text{OVLV,C}}(f_1)|_{\text{dB}} - |H_{\text{LOS}}^{\text{OVLV,C}}(f_1)|_{\text{dB}} \cdots \\ \cdots |H_{\text{NNTGM}}^{\text{OVLV,C}}(f_q)|_{\text{dB}} - |H_{\text{LOS}}^{\text{OVLV,C}}(f_q)|_{\text{dB}} \cdots |H_{\text{NNTGM}}^{\text{OVLV,C}}(f_Q)|_{\text{dB}} - |H_{\text{LOS}}^{\text{OVLV,C}}(f_Q)|_{\text{dB}}]^T \quad (2)$$

where $|H_{\text{NNTGM}}^{\text{OVLV,C}\{\cdot\}}|_{\text{dB}}$ is the amplitude of the coupling scheme channel transfer function of the NNTGM generated OV LV BPL topology in dB, $|H_{\text{LOS}}^{\text{OVLV,C}\{\cdot\}}|_{\text{dB}}$ is the amplitude of the coupling scheme channel transfer function of LOS case of Table 1 in dB, $[\cdot]^C$ denotes the applied coupling scheme and $f_q, q = 1, \dots, Q$ are the operating frequencies when the examined frequency range is divided into Q flat-fading subchannels. With reference to eq. (2), the output of the NNTGM is the $Q \times 1$ NNTGM generated channel attenuation column vector that is given by

$$\mathbf{H}_{\text{NNTGM}}^{\text{OVLV,C}\{\cdot\}} = \Delta \mathbf{H}^{\text{OVLV,C}\{\cdot\}} + \\ + [|H_{\text{LOS}}^{\text{OVLV,C}}(f_1)|_{\text{dB}} \cdots |H_{\text{LOS}}^{\text{OVLV,C}}(f_q)|_{\text{dB}} \cdots |H_{\text{LOS}}^{\text{OVLV,C}}(f_Q)|_{\text{dB}}]^T \quad (3)$$

As the operation of the NNTGM fully connected NN is concerned, NNTGM is based on the MATLAB NN training program of [31, 32] where the inner big data handling of the TIM OV LV BPL topology database is divided into training, validation and testing phases with respective participation percentages. In fact, the MATLAB NN training program randomly splits the supplied big data from the TIM OV LV BPL topology database into 3 portions in accordance with the aforementioned participation percentages of the three phases. In addition, training is achieved using the Levenberg-Marquardt algorithm while RMS-DS is the applied criterion for deciding the best NN approximation of the MATLAB NN training program.

To generate NNTGM virtual topologies for given indicative OV LV BPL topology, the option of testing additional external data that may be offered to the MATLAB NN training program is exploited while appropriately defining the insertions of the TIM OV LV BPL topology database. In contrast with the preparation of the TIM OV LV BPL topology database for NNIM-BNI and NNIM-LLA, TIM OV LV BPL topology database for NNTGM should contain only OV LV BPL topologies with the lengths of the distribution and branch lines that remain close to the respective values of the examined indicative OV LV BPL topology since NNTGM virtual topologies are expected to present only theoretical channel attenuation behaviors when their topological characteristics are assumed to be the same with the topological characteristics of the indicative OV LV BPL topology of the examined class. Hence, with reference to eq. (2), the actual lengths of the distribution and branch lines of the arbitrary p OV LV BPL topology during the preparation of the TIM OV LV BPL topology database for NNTGM are bounded as follows:

$$L_{i,p} - L_s \cdot t_s \leq L_{i,p} \leq L_{i,p} + L_s \cdot t_s, \quad L_{i,p} - L_s \cdot t_s \geq 0, \quad i=1, \dots, N \quad (4)$$

$$L_{i,p} \in \{L_{i,p} \pm L_s \cdot t | t \in \{0, \dots, t_s\}, t \in \mathbb{Z}^{0+}\}, \quad i=1, \dots, N \quad (5)$$

$$L_{N+1,p} = 1,000m - \sum_{i=1}^N L_{i,p} \quad (6)$$

$$L_{bi,p} - L_{bs} \cdot t_{bs} \leq L_{bi,p} \leq L_{bi,p} + L_{bs} \cdot t_{bs}, \quad L_{bi,p} - L_{bs} \cdot t_{bs} \geq 0, \quad i=1, \dots, N \quad (7)$$

$$L_{bi,p} \in \{L_{bi,p} \pm L_{bs} \cdot t | t \in \{0, \dots, t_{bs}\}, t \in \mathbb{Z}^{0+}\}, \quad i=1, \dots, N \quad (8)$$

where L_s and L_{bs} are the length of the distribution and branch line segments, respectively, and t_s and t_{bs} are the number of the distribution and branch line segments that are going to be used during the preparation of the TIM OV LV BPL topology database for NNTGM operation, respectively. From eqs. (4)-(8), given $L_s \cdot t_s$ and $L_{bs} \cdot t_{bs}$ remain

relatively small, the following observations concerning the preparation of the TIM OV LV BPL topology database are given:

- The total number of the OV LV BPL topologies that are going to be added in the TIM OV LV BPL topology database is equal to:

$$P = \underbrace{(2 \cdot t_s + 1)^N}_{\text{eqs.(4)-(6)}} \cdot \underbrace{(2 \cdot t_{bs} + 1)^N}_{\text{eqs.(7),(8)}} \quad (9)$$

when the examined indicative OV LV BPL topology is included into the TIM OV LV BPL topology database during the NNTGM operation. Conversely, when the examined indicative OV LV BPL topology is omitted from the TIM OV LV BPL topology database during the NNTGM operation, the total number of the OV LV BPL topologies from the TIM OV LV BPL topology database becomes equal to:

$$P = \underbrace{(2 \cdot t_s)^N}_{\text{eqs.(4)-(6)}} \cdot \underbrace{(2 \cdot t_{bs})^N}_{\text{eqs.(7),(8)}} \quad (10)$$

It is evident that the inclusion or not of the examined indicative OV LV BPL topology in the TIM OV LV BPL topology database may affect the degree of variation of the amplitude of the coupling scheme channel transfer function of the NNTGM generated OV LV BPL topologies in dB with respect to the amplitude of the coupling scheme channel transfer function of LOS case. The impact assessment of the inclusion or not of the examined indicative OV LV BPL topology in the TIM OV LV BPL topology database on the NNTGM performance is going to be numerically evaluated in the companion paper of [23].

- Apart from the total number of the OV LV BPL topologies that is going to be contained in the TIM OV LV BPL topology database for the NNTGM operation purposes as given in eqs. (9) and (10), the length and the number of distribution and branch line segments may further affect the degree of variation of the amplitude of the coupling scheme channel transfer function of the NNTGM generated OV LV BPL topologies in dB with respect to the amplitude of the coupling scheme channel transfer function of LOS case. Higher lengths and numbers of distribution and branch line segments entail higher variations of the amplitude of the coupling scheme channel transfer function of the NNTGM virtual OV LV BPL topologies due to the variety of the channel attenuation behaviors of the OV LV BPL topologies that are contained in the TIM OV LV BPL topology database. The assessment of the NNTGM virtual OV LV BPL topologies can be done by applying channel attenuation metrics such as the ACA and RMS-DS. Anyway, the lengths and numbers of distribution and branch line segments remain an essential part of the NNTGM default operation settings as theoretically shown in eqs. (4)-(8).
- The graphical vicinity of the NNTGM virtual topologies with their respective indicative OV LV BPL topologies is examined on the OV LV BPL topology class maps. The OV LV BPL topology class maps of this pair of papers are going to be plotted with reference to ACA and RMS-DS while the indicative OV LV BPL topologies of Table 1 will define their respective class map footprint center. Given the TIM OV LV BPL topology database and the examined indicative OV LV BPL topology, the respective NNTGM virtual topologies may define an NNTGM virtual topology footprint while its extent and its relative position inside the class of the corresponding indicative OV LV BPL topology depend on several factors with reference to eqs. (4)-(10), such as: (i) The inclusion or not of the examined indicative OV LV BPL topology in the TIM OV LV BPL topology

database during the NNTGM operation; (ii) the length of the distribution / branch line segments; and (iii) the number of the distribution / branch line segments. Note that 100 NNTGM virtual topologies are assumed to be generated per each OV LV BPL topology class and thus per indicative OV LV BPL topology excluding the LOS class. The correlation among the length and the number of distribution and branch line segments and the extent and relative position of the NNTGM virtual topology footprints are going to be investigated in the companion paper [23]. In the following subsection, the parameters of the NNTGM default operation settings that are going to be configured for the included OV LV BPL topologies of the TIM OV LV BPL topology database, which have already been defined in this subsection, are discussed.

NNTGM Default Operation Settings

In contrast with the default operation settings of NNIM-BNI and NNIM-LLA, the NNTGM default operation settings are strictly based on the database representativeness principle of [2] rather than the richness and the diversity of the applied big data, namely:

- For given examined indicative OV LV BPL topology, its number of the branches and its actual lengths of the distribution and branch lines are assumed to be known thus the OV LV BPL topologies that are going to be included in the TIM OV LV BPL topology database are defined by eqs. (4)-(8) in each case. For given examined indicative OV LV BPL topology, the total number of the OV LV BPL topologies that are added in the TIM OV LV BPL topology database is given in eq. (9) with the inclusion of the indicative OV LV BPL topology in the TIM OV LV BPL topology database that is the default option of the parameter. If the indicative OV LV BPL topology is excluded from the TIM OV LV BPL topology database, which is the variant option of the parameter, the total number of the OV LV BPL topologies that are added in the TIM OV LV BPL topology database is given from eq. (10) while t of eq. (5) and eq. (8) deals with only the positive integers. As the default operation setting values are concerned in this pair of papers, the length of the distribution and branch line segments are assumed to be equal to 1m and 1m, respectively, while the number of the distribution and branch line segments are assumed to be equal to 1 and 1, respectively. It is clear that the aforementioned NNTGM default operation setting parameter selection focuses on generating NNTGM virtual topology footprints that derive from the examined indicative OV LV BPL topology in each scenario while higher values of the aforementioned parameters are expected to relax the relative position and the extent of the NNTGM virtual topology footprints.
- The total distribution line length is assumed to be equal to 1,000 m in all the OV LV BPL topologies of the TIM OV LV BPL topology database. Also, the terminations of all the OV LV BPL topologies of the TIM OV LV BPL topology are assumed to be open-circuit ones in a similar way to the indicative OV LV BPL topologies of Table 1. With reference to [11, 33], the applied coupling scheme of interest in this pair of papers is the WtG^1 one.
- As the operating frequencies of interest are concerned in this pair of papers, the frequency range is assumed to be equal to 1-30 MHz while the flat-fading subchannel frequency spacing is equal to 1 MHz. Hence, the number of flat-fading subchannels is equal to 29. With reference to eq. (2), the amplitudes of the coupling scheme channel transfer functions are stored in dB in the TIM OV LV

BPL topology database for its OV LV BPL topologies with respect to the frequency.

- As the NNTGM is based on the MATLAB NN training program of [31, 32], the default participation percentages of the three phases of NNIM-BNI and NNIM-LLA of [2, 17, 31, 32] are also assumed in this pair of papers; say, training, validation and testing phases during the operation of NNTGM are assumed to be equal to 70%, 15% and 15%, respectively.

Apart from the default operation settings, to assess the performance of NNTGM, the channel attenuation metrics of ACA and RMS-DS are mathematically defined in the following subsection. Also, the definition of the aforementioned channel attenuation metrics remains a crucial task for the design of the OV LV BPL topology class maps as well as the impact evaluation of the operation settings of this subsection on the NNTGM virtual topology footprints.

NNTGM Channel Attenuation Metrics and NNTGM Topology Class Maps

With reference to eq. (3), the output of the NNTGM is the $Q \times 1$ NNTGM generated channel attenuation column vector $\mathbf{H}_{\text{NNTGM}}^{\text{OVLV,C}}\{\cdot\}$ for each of the generated OV LV BPL topologies. Based on the NNTGM generated channel attenuation column vector, the NNTGM channel attenuation metrics of ACA and RMS-DS can be mathematically defined, as follows [22]:

- *ACA*: As the BPL channel is frequency selective and $f_q, q = 1, \dots, Q$ are the operating frequencies when the examined frequency range is divided into Q flat-fading subchannels, ACA can be calculated for each NNTGM virtual topology by averaging over the flat-fading subchannels:

$$ACA_{\text{NNTGM}}^{\text{OVLV,C}} = \frac{1}{Q} \cdot \sum_{q=1}^Q |H_{\text{NNTGM}}^{\text{OVLV,C}}(f_q)|_{\text{dB}} \quad (11)$$

In fact, ACA depends on the multipath nature of the examined OV LV BPL topologies. In accordance with [22], when the number of branches is small and their electrical length is large, like in the rural and suburban cases of Table 1, shallow spectral notches are observed across the theoretical channel attenuation while low values of ACA are expected. Conversely, when the number of branches is large and the electrical length is small, like in the urban case A of Table 1, deep spectral notches are observed across the theoretical channel attenuation while high values of ACA are expected. In accordance with [8, 9, 29, 30], note that LOS case of Table 1 is characterized by the lowest value of ACA among all the OV LV BPL topologies (*i.e.*, either real or NNTGM virtual ones) since no spectral notches are observed. Therefore, NNTGM virtual topologies, which are generated by the respective indicative OV LV BPL topologies of Table 1, are expected to present similar theoretical channel attenuation behaviors and ACA with the ones of the respective indicative OV LV BPL topologies depending on the applied NNTGM operation settings.

- *RMS-DS*: Another channel attenuation metric that assesses the multipath richness of a BPL channel is RMS-DS. With reference to eq. (11), RMS-DS can be calculated for each NNTGM virtual topology as follows:

$$RMS - DS_{\text{NNTGM}}^{\text{OVLV,C}} = \sqrt{\frac{1}{Q} \cdot \sum_{q=1}^Q \left[|H_{\text{NNTGM}}^{\text{OVLV,C}}(f_q)|_{\text{dB}} - ACA_{\text{NNTGM}}^{\text{OVLV,C}} \right]^2} \quad (12)$$

In fact, the RMS-DS measures the average channel attenuation distance from ACA. It is expected that OV LV BPL topologies with rare and shallow spectral

notches across their theoretical channel attenuation present low values of RMS-DS whereas OV LV BPL topologies with frequent and deep spectral notches across their theoretical channel attenuation present high values of RMS-DS. Similarly to ACA, NNTGM virtual topologies, which are generated by the respective indicative OV LV BPL topologies of Table 1, are expected to present similar RMS-DS with the one of the respective indicative OV LV BPL topologies depending on the applied NNTGM operation settings.

From eqs. (11) and (12), it is obvious that each OV LV BPL topology can be characterized by a pair of values (ACA, RMS-DS) regardless of being either a real topology or a NNTGM virtual one. Also, the NNTGM virtual topologies are expected to have pairs of values that remain relatively close to the pair of values of their respective indicative OV LV BPL topology of Table 1 thus populating the class of the respective indicative OV LV BPL topology.

Similarly to the class maps of [18, 21, 34-36], new class maps can be plotted where their two axes correspond to the ACA and RMS-DS while each indicative OV LV BPL topology of Table 1 with its NNTGM virtual topologies can define its footprints on the class maps. Since NNTGM virtual topologies are expected to graphically approach their respective indicative OV LV BPL topology, the shape of the footprints of the indicative OV LV BPL topology classes concerning their relative positions and the sizes, depends on the applied NNTGM operation settings.

On the basis of the NNTGM default operation settings of Section 3.2, the impact of the following parameters, which have been identified in this paper, on the relative position and the size of the NNTGM virtual topology footprints is going to be assessed in the companion paper [23]: (i) The inclusion or not of the examined indicative OV LV BPL topology in the TIM OV LV BPL topology database during the NNTGM operation; (ii) the length of the distribution / branch line segments; and (iii) the number of the distribution / branch line segments.

Conclusions

In this first paper, the required theory for populating OV LV BPL topology classes by applying NNTGM has been proposed. First, it has been introduced NNTGM as the new member of the family products of NNIM-based methodologies; say, NNIM-BNI and NNIM-LLA. In fact, it has been shown that NNTGM is based on the reverse procedure of the NNIM-LLA since NNTGM can generate theoretical channel attenuation behaviors given the topological characteristics of an indicative OV LV BPL topology, when appropriate NNTGM operation settings are assumed. Prior to the detailed presentation of NNTGM in this paper, the indicative OV LV BPL topologies of topology classes had been reported while the TIM OV LV BPL topology database and NNIM-LLA, which are critical components for the operation of NNTGM, had been synopsized. Then, the definition of NNTGM has been given focusing on its NN behavior and its mathematical outputs. Apart from the NNTGM default operation settings, the parameters that affect the NNTGM performance and require additional study have been recognized, namely: (i) The inclusion or not of the examined indicative OV LV BPL topology in the TIM OV LV BPL topology database during the NNTGM operation; (ii) the length of the distribution / branch line segments; and (iii) the number of the distribution / branch line

segments. Actually, the aforementioned parameters are numerically evaluated in the companion paper of [23] for the OV LV BPL topology classes.

CONFLICTS OF INTEREST

The author declares that there is no conflict of interests regarding the publication of this paper.

References

- [1] Lazaropoulos, A. G., & Leligou, H. C. (2022). Fiber optics and broadband over power lines in smart grid: a communications system architecture for overhead high-voltage, medium-voltage and low-voltage power grids. *Progress in Electromagnetics Research B*, 95, 185-205. doi:<http://dx.doi.org/10.2528/PIERB22062502>
- [2] Lazaropoulos, A. G., & Leligou, H. C. (2023). Artificial Intelligence, Machine Learning and Neural Networks for Tomography in Smart Grid – Performance Comparison between Topology Identification Methodology and Neural Network Identification Methodology for the Distribution Line and Branch Line Length Approximation of Overhead Low-Voltage Broadband over Power Lines Network Topologies. *Trends in Renewable Energy*, 9(1), 34-77. doi:<http://dx.doi.org/10.17737/tre.2023.9.1.00149>
- [3] Amirshahi, P., & Kavehrad, M. (2006). High-frequency characteristics of overhead multiconductor power lines for broadband communications. *IEEE Journal on Selected Areas in Communications*, 24(7), 1292-1303. doi:<https://doi.org/10.1109/JSAC.2006.874399>
- [4] Sartenaer, T., & Delogne, P. (2006). Deterministic modeling of the (shielded) outdoor power line channel based on the multiconductor transmission line equations. *IEEE Journal on Selected areas in Communications*, 24(7), 1277-1291. doi:<https://doi.org/10.1109/JSAC.2006.874423>
- [5] Marcuzzi, F., & Tonello, A. M. (2023). Topology-based machine learning: Predicting power line communication quality in smart grids. *IEEE Access*, 11, 24851-24862. doi:<https://doi.org/10.1109/ACCESS.2023.3245361>
- [6] Lazaropoulos, A. G., & Leligou, H. C. (2024). Big Data and Neural Networks in Smart Grid - Part 1: The Impact of Piecewise Monotonic Data Approximation Methods on the Performance of Neural Network Identification Methodology for the Distribution Line and Branch Line Length Approximation of Overhead Low-Voltage Broadband over Powerlines Networks. *Trends in Renewable Energy*, 10, 30-66. doi:<https://doi.org/10.17737/tre.2024.10.1.00164>
- [7] Lazaropoulos, A. G., & Leligou, H. C. (2024). Big Data and Neural Networks in Smart Grid - Part 2: The Impact of Piecewise Monotonic Data Approximation Methods on the Performance of Neural Network Identification Methodology for the Distribution Line and Branch Line Length Approximation of Overhead Low-Voltage Broadband over Powerlines Networks. *Trends in Renewable Energy*, 10, 67-97. doi:<https://doi.org/10.17737/tre.2024.10.1.00165>

- [8] Lazaropoulos, A. G., & Cottis, P. G. (2009). Transmission characteristics of overhead medium voltage power line communication channels. *IEEE Transactions on Power Delivery*, 24(3), 1164-1173. doi:<https://doi.org/10.1109/TPWRD.2008.2008467>
- [9] Lazaropoulos, A. G., & Cottis, P. G. (2010). Capacity of overhead medium voltage power line communication channels. *IEEE Transactions on Power Delivery*, 25(2), 723-733. doi:<https://doi.org/10.1109/TPWRD.2009.2034907>
- [10] Lazaropoulos, A. G. (2012). Towards Modal Integration of Overhead and Underground Low-Voltage and Medium-Voltage Power Line Communication Channels in the Smart Grid Landscape: Model Expansion, Broadband Signal Transmission Characteristics, and Statistical Performance Metrics (Invited Paper). *International Scholarly Research Notices*, 2012(1), 121628. doi:<https://doi.org/10.5402/2012/121628>
- [11] Lazaropoulos, A. G. (2016). New coupling schemes for distribution broadband over power lines (BPL) networks. *Progress in Electromagnetics Research B*, 71, 39-54. doi:<http://dx.doi.org/10.2528/PIERB16081503>
- [12] Amirshahi-Shirazi, P. (2006). *Broadband access and home networking through powerline networks*. The Pennsylvania State University. Ph.D. dissertation.
- [13] Sartenaer, T. (2004). *Multiuser communications over frequency selective wired channels and applications to the powerline access network* (Doctoral dissertation, Catholic University of Louvain, Louvain-la-Neuve, Belgium).
- [14] Sartenaer, T., & Delogne, P. (2001). Powerline cables modelling for broadband communications. In *Proceedings of the IEEE International Conference on Power Line Communications and Its Applications*, Malmö, Sweden, pp. 331-337.
- [15] Lazaropoulos, A. G. (2017). Improvement of Power Systems Stability by Applying Topology Identification Methodology (TIM) and Fault and Instability Identification Methodology (FIIM) Study of the Overhead Medium-Voltage Broadband over Power Lines (OV MV BPL) Networks Case. *Trends in Renewable Energy*, 3(2), 102-128. doi:<http://dx.doi.org/10.17737/tre.2017.3.2.0034>
- [16] Lazaropoulos, A. G. (2016). Measurement Differences, Faults and Instabilities in Intelligent Energy Systems - Part 1: Identification of Overhead High-Voltage Broadband over Power Lines Network Topologies by Applying Topology Identification Methodology (TIM). *Trends in Renewable Energy*, 2, 85-112. doi: <http://dx.doi.org/10.17737/tre.2016.2.3.0026>
- [17] Lazaropoulos, A. G. (2021). Information Technology, Artificial Intelligence and Machine Learning in Smart Grid – Performance Comparison between Topology Identification Methodology and Neural Network Identification Methodology for the Branch Number Approximation of Overhead Low-Voltage Broadband over Power Lines Network Topologies. *Trends in Renewable Energy*, 7, 87-113. doi:<http://dx.doi.org/10.17737/tre.2021.7.1.00133>
- [18] Lazaropoulos, A. G. (2020). Business Analytics and IT in Smart Grid - Part 1: The Impact of Measurement Differences on the iSHM Class Map Footprints of Overhead Low-Voltage Broadband over Power Lines Topologies. *Trends in Renewable Energy*, 6(2), 156-186. doi:<http://dx.doi.org/10.17737/tre.2020.6.2.00117>
- [19] Lazaropoulos, A. G. (2020). Statistical Channel Modeling of Overhead Low Voltage Broadband over Power Lines (OV LV BPL) Networks - Part 1: The

- Theory of Class Map Footprints of Real OV LV BPL Topologies, Branch Line Faults and Hook-Style Energy Thefts. *Trends in Renewable Energy*, 6(1), 61-87. doi:<http://dx.doi.org/10.17737/tre.2020.6.1.00112>
- [20] Lazaropoulos, A. G. (2020). Business Analytics and IT in Smart Grid - Part 2: The Qualitative Mitigation Impact of Piecewise Monotonic Data Approximations on the iSHM Class Map Footprints of Overhead Low-Voltage Broadband over Power Lines Topologies Contaminated by Measurement Differences. *Trends in Renewable Energy*, 6(2), 187-213. doi:<http://dx.doi.org/10.17737/tre.2020.6.2.00118>
- [21] Lazaropoulos, A. G. (2020). Business Analytics and IT in Smart Grid - Part 3: New Application Aspect and the Quantitative Mitigation Analysis of Piecewise Monotonic Data Approximations on the iSHM Class Map Footprints of Overhead Low-Voltage Broadband over Power Lines Topologies Contaminated by Measurement Differences. *Trends in Renewable Energy*, 6(2), 214-233. doi:<http://dx.doi.org/10.17737/tre.2020.6.2.00119>
- [22] Lazaropoulos, A. G. (2012). Broadband Transmission and Statistical Performance Properties of Overhead High-Voltage Transmission Networks. *Journal of Computer Networks and Communications*, 2012(1), 875632. doi:<https://doi.org/10.1155/2012/875632>
- [23] Lazaropoulos, A. (2024). Virtual Topologies for Populating Overhead Low-Voltage Broadband over Powerlines Topology Classes by Exploiting Neural Network Topology Generator Methodology (NNTGM) - Part 2: Numerical Results. *Trends in Renewable Energy*, 10(3), 315-334. doi:<http://dx.doi.org/10.17737/tre.2024.10.3.00182>
- [24] Lazaropoulos, A. (2020). Statistical Channel Modeling of Overhead Low Voltage Broadband over Power Lines (OV LV BPL) Networks - Part 2: The Numerical Results of Class Map Footprints of Real OV LV BPL Topologies, Branch Line Faults and Hook Style Energy Thefts. *Trends in Renewable Energy*, 6(1), 88-109. doi:<http://dx.doi.org/10.17737/tre.2020.6.1.00113>
- [25] Lazaropoulos, A. G. (2013). Review and Progress towards the Capacity Boost of Overhead and Underground Medium-Voltage and Low-Voltage Broadband over Power Lines Networks: Cooperative Communications through Two- and Three-Hop Repeater Systems. *International Scholarly Research Notices*, 2013(1), 472190. doi:<https://doi.org/10.1155/2013/472190>
- [26] Meng, H., Chen, S., Guan, Y. L., Law, C. L., So, P. L., Gunawan, E., & Lie, T. T. (2004). Modeling of transfer characteristics for the broadband power line communication channel. *IEEE Transactions on Power delivery*, 19(3), 1057-1064. doi:<https://doi.org/10.1109/TPWRD.2004.824430>
- [27] Lazaropoulos, A. G. (2019). Statistical broadband over power lines channel modeling-Part 1: The theory of the statistical hybrid model. *Progress in Electromagnetics Research C*, 92, 1-16. doi:<http://dx.doi.org/10.2528/PIERC19012902>
- [28] Qu, B., Wang, H., Chen, Z., Zheng, Z., Han, Z., & Zhang, L. (2021). A Channel Selection Algorithm of Power Line Communication Network Base on Double-layer Cascade Artificial Neural Network. *Journal of Physics: Conference Series*, 2031(1), 012041. doi:<http://dx.doi.org/10.1088/1742-6596/2031/1/012041>
- [29] Lazaropoulos, A. G., & Cottis, P. G. (2010). Broadband transmission via underground medium-voltage power lines-Part I: transmission characteristics.

- IEEE Transactions on Power Delivery*, 25(4), 2414-2424.
doi:<https://doi.org/10.1109/TPWRD.2010.2048929>
- [30] Lazaropoulos, A. G., & Cottis, P. G. (2010). Broadband transmission via underground medium-voltage power lines-Part II: capacity. *IEEE Transactions on Power Delivery*, 25(4), 2425-2434.
doi:<https://doi.org/10.1109/TPWRD.2010.2052113>
- [31] Okoh, D. (2016). *Computer neural networks on MATLAB*. CreateSpace Independent Publishing Platform.
- [32] Okoh, D. (2020). *Neural Network Training Code*. Available at: <https://www.mathworks.com/matlabcentral/fileexchange/59362-neural-network-training-code> (Accessed: 22 April 2020).
- [33] Lazaropoulos, A. G. (2018). Broadband Performance Metrics and Regression Approximations of the New Coupling Schemes for Distribution Broadband over Power Lines (BPL) Networks. *Trends in Renewable Energy*, 4(1), 43-73.
doi:<http://dx.doi.org/10.17737/tre.2018.4.1.0059>
- [34] Lazaropoulos, A. G. (2019). Virtual Indicative Broadband over Power Lines Topologies for Respective Subclasses by Adjusting Channel Attenuation Statistical Distribution Parameters of Statistical Hybrid Models (Class Maps) – Part 1: Theory. *Trends in Renewable Energy*, 5(3), 237-257.
doi:<http://dx.doi.org/10.17737/tre.2019.5.3.0099>
- [35] Lazaropoulos, A. G. (2019). Virtual Indicative Broadband over Power Lines Topologies for Respective Subclasses by Adjusting Channel Attenuation Statistical Distribution Parameters of Statistical Hybrid Models (Class Maps) – Part 2: Numerical Results for the Overhead and Underground Medium-Voltage Power Grids. *Trends in Renewable Energy*, 5(3), 258-281.
doi:<http://dx.doi.org/10.17737/tre.2019.5.3.00100>
- [36] Lazaropoulos, A. G. (2019). Virtual Indicative Broadband over Power Lines Topologies for Respective Subclasses by Adjusting Channel Attenuation Statistical Distribution Parameters of Statistical Hybrid Models (Class Maps) – Part 3: The Case of Overhead Transmission Power Grids. *Trends in Renewable Energy*, 5(3), 282-306. doi:<http://dx.doi.org/10.17737/tre.2019.5.3.00101>

Article copyright: © 2024 Athanasios G. Lazaropoulos. This is an open access article distributed under the terms of the [Creative Commons Attribution 4.0 International License](https://creativecommons.org/licenses/by/4.0/), which permits unrestricted use and distribution provided the original author and source are credited.



Virtual Topologies for Populating Overhead Low-Voltage Broadband over Powerlines Topology Classes by Exploiting Neural Network Topology Generator Methodology (NNTGM) - Part 2: Numerical Results

Athanasios G. Lazaropoulos*

*School of Electrical and Computer Engineering / National Technical University of Athens /
9 Iroon Polytechniou Street / Zografou, GR 15780*

Received July 23, 2024; Accepted September 1, 2024; Published September 15, 2024

In [1], Neural Network Topology Generator Methodology (NNTGM) has been theoretically proposed, so that its generated overhead low-voltage broadband over power lines topologies (NNTGM OV LV BPL topologies) may populate the existing OV LV BPL topology classes. Apart from the methodology, NNTGM default operation settings and the applied performance metrics, such as the average theoretical channel attenuation (ACA) and the root mean square delay-spread (RMS-DS), have been presented in [1]. In this companion paper, the new OV LV BPL topology class maps, which are defined by the graphical combination of ACA and RMS-DS of the OV LV BPL topologies, are shown. With reference to the graphical combination of ACA and RMS-DS, NNTGM OV LV BPL topology footprints for given indicative OV LV BPL topology are demonstrated on the OV LV BPL topology class maps. The impact on the relative position and the size of the NNTGM OV LV BPL topology footprints is assessed with reference to the following factors that affect the preparation of the Topology Identification Methodology (TIM) OV LV BPL topology database being used during the NNTGM operation, namely: (i) The inclusion or not of the examined indicative OV LV BPL topology; (ii) the length of the distribution / branch line segments; and (iii) the number of the distribution / branch line segments. The performance assessment of NNTGM is supported by suitable Graphical Performance Indicators (GPIs).

Keywords: Smart Grid; Broadband over Power Lines (BPL) networks; Power Line Communications (PLC); Distribution and Transmission Power Grids; Neural Networks; Simulation; Modeling

Introduction

In Broadband over Power Lines (BPL) networks, populating BPL topology classes can become a crucial task for optimizing network performance and reliability. Neural Network Topology Generator Methodology (NNTGM) that has been theoretically proposed in [1] addresses this need by generating overhead low-voltage BPL topologies (NNTGM OV LV BPL topologies) based on the indicative OV LV BPL topologies of the topology classes, thus simulating channel attenuation behavior for NNTGM virtual topologies that maintain the same topological characteristics as the indicative ones.

*Corresponding author: AGLazaropoulos@gmail.com

Actually, NNTGM, which is the new member of the neural network identification methodology (NNIM) -based family products; say, neural network identification methodology for the branch number identification (NNIM-BNI) [2] and neural network identification methodology for the line length approximation (NNIM-LLA) [3-5], enhances the speed of populating OV LV BPL topology classes, thus facilitating better planning and management of OV LV BPL networks. Exploiting artificial intelligence (AI), machine learning (ML) and neural network (NN) features, the ability of NNTGM to create virtual topologies that imitate the characteristics of real-world topologies may allow communications engineers to predict and mitigate potential issues, leading to more robust and resilient communication systems [6-8]. Therefore, the adoption of NNTGM for populating OV LV BPL topology classes offers a significant advancement in the field of BPL networks, ensuring efficient and reliable network operation.

To examine the statistical and graphical similarity of the NNTGM OV LV BPL topologies with the respective indicative OV LV BPL topologies and to evaluate the procedure of populating of the OV LV BPL topology classes, new class maps have been described in [1] and are going to be implemented in this companion paper. The new class maps exploit the NNTGM performance metrics; say, the average theoretical channel attenuation (ACA) and the root mean square delay-spread (RMS-DS) [9]. With reference to other versions of class maps that have been used in OV LV BPL topologies so far [10]-[13], the OV LV BPL topology class maps, which are based on the graphical ACA / RMS-DS combination, allows the graphical examination of the vicinity of the NNTGM OV LV BPL topologies to their respective indicative OV LV BPL topologies while the group of the NNTGM OV LV BPL topologies defines the NNTGM virtual topology footprint. Then, the impact of the parameters of the NNTGM default operation settings on the relative position and the size of the NNTGM virtual topology footprints are further graphically assessed in this companion paper through the prism of the Graphical Performance Indicators (GPIs); say, the percentage of the NNTGM OV LV BPL topologies that remain inside the OV LV BPL topology class of their respective indicative OV LV BPL topology and the percentage of the NNTGM OV LV BPL topologies that remain inside specific ACA / RMS-DS limits with respect to their indicative OV LV BPL topology. In accordance with [1] and with reference to the class maps and the GPIs, the impact of the following parameters on the NNTGM virtual topology footprints is going to be assessed, namely: (i) The inclusion or not of the examined indicative OV LV BPL topology in the Topology Identification Methodology (TIM) OV LV BPL topology database during the NNTGM operation; (ii) the length of the distribution / branch line segments; and (iii) the number of the distribution / branch line segments.

The rest of this paper is organized as follows: Section 2 presents the new class maps with respect to the indicative OV LV BPL topologies of [1]. Then, the superimposition of NNTGM virtual topology footprints on the class maps and the application of GPIs are analyzed when the NNTGM default operation settings of [1] are adopted. In Section 3, the impact of the aforementioned parameters of the NNTGM default operation settings on the NNTGM virtual topology footprints and GPIs is assessed. Section 4 concludes this paper.

OV LV BPL Topology Class Maps and NNTGM Default Operation Settings

In this Section, the four indicative OV LV BPL topologies that are the representative ones of the four main OV LV BPL topology classes of [1, 10-14] are here adopted. With respect to these OV LV BPL topology classes, the OV LV BPL topology class map, which is based on the graphical ACA / RMS-DS combination, is first presented with reference to the NNTGM default operation settings of [1]. Then, NNTGM virtual OV LV BPL topologies per indicative OV LV BPL topology are graphically grouped into the respective NNTGM virtual topology footprints that are going to be superimposed on the class maps. Finally, APIs that are going to be applied across the result presentation of this companion paper are reported.

OV LV BPL Topologies and Respective Topology Classes

As already mentioned in [1, 3, 15-19], OV LV BPL networks are divided into cascaded OV LV BPL topologies of typical lengths of 1000 m while a typical OV LV BPL topology is shown in Figure 1 of [1]. In Table 1 of [1], the topological characteristics for the four indicative OV LV BPL topologies of interest –*i.e.*, Line-Of-Sight (LOS) case, rural case, suburban case and urban case A– are reported. The aforementioned four indicative OV LV BPL topologies are the representative ones of the respective OV LV BPL topology classes, which have extensively been used until now [10, 12, 13]. Deterministic Hybrid Model (DHM), which describes the BPL signal propagation and transmission across the OV LV BPL topologies [16, 17, 20-26], is here used for evaluating the theoretical channel attenuation of the four indicative OV LV BPL topologies with reference to the NNTGM default operation settings analyzed in [1]. Then, NNTGM performance metrics of ACA and RMS-DS that are going to be used in class maps are calculated for the four indicative OV LV BPL topologies.

In Figure 1, the OV LV BPL topology class map, which is based on the graphical ACA / RMS-DS combination of the four indicative OV LV BPL topologies, is plotted with reference to ACA and RMS-DS when the NNTGM default operation settings of [1] are applied. From Figure 1, the following observations can be made:

- In accordance with [16, 20, 27, 28], LOS case is characterized by the lowest value of ACA among all the OV LV BPL topologies. Since no spectral notches are observed, low value of RMS-DS is also shown. Anyway, LOS case is a unique OV LV BPL topology and there is no need for supporting an OV LV BPL topology class with NNTGM virtual topologies. In the rest of this companion paper, LOS case is not presented on the class maps and is not populated by NNTGM virtual topologies.
- In accordance with [10, 11, 16, 17, 20], in general terms, as the number of branches of the OV LV BPL topologies increases, their theoretical channel attenuation described by DHM is getting higher thus entailing higher values of ACA. Conversely, as the length of branches of the OV LV BPL topologies decreases, their theoretical channel attenuation described by DHM is getting higher due to the resulting stressed multipath environment thus entailing higher values of RMS-DS. The combination of the aforementioned two general principles of the OV LV BPL topologies explains the ranking and the position of the four indicative OV LV BPL topologies on the class map of Figure 1.

- In order to define the OV LV BPL topology class areas, the class borderlines that spatially demarcate the class areas are roughly derived as the median lines between the neighboring indicative OV LV BPL topologies that anyway define the class areas. Beyond that, around each indicative OV LV BPL topology, the ACA / RMS-DS box of $\pm 10\%$ is here defined and represented with dashed lines around each examined topology in Figure 1, resulting from the variation of $\pm 10\%$ in the values of ACA and RMS-DS of the examined topology.

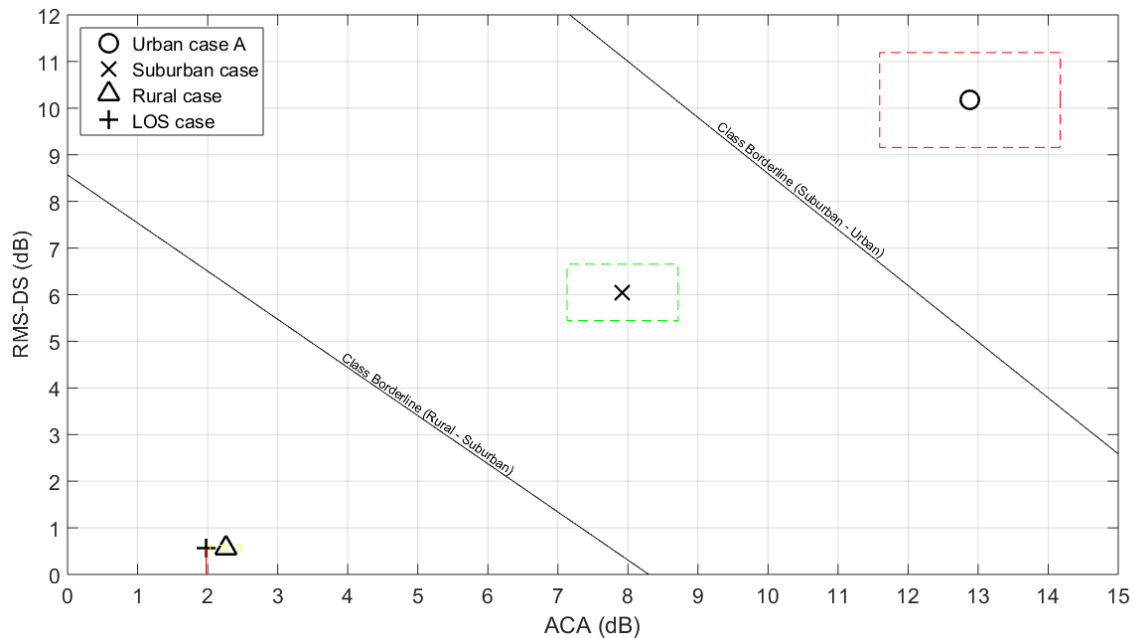


Fig. 1. OV LV BPL topology class map when the NNTGM default operation settings are applied.

OV LV BPL Topology Class Map and NNTGM Virtual Topology Footprints

NNTGM virtual topologies are expected to present similar theoretical channel attenuation behaviors, ACA and RMS-DS with the ones of the respective indicative OV LV BPL topologies but not the same ones. This inherent property of NNTGM virtual topologies securely allows populating of the OV LV BPL topology classes given the indicative OV LV BPL topology in each case. In accordance with the NNTGM default operation settings of [1], 100 NNTGM virtual topologies are assumed to be generated per each indicative OV LV BPL topology thus forming the respective NNTGM virtual topology footprints.

In Figure 2, the OV LV BPL topology class map of Figure 1 enhanced with the NNTGM virtual topology footprints of the rural case, suburban case and urban case A is presented. Observing Figure 2, it is evident that 100 NNTGM virtual topologies are related with each indicative OV LV BPL topology thus defining respective footprints that remain inside the respective class area in all the classes examined. In fact, the majority of the NNTGM virtual topologies remain significantly close to the respective indicative OV LV BPL topologies and inside the ACA / RMS-DS box of $\pm 10\%$ in each case.

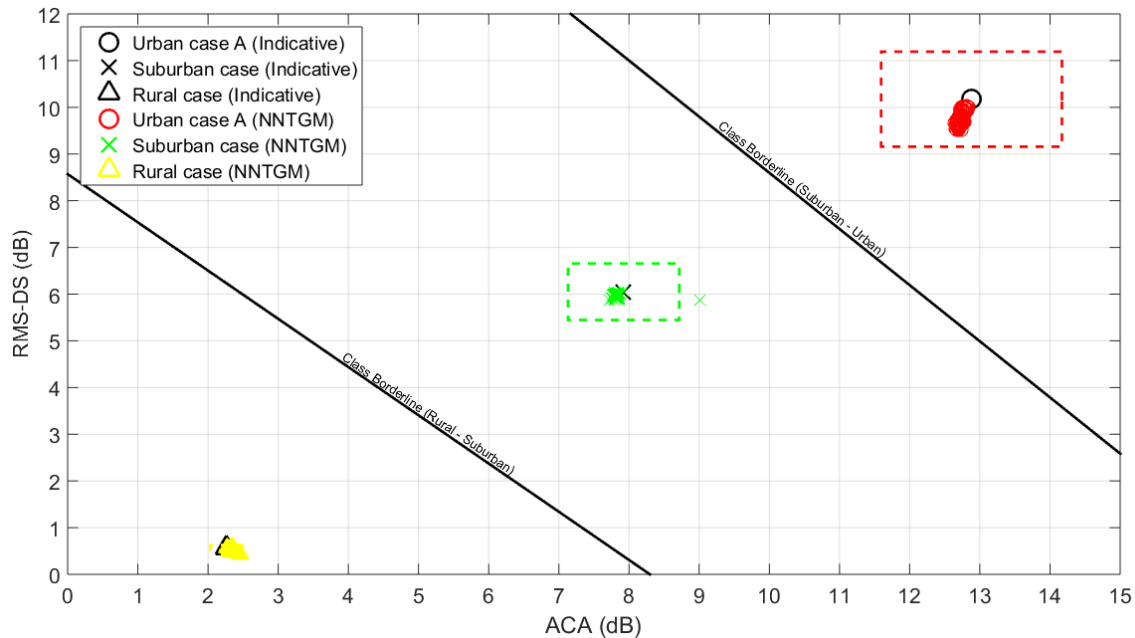


Fig. 2. OV LV BPL topology class map with NNTGM virtual topology footprints of the three indicative OV LV BPL topologies when the NNTGM default operation settings are applied.

On the basis of the aforementioned observations regarding the extent and the relative position of NNTGM virtual topology footprints in Figure 2, two GPIs can be defined in order to evaluate the populating of the OV LV BPL topology classes, namely:

- *Inside the class:* This GPI has to do with the percentage of the NNTGM OV LV BPL topologies that remain inside the OV LV BPL topology class of their respective indicative OV LV BPL topology, and
- *Inside the box:* The percentage of the NNTGM OV LV BPL topologies that remain inside the ACA / RMS-DS box of $\pm 10\%$ with respect to their indicative OV LV BPL topology.

With reference to Figure 2, the aforementioned GPIs are applied to the NNTGM OV LV BPL topologies of the three OV LV BPL topology classes and are reported in Table 1. Indeed, the three NNTGM virtual topology footprints remain tightly near their respective indicative OV LV BPL topologies when the NNTGM default operation settings are assumed. 100% of the NNTGM OV LV BPL topologies remain inside the OV LV BPL topology class regardless of the examined indicative OV LV BPL topologies while the majority of the NNTGM OV LV BPL topologies (*i.e.*, above 84%) remain inside the ACA / RMS-DS box of $\pm 10\%$ of the examined indicative OV LV BPL topologies. From Table 1, it is evident that NNTGM default operation settings may support NNTGM virtual topology footprints of reduced extents with positions that stand close to the indicative OV LV BPL topologies of origin.

The impact of the parameters of the NNTGM default operation settings on the relative position and the size of the NNTGM virtual topology footprints can further be graphically examined and numerically assessed by GPIs so that footprints of custom

Table 1. GPIs of the NNTGM OV LV BPL topologies of the three OV LV BPL topology classes (NNTGM default operation settings are applied)

GPI	OV LV BPL topology class		
	Rural case class	Suburban case class	Urban case A class
Inside the class (%)	100	100	100
Inside the box (%)	84	99	100

relative positions and size can later be produced on demand. In accordance with [1] and with reference to the class maps and the GPIs, the effect of certain parameters of the NNTGM default operation settings of [1] on the NNTGM virtual topology footprints is going to be assessed in the following Section.

The Impact of the Different NNTGM Operation Settings on the NNTGM Virtual Topology Footprints

In this Section, the effect of the following parameters of the NNTGM default operation settings of [1] on the NNTGM virtual topology footprints is going to be investigated, namely: (i) The inclusion or not of the examined indicative OV LV BPL topology in the TIM OV LV BPL topology database during the NNTGM operation; (ii) the length of the distribution / branch line segments; and (iii) the number of the distribution / branch line segments.

Excluding Indicative OV LV BPL Topologies from TIM OV LV BPL Topology Database and Its Impact on NNTGM Virtual Topology Footprints

In accordance with [1], the NNTGM default operation settings assume that the inclusion of the indicative OV LV BPL topology in the TIM OV LV BPL topology database during the operation of NNTGM for given indicative OV LV BPL topology is the default option of the parameter. Indeed, the total number of the OV LV BPL topologies that are added in the TIM OV LV BPL topology database is given in eq. (9) of [1]. The concept for including the indicative OV LV BPL topology in the TIM OV LV BPL topology aims at preserving the representativeness principle of [3] for the TIM OV LV BPL topology database rather than enhancing the richness and the diversity of the applied big data.

In this subsection, the option of excluding the indicative OV LV BPL topology from the TIM OV LV BPL topology database during the operation of NNTGM for given indicative OV LV BPL topology is investigated. Anyway, the theoretical study of the aforementioned exclusion, which is the variant option of the parameter, concerning the total number of the OV LV BPL topologies that are added in the TIM OV LV BPL topology database has been given in eq. (10) of [1]. Here, the preservation of the representativeness of the TIM OV LV BPL topology database is challenged through excluding the indicative OV LV BPL topology from the TIM OV LV BPL topology database while the remaining NNTGM default operation settings of [1], which anyway support NNTGM virtual topology footprints of reduced extents as presented in Section 2.2, remain the same.

In Figure 3, the OV LV BPL topology class map and the NNTGM virtual topology footprints of the rural case, suburban case and urban case A are illustrated when the NNTGM default operation settings are applied but the indicative OV LV BPL

topologies are excluded from the TIM OV LV BPL topology database in each examined case. With reference to Figure 3, the GPIs of Section 2.2 are applied to the NNTGM virtual topology footprints of the rural case, suburban case and urban case A and their values are reported in Table 2.

Comparing Figure 3 and Table 2 with Figure 2 and Table 1, respectively, it is evident that the representativeness of the TIM OV LV BPL topology database still occurs even though the indicative OV LV BPL topologies have been excluded from the TIM OV LV BPL topology database. In fact, all the NNTGM virtual topology footprints after the exclusion of the indicative OV LV BPL topologies present almost the same extents, relative positions and GPIs with all the respective NNTGM virtual topology footprints occurring with the inclusion of the indicative OV LV BPL topologies. Anyway, the NNTGM default operation settings allow the TIM OV LV BPL topology database to consist of OV LV BPL topologies presenting similar channel attenuation behavior to the examined indicative OV LV BPL topology in each case. Therefore, the exclusion of the indicative OV LV BPL topology little affects NNTGM virtual topology footprints and corresponding GPIs. Anyway, like the other NNIM-based family products, NNTGM is a stochastic methodology where AI, ML and NN coexist and for that reason small GPI percentage differences are expected even for executions of the same set of NNTGM operation settings. In the following Section, the impacts of the length of the distribution line segments and the number of the distribution line segments on the NNTGM virtual topology footprints are benchmarked.

The Impact of Distribution Line Parameters of the NNTGM Default Operation Settings on NNTGM Virtual Topology Footprints

In accordance with [1], the NNTGM default operation settings assume that the length of the distribution line segments and their number are equal to 1m and 1, respectively. In fact, the length and the number of distribution line segments affect the degree of variation of the amplitude of the coupling scheme channel transfer functions of the OV LV BPL topologies being included in the TIM OV LV BPL topology database that further is going to affect the NNTGM results.

Length of Distribution Line Segments of the NNTGM Default Operation Settings and NNTGM Virtual Topology Footprints

In Figure 4(a), the OV LV BPL topology class map and the NNTGM virtual topology footprints of the rural case, suburban case and urban case A are illustrated when the NNTGM default operation settings are applied but the length of the distribution line segments is equal to 10m. In Figure 4(b), similar plots are given with Figure 4(a) but the length of the distribution line segments is equal to 50m. With reference to Figures 4(a) and 4(b), the GPIs of this companion paper are applied to the NNTGM virtual topology footprints of the rural case, suburban case and urban case A and their values are comparatively reported in Table 3.

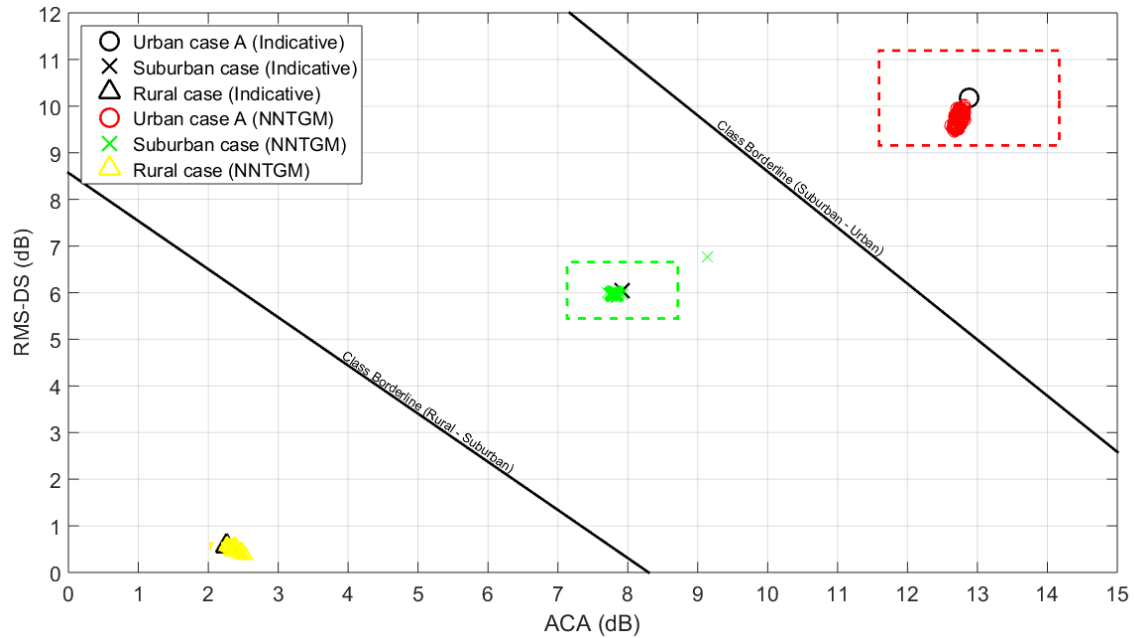


Fig. 3. OV LV BPL topology class map with NNTGM virtual topology footprints of the three indicative OV LV BPL topologies when the NNTGM default operation settings are applied but the indicative OV LV BPL topologies are excluded from the TIM OV LV BPL topology database.

Table 2. GPIs of the NNTGM OV LV BPL topologies of the three OV LV BPL topology classes (NNTGM default operation settings are applied without the indicative OV LV BPL topologies during the preparation of TIM OV LV BPL topology database)

GPI	OV LV BPL topology class		
	Rural case class	Suburban case class	Urban case A class
Inside the class (%)	100	100	100
Inside the box (%)	85	99	100

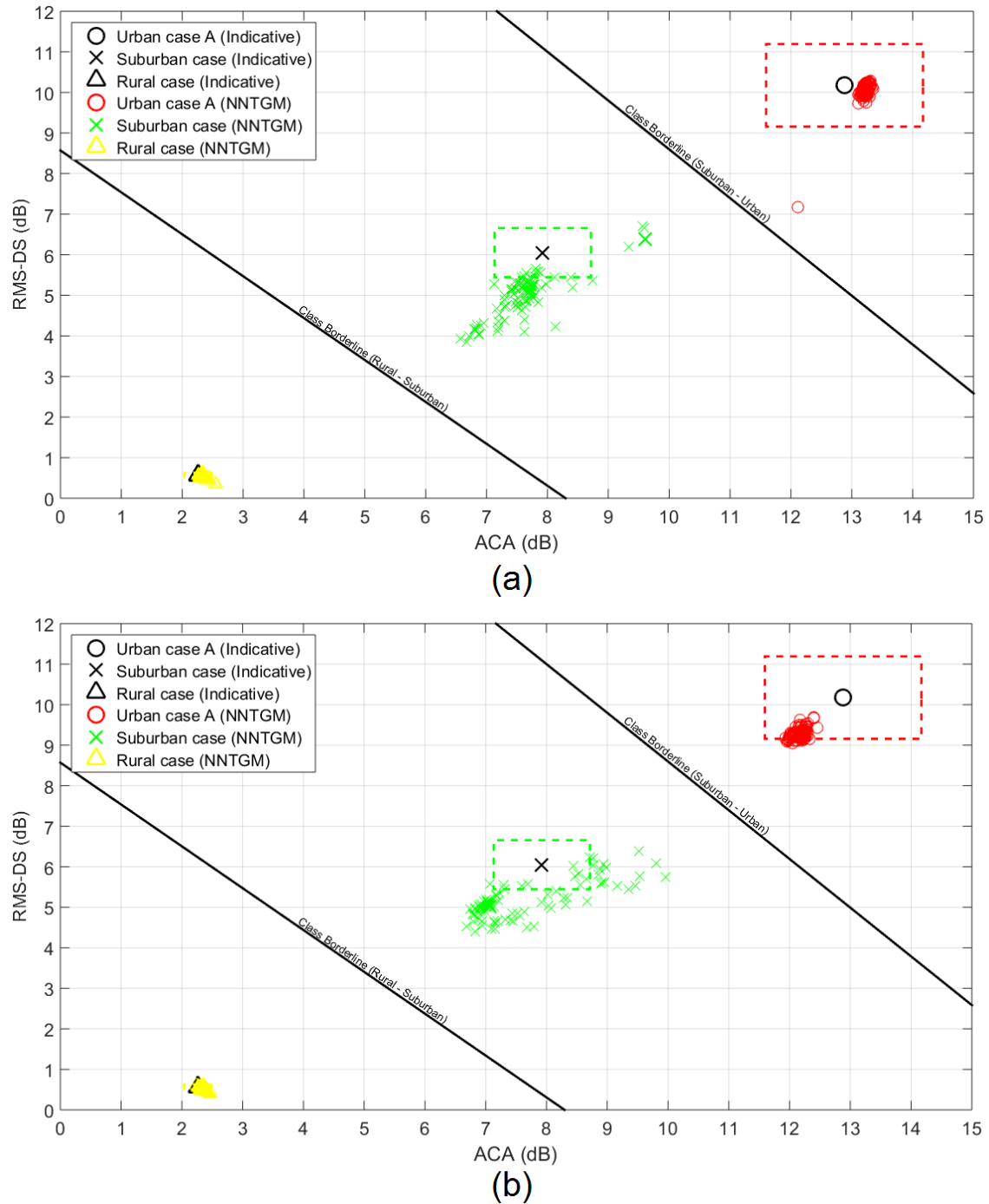


Fig. 4. OV LV BPL topology class map with NNTGM virtual topology footprints of the three indicative OV LV BPL topologies when the NNTGM default operation settings are applied and various lengths of the distribution line segments are considered. (a) 10m, (b) 50m

Table 3. GPIs of the NNTGM OV LV BPL topologies of the three OV LV BPL topology classes (NNTGM default operation settings are applied with various lengths of the distribution line segments)

GPI	OV LV BPL topology class (Distribution line segment length)					
	Rural case class		Suburban case class		Urban case A class	
	(10m)	(50m)	(10m)	(50m)	(10m)	(50m)
Inside the class (%)	100	100	100	100	100	100
Inside the box (%)	75	82	10	9	99	85

Comparing Figures 4(a), 4(b) with Figure 2, it is evident that the change of the distribution line parameter values of the NNTGM default operation settings has a direct impact on the size and the relative position of the NNTGM virtual topology footprints of the examined indicative OV LV BPL topologies. Indeed, as the length of the distribution line segments changes, the NNTGM virtual topology footprints move away from their indicative OV LV BPL topology while their extents get wider thus sparsely populating the respective OV LV BPL topology classes. Although the NNTGM virtual topology footprints cover greater regions of their respective OV LV BPL topology class, they remain strictly within the class boundaries with reference to Table 3.

Comparing “inside the box” GPIs of Tables 3 with the ones of Table 1, it is evident that the length change of the distribution line segments critically affects the position of the NNTGM virtual topology footprints in relation with the ACA / RMS-DS box of $\pm 10\%$ of their respective indicative OV LV BPL topologies. The movement and the wider extents of the NNTGM virtual topology footprints of Figures 4(a) and 4(b) are reflected on lower values of their respective “inside the box” GPIs. More specifically, the “inside the box” GPIs of the NNTGM virtual topology footprints of the suburban case are the most affected ones by the change of the lengths of the distribution line segments since the two branches of the indicative suburban case allow NNTGM to enrich the respective TIM OV LV BPL topology database with OV LV BPL topologies that vary regarding their channel attenuation behavior as well as their multipath environment due to the branch movement. In a similar way, the change of the lengths of the distribution line segments has a less severe effect on the “inside the box” GPIs of the NNTGM virtual topology footprints of the rural case, since the one electrically long branch of the indicative rural case does not allow NNTGM to significantly enhance the diversity of the respective TIM OV LV BPL topology database. In contrast, the different versions of the anyway heavy multipath environment of the indicative urban case A that come from the length increase of the distribution line segments and are included in the TIM OV LV BPL topology database has a small effect on the “inside the box” GPIs of the NNTGM virtual topology footprints of the urban case A.

From the perspective of sparse populating of classes, the increase of the length of the distribution line segments mainly supports sparse NNTGM virtual topology footprints for the suburban class. In the following subsections, apart from the length, the impact of the number of distribution line segments of the NNTGM default operation settings that is expected to focus in a similar way to this subsection on the diversity and the high number of OV LV BPL topologies in the TIM OV LV BPL topology database is investigated.

Number of Distribution Line Segments of the NNTGM Default Operation Settings and NNTGM Virtual Topology Footprints

In Figure 5, the OV LV BPL topology class map and the NNTGM virtual topology footprints of the rural case, suburban case and urban case A are illustrated when the NNTGM default operation settings are applied but the number of the distribution line segments is equal to 2. With reference to Figure 5, the GPIs of this companion paper are applied to the NNTGM virtual topology footprints of the rural case, suburban case and urban case A and their values are reported in Table 4.

Comparing Figure 5 with Figures 4(a) and 4(b), it is evident that the number increase of the distribution line segments of the NNTGM default operation settings presents similar results with the length increase of the distribution line segments on the size and the relative position of the NNTGM virtual topology footprints of the examined indicative OV LV BPL topologies but in a more drastic way for the suburban case. As the position of the NNTGM virtual topology footprints is concerned, even if the default length of the distribution line segments, which is assumed to be equal to 1m, is assumed, the number increase of the distribution line segments achieves to move almost the entire NNTGM virtual topology footprint of the suburban case outside the ACA / RMS-DS box of $\pm 10\%$ of the indicative suburban case. Conversely, the NNTGM virtual topology footprints of the rural case and the urban case A remain inside the ACA / RMS-DS boxes of $\pm 10\%$ of the respective indicative OV LV BPL topologies. Anyway, all the NNTGM virtual topology footprints remain inside the classes of the respective indicative OV LV BPL topologies. In comparison with Figure 2, the NNTGM virtual topology footprints of Figure 5 present comparable relative positions and extents with the ones of Figure 2 except for the NNTGM virtual topology footprint of the suburban case that is significantly dislocated with larger extent due to the fact that OV LV BPL topologies of lengths of distribution line segments that are equal to $2 \times 1\text{m} = 2\text{m}$ are also included in the TIM OV LV BPL topology database in accordance with eq. (5) of [1]. In comparison with Figures 4(a) and (b), the extent of the NNTGM virtual topology footprints of Figure 5 is significantly reduced than the ones of OV LV BPL topologies with the increased lengths of the distribution line segments of the NNTGM default operation settings.

Synoptically, the impact of the changes of the lengths and the number of distribution line segments of the NNTGM default operation settings on the NNTGM virtual topology footprints of the examined indicative OV LV BPL topologies present similarities concerning their position, their extent and the affected indicative OV LV BPL topologies. In accordance with GPIs, the most affected NNTGM virtual topology footprint from the distribution line segment parameter changes of the NNTGM default operation settings is the one of the suburban case as well as the one of the rural case but in lower intensity. The changes of the distribution line segment parameters of the NNTGM default operation settings little affect the NNTGM virtual topology footprints of the urban case A. In the following subsection, the impacts of the length and the number of the branch line segments on the NNTGM virtual topology footprints are examined.

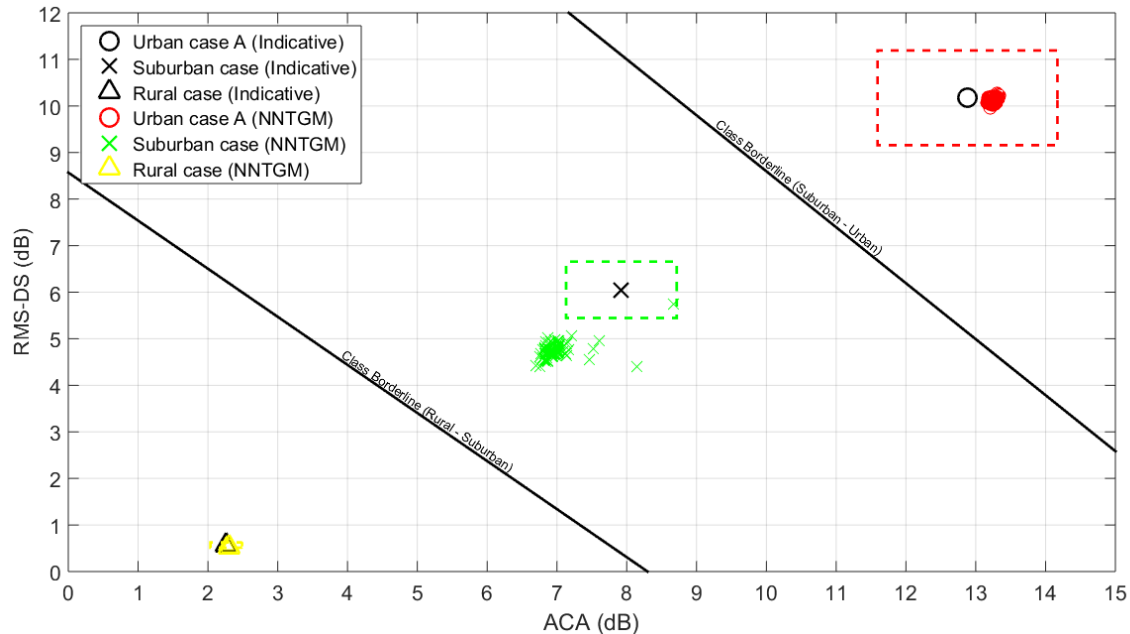


Fig. 5. OV LV BPL topology class map with NNTGM virtual topology footprints of the three indicative OV LV BPL topologies when the NNTGM default operation settings are applied and 2 distribution line segments are considered.

Table 4. GPIs of the NNTGM OV LV BPL topologies of the three OV LV BPL topology classes (NNTGM default operation settings are applied when 2 distribution line segments are assumed)

GPI	OV LV BPL topology class		
	Rural case class	Suburban case class	Urban case A class
Inside the class(%)	100	100	100
Inside the box (%)	100	1	100

The Impact of Branch Line Parameters of the NNTGM Default Operation Settings on NNTGM Virtual Topology Footprints

In accordance with [1], the NNTGM default operation settings assume that the length of the branch line segments and their number are equal to 1m and 1, respectively. In fact, the length and the number of branch line segments affect the number and the depth of the notches of the amplitude of the coupling scheme channel transfer functions of the OV LV BPL topologies being included in the TIM OV LV BPL topology database that further are going to affect the corresponding NNTGM results.

Length of Branch Line Segments of the NNTGM Default Operation Settings and NNTGM Virtual Topology Footprints

In Figure 6(a), the OV LV BPL topology class map and the NNTGM virtual topology footprints of the rural case, suburban case and urban case A are plotted when the NNTGM default operation settings are applied but the length of the branch line segments is equal to 4m. In Figure 6(b), similar plots are given with Figure 6(a) but the length of the branch line segments is equal to 8m. With reference to Figures 6(a) and 6(b), the GPIs of this companion paper are applied to the NNTGM virtual topology

footprints of the rural case, suburban case and urban case A and their values are comparatively reported in Table 5.

Comparing Figures 6(a) and 6(b) with Figures 4(a) and 4(b), it is clear that the length change of the branch line segments of the NNTGM default operation settings has an opposite effect on the NNTGM virtual topology footprints of the examined indicative OV LV BPL topologies in relation with the impact of length increase of the distribution line segments. In fact, the length increase of the branch line segments primarily affects the NNTGM virtual topology footprints of the rural case and urban case A. The number and the lengths of the branches determine the number and the depth of the spectral notches across the coupling scheme channel transfer functions of the OV LV BPL topologies being included in the TIM OV LV BPL topology database; say, the intensity of the multipath environment of the OV LV BPL topologies. As the length of the branch line segments changes, the NNTGM virtual topology footprints spread rapidly away from the respective indicative OV LV BPL topologies with wide extents thus sparsely populating the respective OV LV BPL topology classes. In the case of the length increase of the branch line segments of this subsection, the NNTGM virtual topology footprints of rural case and urban case A cover great regions that are beyond their respective OV LV BPL topology class borderlines in many times.

Comparing GPIs of Tables 5 and 3, the opposite effect of the length increase of the branch line segments on the NNTGM virtual topology footprints of the examined indicative OV LV BPL topologies with respect to the length increase of the distribution line segments is quantitatively verified. As the “inside the class” lines of Table 5 are concerned, the “inside the class” GPIs of the NNTGM virtual topology footprints of the rural case are the only affected ones by the change of the length of the branch line segments. As the “inside the box” lines of Table 5 are regarded, the “inside the box” GPIs of the NNTGM virtual topology footprints of primarily the urban case A and of secondarily the rural case are the most affected. In the aforementioned cases, NNTGM enriches the respective TIM OV LV BPL topology database with OV LV BPL topologies that vary regarding their channel attenuation behavior in terms of the number and the depth of notches. In fact, the “inside the box” GPI deterioration for the NNTGM virtual topology footprints of the urban case A is greater when the length of the branch line segments is equal to 4m rather than 8m.

From the perspective of sparsely populating the OV LV BPL topology classes, the increase of the length of the branch line segments mainly supports sparse NNTGM virtual topology footprints for the rural and urban classes. Here, it should be highlighted the complementary NNTGM operation of the change of the length of the branch line segments of this subsection to the one of the change of the length of the distribution line segments, which has been presented in Section 3.2.1. Except for the increase of the length of the branch line segments, the impact of the number of branch line segments of the NNTGM default operation settings on the NNTGM virtual topology footprints is investigated in the following subsection.

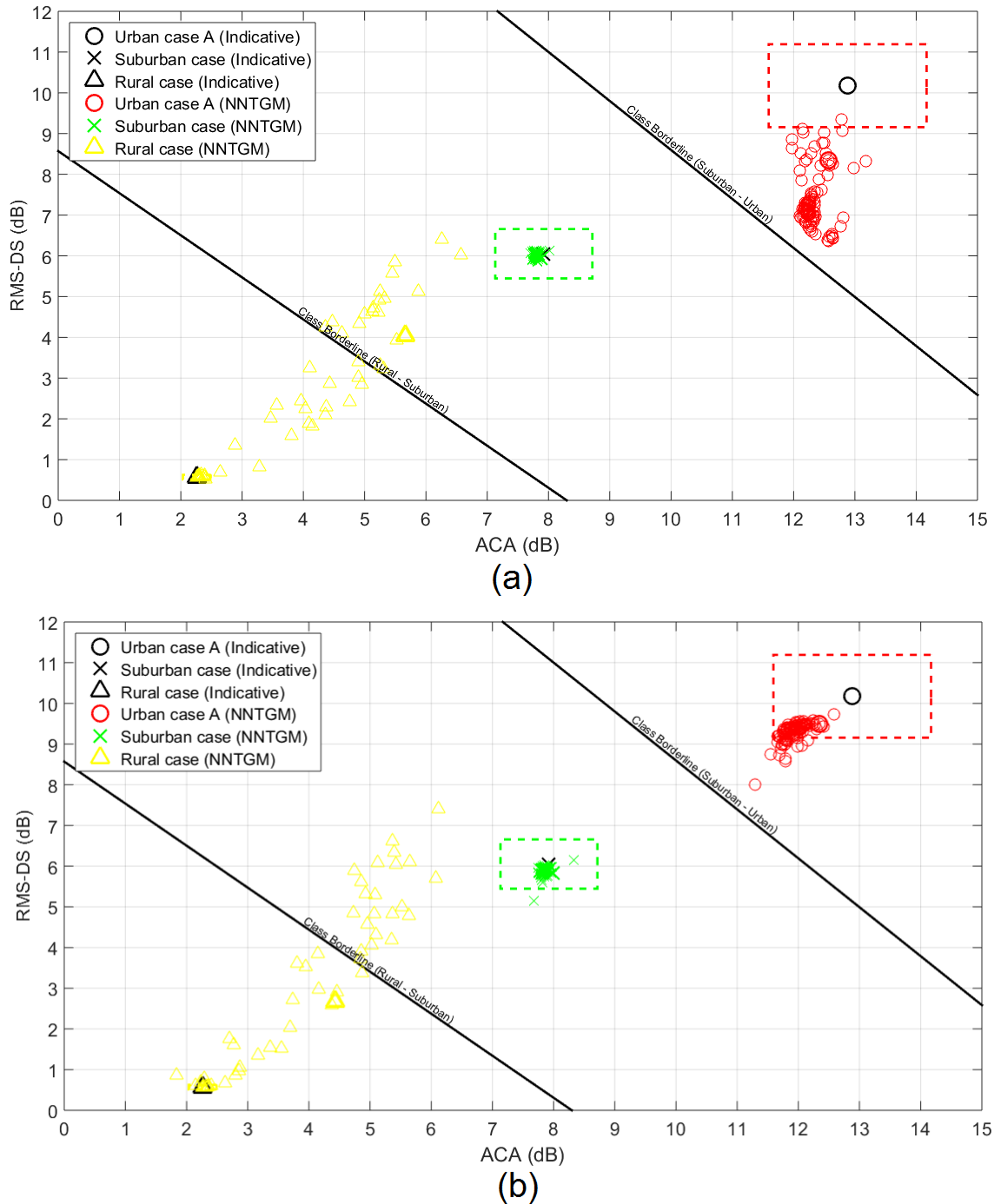


Fig. 6. OV LV BPL topology class map with NNTGM virtual topology footprints of the three indicative OV LV BPL topologies when the NNTGM default operation settings are applied and various lengths of the branch line segments are considered. (a) 4m. (b) 8m.

Table 5. GPIs of the NNTGM OV LV BPL topologies of the three OV LV BPL topology classes (NNTGM default operation settings are applied with various lengths of the branch line segments)

GPI	OV LV BPL topology class (Branch line segment length)					
	Rural case class		Suburban case class		Urban case A class	
	(4m)	(8m)	(4m)	(8m)	(4m)	(8m)
Inside the class (%)	80	78	100	100	100	100
Inside the box (%)	61	56	100	99	1	78

Number of Branch Line Segments of the NNTGM Default Operation Settings and NNTGM Virtual Topology Footprints

In Figure 7, the OV LV BPL topology class map and the NNTGM virtual topology footprints of the rural case, suburban case and urban case A are drawn when the NNTGM default operation settings are applied but the number of the branch line segments is equal to 2. With reference to Figure 7, the GPIs of this companion paper are applied to the NNTGM virtual topology footprints of the rural case, suburban case and urban case A and their values are reported in Table 6.

Comparing Figure 7 with Figures 6(a) and 6(b), it is obvious that the number increase of the branch line segments of the NNTGM default operation settings intensifies the NNTGM virtual topology footprint behavior that has been analyzed in the previous subsection where the length increase of the branch line segments has been studied. Indeed, the NNTGM virtual topology footprints of rural case and urban case A still spread away from the respective indicative OV LV BPL topologies demonstrating wide extents. GPIs of Table 6 indicate that the NNTGM virtual topology footprints of rural case and urban case A sparsely populate the respective OV LV BPL topology classes with “inside the class” GPIs that are equal to 93% and 29%, respectively, when the respective “inside the class” GPIs of Table 5 for the scenario of the length increase of the branch line segments were 78%-80% and 100%. But the real critical effect of the number increase of the branch line segments occurs when the “inside the box” GPIs of Table 6 are discussed. The vast majority of the NNTGM OV LV BPL topologies of the NNTGM virtual topology footprints of rural case and urban case A lie outside the ACA / RMS-DS boxes of $\pm 10\%$ of the respective indicative OV LV BPL topologies while the NNTGM virtual topology footprint of suburban case starts to go away from the ACA / RMS-DS boxes of $\pm 10\%$ of the indicative suburban case not being observed so far in the scenarios of the length increase of the branch line segments of Figures 6(a) and 6(b). In contrast with the impact of the distribution line parameters on NNTGM virtual topology footprints of Section 3.2, the extent of the NNTGM virtual topology footprints is significantly increased when higher numbers of branch line segments are assumed than the ones of OV LV BPL topologies with increased lengths of the branch line segments. In total, the impact of the changes of the lengths and of the number of branch line segments of the NNTGM default operation

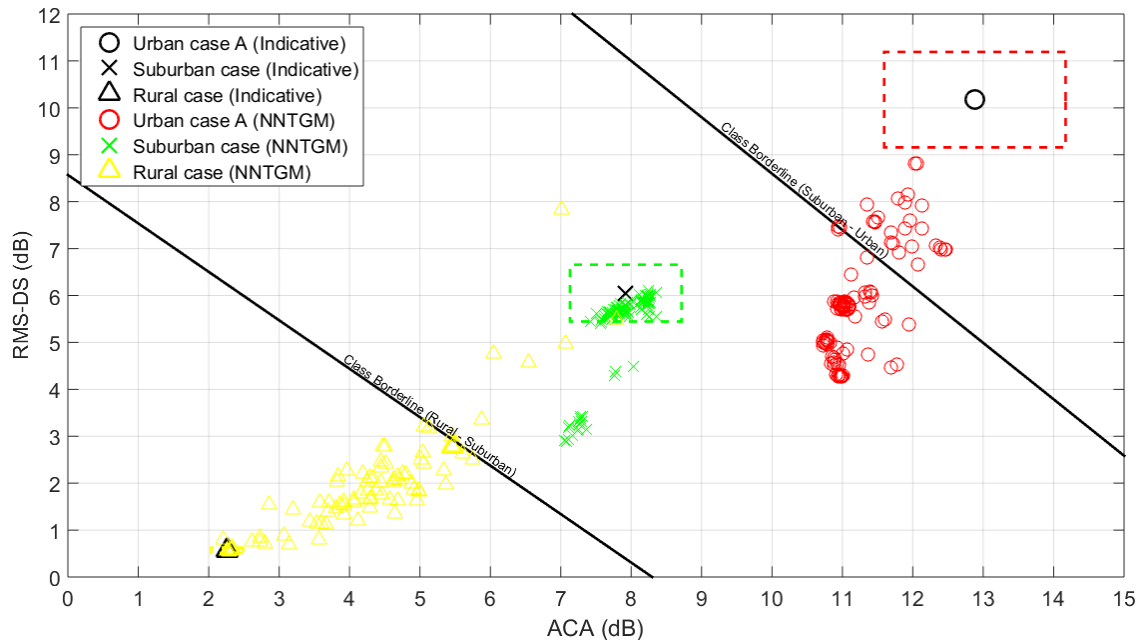


Fig. 7. OV LV BPL topology class map with NNTGM virtual topology footprints of the three indicative OV LV BPL topologies when the NNTGM default operation settings are applied and 2 branch line segments are considered.

Table 6. GPIs of the NNTGM OV LV BPL topologies of the three OV LV BPL topology classes (NNTGM default operation settings are applied when 2 branch line segments are assumed)

GPI	OV LV BPL topology class		
	Rural case class	Suburban case class	Urban case A class
Inside the class (%)	93	100	29
Inside the box (%)	23	79	0

settings on the NNTGM virtual topology footprints of the examined indicative OV LV BPL topologies present similarities concerning their position, their extent and the affected indicative OV LV BPL topologies but differences with the impact of the changes of the lengths and the number of distribution line segments of the NNTGM default operation settings. In accordance with GPIs, the most affected NNTGM virtual topology footprints from the branch line segment parameter changes of the NNTGM default operation settings are the ones of the urban case A and the rural case but also the NNTGM virtual topology footprint of the suburban case may be affected when the number of branch line segment gets increased.

In conclusion, from the perspective of generating virtual topologies for populating OV LV BPL topology classes, the previous findings concerning the impacts of distribution and branch line parameter changes of the NNTGM default operation settings on NNTGM virtual topology footprints may offer a plethora of populating scenarios. Depending on the distribution and branch line parameter of the NNTGM default operation settings, various shapes of NNTGM virtual topology footprints may be generated in terms of their position and extent with respect to their indicative OV LV BPL topologies. Therefore, OV LV BPL topology classes can be populated by NNTGM

virtual topologies of different characteristics that may be defined by the user taking into account his simulation scenario requirements.

Conclusions

In this companion paper, the numerical results for populating OV LV BPL topology classes by applying NNTGM are demonstrated and analyzed. In [1], the theory for populating OV LV BPL topology classes by applying NNTGM has been given. With reference to the class maps and the GPIs, the impact of the following NNTGM parameters on the NNTGM virtual topology footprints, whose significance has already been identified in [1], has been assessed, namely: (i) The inclusion or not of the examined indicative OV LV BPL topology in the TIM OV LV BPL topology database during the NNTGM operation; (ii) the length of the distribution / branch line segments; and (iii) the number of the distribution / branch line segments. First, as the inclusion of the examined indicative OV LV BPL topology in the TIM OV LV BPL topology database is concerned, NNTGM virtual topology footprints and GPIs of the indicative OV LV BPL topologies have shown that the TIM OV LV BPL topology database remains robust after the exclusion of the examined indicative OV LV BPL topology thus having small effect on the NNTGM class maps and footprints. Second, the length increases of the distribution and branch line segments of NNTGM default operation settings have complementary impacts on the NNTGM virtual topology footprints of the indicative OV LV BPL topologies. In fact, the length increase of the distribution line segments mainly moves and extends the NNTGM virtual topology footprints of the suburban case while the increase of the branch line segments mainly affects the position and extent of the NNTGM virtual topology footprints of the urban case A and the rural case. The aforementioned complementary behaviors offer an important tool for NNTGM in order to efficiently populate various OV LV BPL topology classes in various patterns. Third, the number increases of the distribution and branch line segments of NNTGM default operation settings present similar impacts on the NNTGM virtual topology footprints of the indicative OV LV BPL topologies of this pair of paper with the ones of the length increases of the distribution and branch line segments, respectively, but in a more drastic way with reference to GPIs of this paper. Concluding this pair of papers, NNTGM can generate theoretical channel attenuation behaviors given the topological characteristics of an indicative OV LV BPL topology, when appropriate NNTGM default operation settings are assumed, while the tuning of NNTGM operation settings may offer a plethora of populating scenarios for OV LV BPL topology classes that may be defined by the user taking into account his simulation scenario requirements.

CONFLICTS OF INTEREST

The author declares that there is no conflict of interests regarding the publication of this paper.

References

- [1] Lazaropoulos, A. (2024). Virtual Topologies for Populating Overhead Low-Voltage Broadband over Powerlines Topology Classes by Exploiting Neural Network Topology Generator Methodology (NNTGM) - Part 1: Theory. *Trends in Renewable Energy*, 10(3), 301-314. doi:<http://dx.doi.org/10.17737/tre.2024.10.3.00181>
- [2] Lazaropoulos, A. G. (2021). Information Technology, Artificial Intelligence and Machine Learning in Smart Grid – Performance Comparison between Topology Identification Methodology and Neural Network Identification Methodology for the Branch Number Approximation of Overhead Low-Voltage Broadband over Power Lines Network Topologies. *Trends in Renewable Energy*, 7, 87-113. doi:<http://dx.doi.org/10.17737/tre.2021.7.1.00133>
- [3] Lazaropoulos, A. G., & Leligou, H. C. (2023). Artificial Intelligence, Machine Learning and Neural Networks for Tomography in Smart Grid – Performance Comparison between Topology Identification Methodology and Neural Network Identification Methodology for the Distribution Line and Branch Line Length Approximation of Overhead Low-Voltage Broadband over Power Lines Network Topologies. *Trends in Renewable Energy*, 9(1), 34-77. doi:<http://dx.doi.org/10.17737/tre.2023.9.1.00149>
- [4] Lazaropoulos, A. G., & Leligou, H. C. (2024). Big Data and Neural Networks in Smart Grid - Part 1: The Impact of Piecewise Monotonic Data Approximation Methods on the Performance of Neural Network Identification Methodology for the Distribution Line and Branch Line Length Approximation of Overhead Low-Voltage Broadband over Powerlines Networks. *Trends in Renewable Energy*, 10, 30-66. doi:<https://doi.org/10.17737/tre.2024.10.1.00164>
- [5] Lazaropoulos, A. G., & Leligou, H. C. (2024). Big Data and Neural Networks in Smart Grid - Part 2: The Impact of Piecewise Monotonic Data Approximation Methods on the Performance of Neural Network Identification Methodology for the Distribution Line and Branch Line Length Approximation of Overhead Low-Voltage Broadband over Powerlines Networks. *Trends in Renewable Energy*, 10, 67-97. doi:<https://doi.org/10.17737/tre.2024.10.1.00165>
- [6] Patel, D. K., Phukan, H., Mansani, S., Singh, J., Sreejith, S., Goswami, A. K., & Patel, R. (2022). Smart Grid Communication and Information Technologies: A Review. In: Dash, R.N., Rathore, A.K., Khadkikar, V., Patel, R., Debnath, M. (eds) *Smart Technologies for Power and Green Energy. Lecture Notes in Networks and Systems, vol 443*. Springer, Singapore. doi:https://doi.org/10.1007/978-981-19-2764-5_5
- [7] Marcuzzi, F., & Tonello, A. M. (2023). Topology-based machine learning: Predicting power line communication quality in smart grids. *IEEE Access*, 11, 24851-24862. doi:<https://doi.org/10.1109/ACCESS.2023.3245361>
- [8] Ustun Ercan, S. (2024). Power line Communication: Revolutionizing data transfer over electrical distribution networks. *Engineering Science and Technology, an International Journal*, 52, 101680. doi:<https://doi.org/10.1016/j.jestch.2024.101680>
- [9] Lazaropoulos, A. G. (2012). Broadband Transmission and Statistical Performance Properties of Overhead High-Voltage Transmission Networks. *Journal of*

- Computer Networks and Communications*, 2012(1), 875632.
doi:<https://doi.org/10.1155/2012/875632>
- [10] Lazaropoulos, A. G. (2020). Business Analytics and IT in Smart Grid - Part 1: The Impact of Measurement Differences on the iSHM Class Map Footprints of Overhead Low-Voltage Broadband over Power Lines Topologies. *Trends in Renewable Energy*, 6(2), 156-186.
doi:<http://dx.doi.org/10.17737/tre.2020.6.2.00117>
- [11] Lazaropoulos, A. G. (2020). Statistical Channel Modeling of Overhead Low Voltage Broadband over Power Lines (OV LV BPL) Networks - Part 1: The Theory of Class Map Footprints of Real OV LV BPL Topologies, Branch Line Faults and Hook-Style Energy Thefts. *Trends in Renewable Energy*, 6(1), 61-87.
doi:<http://dx.doi.org/10.17737/tre.2020.6.1.00112>
- [12] Lazaropoulos, A. G. (2020). Business Analytics and IT in Smart Grid - Part 2: The Qualitative Mitigation Impact of Piecewise Monotonic Data Approximations on the iSHM Class Map Footprints of Overhead Low-Voltage Broadband over Power Lines Topologies Contaminated by Measurement Differences. *Trends in Renewable Energy*, 6(2), 187-213.
doi:<http://dx.doi.org/10.17737/tre.2020.6.2.00118>
- [13] Lazaropoulos, A. G. (2020). Business Analytics and IT in Smart Grid - Part 3: New Application Aspect and the Quantitative Mitigation Analysis of Piecewise Monotonic Data Approximations on the iSHM Class Map Footprints of Overhead Low-Voltage Broadband over Power Lines Topologies Contaminated by Measurement Differences. *Trends in Renewable Energy*, 6(2), 214-233.
doi:<http://dx.doi.org/10.17737/tre.2020.6.2.00119>
- [14] Lazaropoulos, A. (2020). Statistical Channel Modeling of Overhead Low Voltage Broadband over Power Lines (OV LV BPL) Networks - Part 2: The Numerical Results of Class Map Footprints of Real OV LV BPL Topologies, Branch Line Faults and Hook Style Energy Thefts. *Trends in Renewable Energy*, 6(1), 88-109.
doi:<http://dx.doi.org/10.17737/tre.2020.6.1.00113>
- [15] Lazaropoulos, A. G. (2013). Review and Progress towards the Capacity Boost of Overhead and Underground Medium-Voltage and Low-Voltage Broadband over Power Lines Networks: Cooperative Communications through Two- and Three-Hop Repeater Systems. *International Scholarly Research Notices*, 2013(1), 472190. doi:<https://doi.org/10.1155/2013/472190>
- [16] Lazaropoulos, A. G., & Cottis, P. G. (2009). Transmission characteristics of overhead medium voltage power line communication channels. *IEEE Transactions on Power Delivery*, 24(3), 1164-1173.
doi:<https://doi.org/10.1109/TPWRD.2008.2008467>
- [17] Lazaropoulos, A. G. (2012). Towards Modal Integration of Overhead and Underground Low-Voltage and Medium-Voltage Power Line Communication Channels in the Smart Grid Landscape: Model Expansion, Broadband Signal Transmission Characteristics, and Statistical Performance Metrics (Invited Paper). *International Scholarly Research Notices*, 2012(1), 121628.
doi:<https://doi.org/10.5402/2012/121628>
- [18] Meng, H., Chen, S., Guan, Y. L., Law, C. L., So, P. L., Gunawan, E., & Lie, T. T. (2004). Modeling of transfer characteristics for the broadband power line communication channel. *IEEE Transactions on Power delivery*, 19(3), 1057-1064. doi:<https://doi.org/10.1109/TPWRD.2004.824430>

- [19] Lazaropoulos, A. G., & Leligou, H. C. (2022). Fiber optics and broadband over power lines in smart grid: a communications system architecture for overhead high-voltage, medium-voltage and low-voltage power grids. *Progress in Electromagnetics Research B*, 95, 185-205.
doi:<http://dx.doi.org/10.2528/PIERB22062502>
- [20] Lazaropoulos, A. G., & Cottis, P. G. (2010). Capacity of overhead medium voltage power line communication channels. *IEEE Transactions on Power Delivery*, 25(2), 723-733. doi:<https://doi.org/10.1109/TPWRD.2009.2034907>
- [21] Lazaropoulos, A. G. (2016). New coupling schemes for distribution broadband over power lines (BPL) networks. *Progress in Electromagnetics Research B*, 71, 39-54. doi:<http://dx.doi.org/10.2528/PIERB16081503>
- [22] Amirshahi, P., & Kavehrad, M. (2006). High-frequency characteristics of overhead multiconductor power lines for broadband communications. *IEEE Journal on Selected Areas in Communications*, 24(7), 1292-1303.
doi:<https://doi.org/10.1109/JSAC.2006.874399>
- [23] Amirshahi-Shirazi, P. (2006). *Broadband access and home networking through powerline networks*. The Pennsylvania State University. Ph.D. dissertation.
- [24] Sartenaer, T. (2004). *Multiuser communications over frequency selective wired channels and applications to the powerline access network* (Ph.D. dissertation). Univ. Catholique Louvain, Louvain-la-Neuve, Belgium.
- [25] Sartenaer, T., & Delogne, P. (2006). Deterministic modeling of the (shielded) outdoor power line channel based on the multiconductor transmission line equations. *IEEE Journal on Selected areas in Communications*, 24(7), 1277-1291.
doi:<https://doi.org/10.1109/JSAC.2006.874423>
- [26] Sartenaer, T., & Delogne, P. (2001). Powerline cables modelling for broadband communications. In *Proceedings of the IEEE International Conference on Power Line Communications and Its Applications*, Malmö, Sweden, pp. 331-337.
- [27] Lazaropoulos, A. G., & Cottis, P. G. (2010). Broadband transmission via underground medium-voltage power lines-Part I: transmission characteristics. *IEEE Transactions on Power Delivery*, 25(4), 2414-2424.
doi:<https://doi.org/10.1109/TPWRD.2010.2048929>
- [28] Lazaropoulos, A. G., & Cottis, P. G. (2010). Broadband transmission via underground medium-voltage power lines-Part II: capacity. *IEEE Transactions on Power Delivery*, 25(4), 2425-2434.
doi:<https://doi.org/10.1109/TPWRD.2010.2052113>

Article copyright: © 2024 Athanasios G. Lazaropoulos. This is an open access article distributed under the terms of the [Creative Commons Attribution 4.0 International License](https://creativecommons.org/licenses/by/4.0/), which permits unrestricted use and distribution provided the original author and source are credited.





CALL FOR PAPERS

Trends in Renewable Energy

ISSN Print: 2376-2136 ISSN online: 2376-2144

<http://futureenergysp.com/index.php/tre/>

Trends in Renewable Energy (TRE) is an open accessed, peer-reviewed semi-annual journal publishing reviews and research papers in the field of renewable energy technology and science. The aim of this journal is to provide a communication platform that is run exclusively by scientists. This journal publishes original papers including but not limited to the following fields:

- ✧ Renewable energy technologies
- ✧ Catalysis for energy generation, Green chemistry, Green energy
- ✧ Bioenergy: Biofuel, Biomass, Biorefinery, Bioprocessing, Feedstock utilization, Biological waste treatment,
- ✧ Energy issues: Energy conservation, Energy delivery, Energy resources, Energy storage, Energy transformation, Smart Grid
- ✧ Environmental issues: Environmental impacts, Pollution
- ✧ Bioproducts
- ✧ Policy, etc.

We publish the following article types: peer-reviewed reviews, mini-reviews, technical notes, short-form research papers, and original research papers.

The article processing charge (APC), also known as a publication fee, is fully waived for the Trends in Renewable Energy.

Call for Editorial Board Members

We are seeking scholars active in a field of renewable energy interested in serving as volunteer Editorial Board Members.

Qualifications

Ph.D. degree in related areas, or Master's degree with a minimum of 5 years of experience. All members must have a strong record of publications or other proofs to show activities in the energy related field.

If you are interested in serving on the editorial board, please email CV to editor@futureenergysp.com.